Inversion of geothermal parameters using borehole and core data

Thesis · February 2008

Source: OAI

CITATIONS
4

READS
156

1 author:

Andreas Antonius Hartmann
Baker Hughes Incorporated
44 PUBLICATIONS **278** CITATIONS

SEE PROFILE

Inversion of geothermal parameters using borehole and core data

Von der Fakultät für Georessourcen und Materialtechnik
der Rheinisch-Westfälischen Technischen Hochschule Aachen

zur Erlangung des akademischen Grades eines

Doktors der Naturwissenschaften

genehmigte Dissertation

vorgelegt von

Diplom-Geophysiker Andreas Hartmann

aus Sassenberg

Berichter: Univ.-Prof. Dr. rer. nat. Christoph Clauser
Dr. Francis Lucazeau

Tag der mündlichen Prüfung: 18. Februar 2008

Diese Dissertation ist auf den Internetseiten der Hochschulbibliothek online verfügbar

Für meine Familie

Franziskas „Promotion“

Contents

Chapter 1

Introduction

Possibly the oldest temperature measurement in a borehole was performed in Rüdersdorf, Germany, in 1831 [*Magnus*, 1831]. Heinrich Gustav Magnus developed a mercury maximum thermometer ("geothermometer") to perform such measurements. This long standing interest in the temperature of the subsurface stems from the fact that temperature is an important constraint for possible geodynamic processes acting at depth (see for example figure 1.1, after *Chapman and Furlong* [1992]). To constrain subsurface temperatures, considerable effort has been put into determining undisturbed, representative heat flux density values and mapping of heat flux density in different tectonic settings. These efforts of the geothermal community have led to the setup of a database of heat flux density values by the International Heat Flow Commission (IHFC) of the International Association of Seismology and Physics of the Earth's Interior (IASPEI).

The ongoing interest in the temperature distribution of the crust and mantle is demonstrated by current work that uses novel ways of determining regional and global heat flux density distributions. For instance, heat flux density might be derived from Curie point depths obtained from aeromagnetic and satellite data [*Aydin et al.*, 2005; *Fox Maule et al.*, 2005] as well as from seismic tomography studies [*Shapiro and Ritzwoller*, 2004].

Parallel to the application of novel methods to determine heat flux density distributions, borehole temperature data have seen new applications in fields other than heat flux density determination. At the very beginning of heat flow studies it was noted that temperature in the subsurface can be modified by transient changes of the surface temperature and by advection of heat due to groundwater flow [e.g. *Lane*, 1923; *Hotchkiss and Ingersoll*, 1934]. Because classical studies assume a steady-state, conduction dominated thermal regime, it was attempted either to correct these data or to avoid "disturbed" temperature data altogether. Later, methods were developed for deriving meaningful results from these "disturbing" thermal signatures observed in the data. Temperature data is valuable for the study of hydrogeological regimes, in particular for quantifying groundwater flow rates. This was first studied by *Stallmann* [1963] and *Bredehoeft and Papadopulos* [1965]. They describe the effect of vertical groundwater flow on temperature profiles. Using similar methods, patterns of recharge and discharge can be identified on the regional basin scale [e.g. *van der Kamp and Bachu*, 1989; *Clauser and Villinger*, 1990; *Clauser et al.*, 2002]. On the borehole scale, small rates of fluid flowing into or out of the borehole can be detected by disturbances of the conductive temperature profile [e.g. *Ziagos and Blackwell*, 1981].

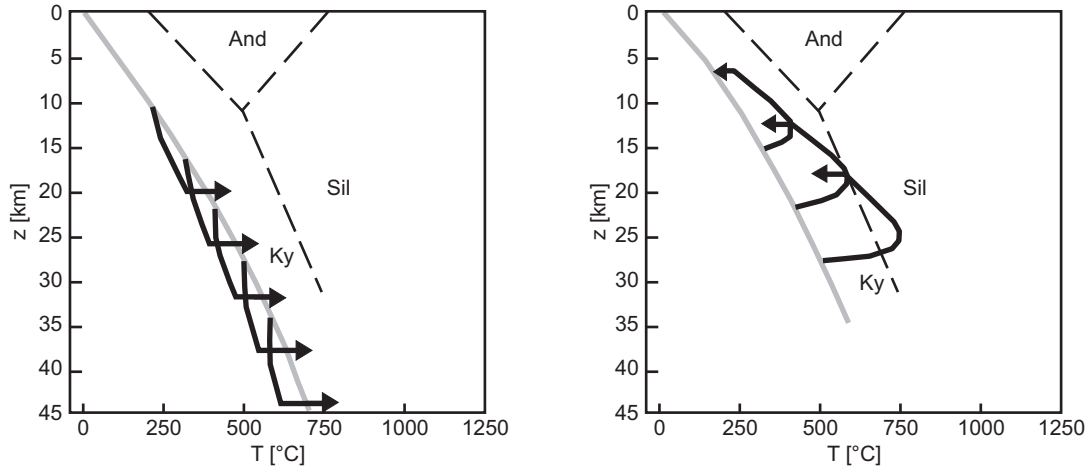

Figure 1.1: Example of geotherms and pressure-temperature (PT) paths for a subsidence of 10 km by sedimentation (*left*) and underplating, followed by 10 km of erosion (*right*) (after *Chapman and Furlong* [1992]). Grey lines depict the steady-state geotherms, dashed lines show stability windows for minerals Andesite (And), Sillimanite (Sil), and Kyanite (Ky), that serve to classify metamorphic rocks [*Winkler*, 1979]. Depending on the geological process, rocks follow different PT-paths (bold black lines) that leave different genetic imprints on the rocks.

Temperature data have also seen some use in geologic interpretation of wireline data, because the temperature gradient is sensitive to lithological changes and can be used for stratigraphic correlation similar to the γ-ray log [*Reiter et al.*, 1980; *Beck*, 1976].

Sometimes, the signatures caused by transient temperature variations may be as large as those caused by heat advection or lithological changes. In particular, changes in ground surface temperature (GST) may cause a curvature in the temperature log similar to that due to vertical discharge or recharge. In such a case, a joint analysis of both effects is obviously necessary. This type of analysis is usually based on strongly simplified models of the subsurface, for instance a homogeneous half-space [*Taniguchi et al.*, 1999]. However, another possible source of similar curvature is sedimentary compaction and the corresponding change in physical properties (see section 2.4.3). A similar ambiguity may result from groundwater flow in thin, inclined aquifers [*Vasseur et al.*, 1993; *Zschocke et al.*, 2005]. This modifies the vertical heat flux density as heat is advected horizontally into or out of a given control volume. However, the corresponding offset in the vertical profile of heat flux density is again non-unique, as it could be produced as well by an unnoticed change in thermal conductivity.

The quoted studies are just a few of many applications where temperature data contribute to other disciplines. They all have in common that they require good control of thermal properties to define the background steady-state conductive regime. A continuous profile would be ideal in this respect. Continuous coring of a borehole is usually out of the question, therefore thermophysical properties need to be determined from wireline logs. In today's hydrocarbon formation evaluation, it is standard practise to determine physical properties from wireline data. This technique started with empirical relations to compute porosity from sonic or electrical logs, assuming

simple binary mixtures of rock matrix and pore space, [e.g. *Wyllie et al.*, 1956; *Archie*, 1942]. Later, more complicated models were used to identify the volumetric composition of the rock such as the M-N crossplot or the MID crossplot [*Burke et al.*, 1969; *Clavier and Rust*, 1976].

Today, methods to determine lithology may be divided into two categories:

- Early deterministic methods have evolved to a point where a general model of the mineral and fluid composition of the host rock yields a theoretical log response that is compared to the borehole logs. The optimum rock model is found using least-squares minimisation [e.g. *Doveton and Cable*, 1979].

- A different approach is taken in statistical models. Here, a set of log responses is defined for a given rock type in a training session with known rock types. During the analysis phase, this characterisation is transferred to the entire logged interval. Rock types are assigned based on "proximity" of their log responses to those of the training set. The proximity needs to be computed. This can be done, for instance, using discriminant analysis [*Serra*, 1984; *Bartetzko et al.*, 2001, 2002] or neural networks [*Benaouda et al.*, 1999; *Bhatt and Helle*, 2002].

These methods were designed mainly to derive information important for hydrocarbon exploration but were also applied to the problem of determining thermal conductivity. However, temperature as the measurement most sensitive to thermal conductivity variations has not been included in these algorithms. This is because wireline logs, as a rule, can be assumed to probe the local rock volume around the tool. Temperature models, in contrast, involve solving a differential equation for the full depth range including non-local parameters such as heat flux density, variations of ground surface temperature (GST), or recharge and discharge rates. These cannot be handled by existing inversion methods for wireline logs.

In this work this gap is bridged by developing an inverse scheme for borehole data that includes temperature data in the petrophysical inversion. The approach corresponds to the deterministic one where the volumetric composition of the rock is linked to the log response via physical relationships. In the case of temperature, this implies solving the one-dimensional heat diffusion equation. The intricate nature of this problem, compared to the inversion of conventional logs, requires advanced methods. This leads to using a Bayesian-type inversion with prior information and applying automatic differentiation to generate the Jacobian matrices of arbitrary complicated models. Since the algorithm is implemented in this flexible way it can also be used for other petrophysical applications.

This thesis is divided into two parts. In the first part (chapters 2 and 3) inversion of temperature data and inversion of rock properties from logging data are studied independently of each other, using existing methods. In the second part (chapter 4) these analyses are combined in a new algorithm for the joint inversion of temperature and other logging data.

Although the algorithm could be extended to handle advective problems as well, I will restrict myself to the treatment of purely conductive problems. The main focus of chapter 2 is therefore the problem of transient heat diffusion with regard to incomplete information on thermal properties as well as data noise and insufficient depth range of the data. The sensitivity of the result

on thermal properties is computed. In general, it is concluded that the diffusive part cannot be ignored, although resolving the past changes in GST might be sometimes problematic.

The correlation between thermal conductivity and other physical rock properties is discussed in chapter 3 using laboratory and logging data. Here, I review the relationships between thermal and other properties and present some empirical correlations. Also, a review of several mixing laws is provided. This helps deciding which relationship is the most appropriate for the inversion of logging data.

Chapter 4 introduces the new algorithm developed for the inversion of logging data. It starts by presenting the forward models used to compute log responses from the rock model. The inverse algorithm is then discussed in detail, in particular with respect to methods for efficiently computing the Jacobian matrix. This is followed by tests against existing algorithms, where specific functionality is verified. The chapter concludes with some applications of the algorithm to the geothermal and petrophysical inverse problem.

At the time of writing of this thesis, part of the work reported here has been published:

Chapter 2: Hartmann, A., and V. Rath, Uncertainties and shortcomings of ground surface temperature histories derived from inversion of temperature logs, *Journal of Geophysics and Engineering*, *2*, 299–311, 2005.

Chapter 3: Hartmann, A., V. Rath, and C. Clauser, Thermal conductivity from core and well log data, *International Journal of Rock Mechanics & Mining Sciences*, *42*, 1042–1055, 2005.

Chapter 2

Reconstruction of paleotemperatures at the earth's surface

Borehole temperatures record past changes in ground surface temperature (GST) as the transient temperature signal diffuses into the subsurface. In numerous studies, temperature data have been used to reconstruct time series of ground surface temperature. The value of such reconstructions as a proxy for the paleoclimate, however, is still subject of research and discussion [e.g. *Mann and Schmidt*, 2003]. It has been shown [e.g. *González-Rouco et al.*, 2003; *Signorelli and Kohl*, 2004] that surface air temperature (SAT) and soil temperature correlate well on long timescales. Reconstructions can be carried out on various timescales from a few hundred years to 100 000 years. Combined with proxy climate data, millennial scale reconstructions serve as a means to investigate natural and anthropogenic climate change. In contrast, long-term reconstructions study the temperatures of the last ice age and its transition to our current climate.

The problem is usually assumed to be purely conductive and one-dimensional. Inversion results will be in error if these assumptions are inadequate. Previous studies have already analysed various effects that can possibly influence the transient signal. For instance, the error introduced by the common assumption of one-dimensionality has been treated by *Shen et al.* [1995] and *Kohl* [1999]. Advection of heat by groundwater flow can modify the signal considerably [*Clauser and Villinger*, 1990; *Clauser et al.*, 1997; *Kohl*, 1998; *Taniguchi et al.*, 1999; *Reiter*, 2005]. The following analysis will show that even with all simplifying assumptions fulfilled, artefacts may be produced by the inversion of temperature data. Although a particular algorithm is used in this study, the results will apply, by and large, to other programs as well.

2.1 Theory

The algorithms commonly used for GST history inversion assume a one-dimensional, purely conductive subsurface whose physical properties are known. The medium may be either homogeneous [e.g. *Mareschal and Beltrami*, 1992; *Beltrami and Mareschal*, 1995] or layered [*Shen and Beck*, 1991, 1992]. Both approaches can be applied to single temperature logs or to ensembles of logs in order to improve the signal to noise ratio [*Beltrami and Mareschal*, 1995;

Clauser and Mareschal, 1995]. A comparison of different codes [*Beck et al.*, 1992] showed that all perform equally well for similar model assumptions.

In the model considered here [*Mareschal and Beltrami*, 1992; *Beltrami and Mareschal*, 1995; *Clauser and Mareschal*, 1995], the subsurface is assumed to be homogeneous. The steady-state temperature profile is defined by the heat flux density at the surface q_0, the pre-observational mean ground surface temperature T_0, thermal conductivity λ, and heat production rate A of the subsurface. Together with an additional transient term $T_t(z,t)$ the temperature at time t and depth z is given by [*Carslaw and Jaeger*, 1959; *Mareschal and Beltrami*, 1992]:

$$T(z,t) = T_0 + \frac{q_0 z}{\lambda} - \frac{A z^2}{2\lambda} + T_t(z,t). \tag{2.1}$$

In the particular case that the GST history can be parametrised by a series of temperature steps T_j^G at times t_j before present ($t = 0$), the transient term becomes

$$T_t(z) = \sum_{j=1}^{N} T_j^G \left(\operatorname{erfc}\left(\frac{z}{2\sqrt{\kappa t_j}} \right) - \operatorname{erfc}\left(\frac{z}{2\sqrt{\kappa t_{j-1}}} \right) \right). \tag{2.2}$$

If thermal conductivity, diffusivity, and heat production rate are known, the remaining unknowns are T_0, q_0, and T_j^G. If temperatures are recorded at depths z_i ($i = 1, ..., M$), equation 2.1 yields a set of M linear equations which can be solved for the $N + 2$ unknown variables. The solution needs to be regularised because the problem is ill-posed. The singular value decomposition [*Lanczos*, 1961] is used for this purpose: It solves the linear problem and at the same time seeks a solution that minimises the norm of the model. Implications of this procedure will be discussed in more detail in section 2.3.

This code[1] was employed in various case studies for the reconstruction of past climates [e.g. *Beltrami et al.*, 1997; *Beltrami and Bourlon*, 2004; *Clauser and Mareschal*, 1995; *Clauser et al.*, 1997; *Jones et al.*, 1999]. It was also used in conjunction with other proxy data to improve the temporal resolution of the GST history [*Beltrami et al.*, 1995; *Beltrami and Taylor*, 1995] as well as the study of coupling between GST and SAT [*Signorelli and Kohl*, 2004; *Nitoiu and Beltrami*, 2005].

2.2 Paleoclimatic influence on subsurface temperatures

The magnitude as well as time and depth scales of GST changes are shown in figure 2.1. A temperature history of the past million years based on proxy data [*Haenel et al.*, 1988, table 10.9] is used to demonstrate the effect of this transient signal on the subsurface temperatures. The curve was derived for Switzerland [*Rellstab*, 1981] but its main features are considered characteristic for the Central European climate of the last 1 million years. The proxy curve is subdivided into three parts and for each part the transient perturbation is calculated using equation 2.1. The

[1] A MATLAB™ version of the program including a GUI for the optimal choice of the regularisation parameter by means of the L-curve method can be downloaded from:
`http://www.geophysik.rwth-aachen.de/Downloads/software.html`

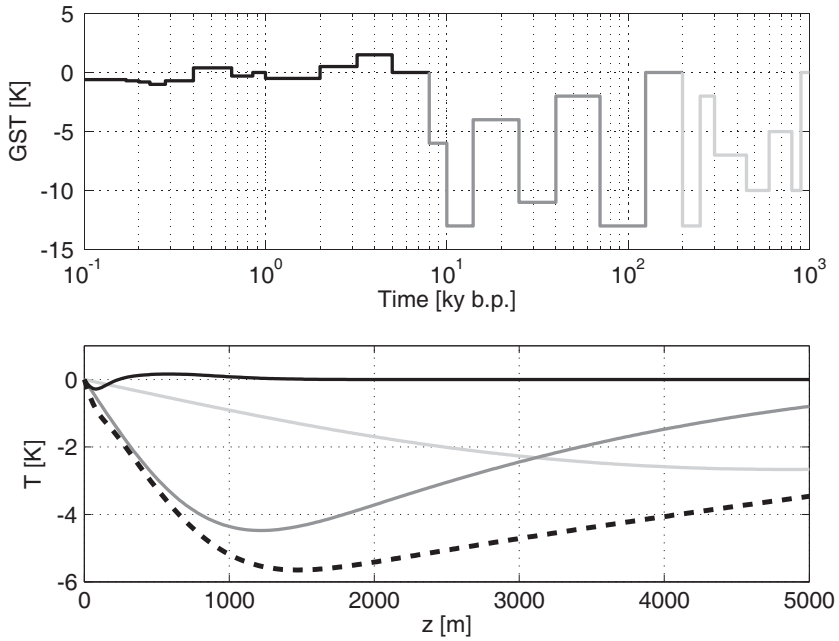

Figure 2.1: Time and depth scales of GST changes and corresponding changes in today's subsurface temperature. *Top:* Idealised GST history [*Haenel et al.*, 1988, table 10.9]. Different line styles correspond to different periods. *Bottom:* Temperature anomalies ΔT in the subsurface computed from the time series. Line styles correspond to the periods of the upper panel. The dashed line represents the sum of the individual anomalies.

steady-state temperature T_0 is assumed to be 0 °C for all computations. The transient signals for each of the periods are shown in figure 2.1 (bottom panel, solid lines). The total transient signal (bottom panel, dashed line) is the sum of these three contributions.

For this particular GST history, variations occurring on the order of 10^6 years will result in a virtually straight temperature anomaly with a slope of about -1 K km^{-1} unless the temperature log runs down to a depth of at least 4000 m. The magnitude of the slope might change for a different GST history. However, it is clear that this part of the transient signal cannot be resolved by an inversion of temperatures logged in boreholes, particularly not in the presence of noise. Thus, GST fluctuations from 100 000 years to 1000 000 years before present will usually modify only the pre-observational mean temperature. The glacial temperature minimum and the post-glacial temperature increase (100 000 years to 10 000 years b. p.) cause the most prominent disturbance. The temperature deviation reaches its maximum amplitude at depths of about 1500 m but still amounts to 1.5 K at 4000 m depth. Because most of the available temperature data world-wide are derived from shallower boreholes, a large portion of this signal is frequently not recorded. The signal due to temperature variations during the Holocene can be traced down to a maximum depth of 1000 m. Although there are many temperature logs in this depth range, most GST reconstructions have been attempted using substantially shallower data.

From this discussion the question arises whether reliable reconstructions of past temperatures

are possible when only part of the transient signal is contained in the data. This issue will be addressed in section 2.4. Sensitivity of the results with respect to the thermal properties of the subsurface will also be tested. However, before these effects can be analysed, the ill-posed character of the inverse problem and the regularisation procedure need to be discussed (section 2.3). Both problems are related, because similar to noisy data, data from shallow boreholes will render the inverse problem ill-posed.

2.3 Optimum choice of regularisation parameter

For the ill-posed inverse problem some sort of regularisation is needed to obtain a stable solution. In the singular value decomposition, two methods can be used [*Menke*, 1989]: (1) Either only the p largest singular values are used in the inversion, or (2) a damping parameter ϵ is added to the singular values λ_i such that

$$\frac{1}{\lambda_i^*} = \frac{\lambda_i}{\epsilon^2 + \lambda_i^2}. \tag{2.3}$$

Either way, stability is gained at the cost of losing model resolution. Both methods require a choice of a regularisation parameter, i.e. the number of singular values discarded, or the magnitude of the damping parameter ϵ. A regularisation of this type tends to minimise the norm of the model. This is equivalent to minimising the objective function $\phi(m)$ given by [*Aster et al.*, 2004; *Farquharson and Oldenburg*, 2004]:

$$\phi(\mathbf{m}) = ||\mathbf{G}(\mathbf{m}) - \mathbf{d}|| + \epsilon^2 ||\mathbf{m}||. \tag{2.4}$$

Here, the first term represents the L_2-norm of the data misfit, with $\mathbf{G}(\mathbf{m})$ and $\mathbf{d}$ being the forward model and the data, respectively. The second term represents the L_2-norm of the model $\mathbf{m}$. In terms of paleoclimate inversion, minimising the model norm may change the amplitude of paleoclimatic disturbances. However, too small an ϵ will lead to an oscillating solution for the GST. Thus it is important to choose a proper value for the damping parameter, preferably based on some objective criterion.

One way to gain insight into this problem is the L-curve [*Hansen*, 1998; *Farquharson and Oldenburg*, 2004], so called for its shape. To create this curve, the inversion is repeated for a range of regularisation parameters ϵ and the data misfit norm is plotted versus the model norm (figure 2.2). A large value of ϵ causes a strongly dampened model and poor data fit. Thus, the model norm will be small but the data misfit norm will be large. In contrast, a small ϵ will result in a good data fit but strongly oscillating GST history, i.e. a large model norm and a small data misfit norm. These two cases characterise the asymptotic behaviour of the L-curve. The point of maximum curvature of this curve defines a compromise between the two extremes. This is considered as the optimal value for the regularisation parameter [*Hansen*, 1998].

The inverse problem is studied with the help of the L-curve criterion. A synthetic temperature log is created using the set of parameters given in table 2.1. The transient temperature anomaly given in figure 2.1 is added to the steady-state solution and random, normally distributed noise is added. The noise amplitudes σ for the test data sets are 0.01, 0.2, 0.4, and 0.6 K.

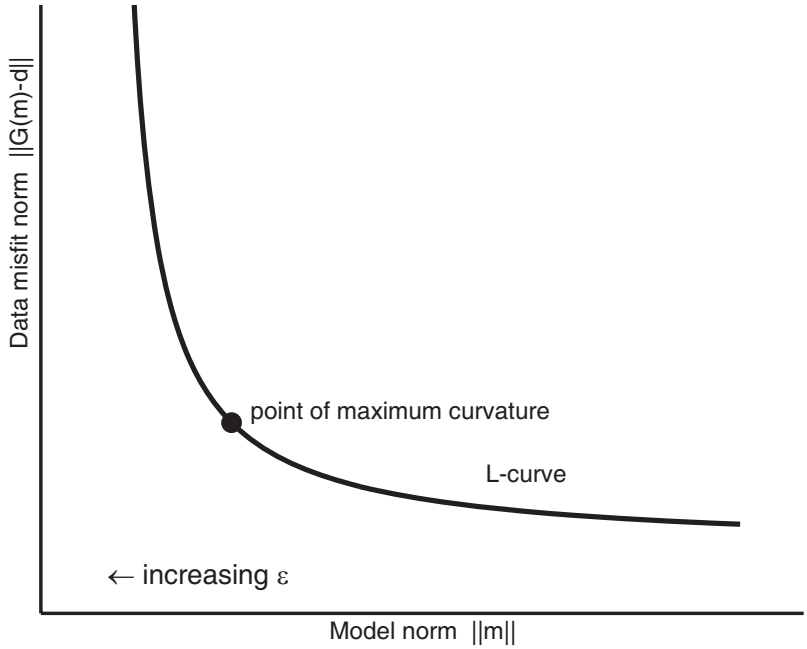

Figure 2.2: Principle of the L-curve. With increasing ϵ the model norm decreases and the data misfit norm increases. The optimum value for ϵ can be found at the maximum curvature point of the curve.

Table 2.1: Thermal properties, boundary conditions, and inversion parameters that are used throughout the text to compute and invert synthetic temperature logs.

Thermal conductivity λ	2.5	W (m K)$^{-1}$
Volumetric heat capacity (ρc)	$2.30 \cdot 10^{6}$	J m^{-3} K^{-1}
Thermal diffusivity κ	$1.09 \cdot 10^{-6}$	m^{2} s^{-1}
Heat production rate A	$1.00 \cdot 10^{-6}$	W m^{-3}
Steady-state surface temperature T_0	10	°C
Steady-state surface heat flux density q_0	0.06	W m^{-2}
Sampling rate of the temperature log	1	m
Total depth of the temperature log	5000	m
Number of time steps for the inversion	20	
Start time of inversion	1000	kyr b.p.
End time of inversion	0.1	kyr b.p.

Figure 2.3 shows the variation of the L-curve and the optimum ϵ as a function of the noise level. It appears that only for the smallest noise level the L-curve assumes a shape with a well defined maximum curvature point. At all noise levels, the L-curve displays an asymptotic region where any change in ϵ results in large changes in the model norm but does not change the data misfit at all. This means that a value of ϵ less than the value found in the maximum curvature

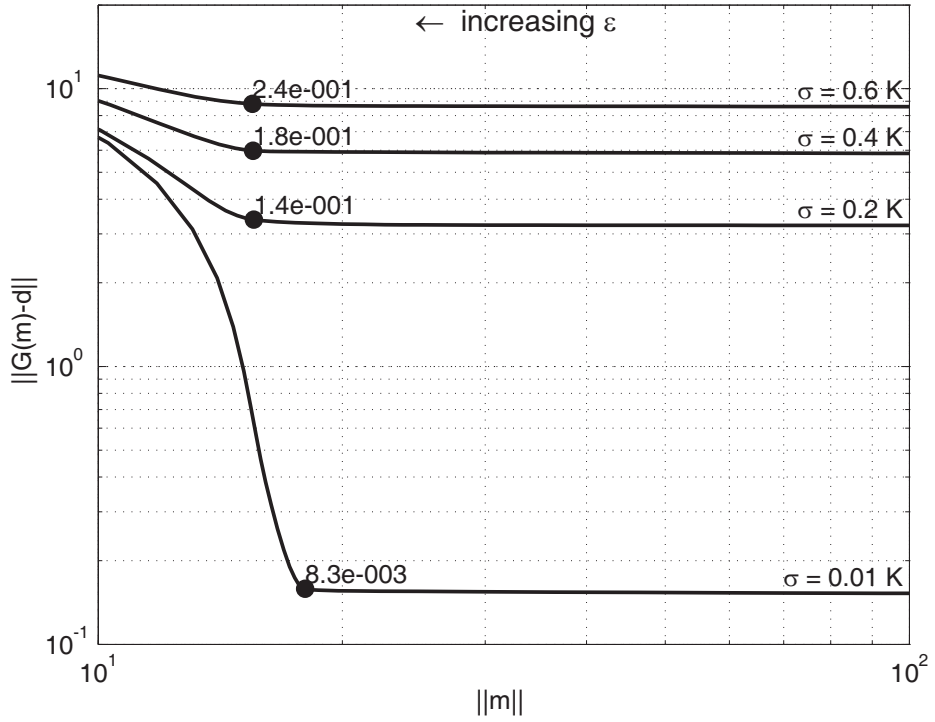

Figure 2.3: L-Curves for different noise levels. A synthetic temperature log is inverted several times with increasing ϵ. The resulting data misfit norm $||\mathbf{G}(\mathbf{m}) - \mathbf{d}||$ is plotted against the model norm $||\mathbf{m}||$ for different levels σ of noise. The circles indicate the points of maximum curvature with the corresponding values of ϵ.

point is not justified by the data. It is noteworthy that the values of the model norm of the optimum models do not vary much with the noise level. This indicates that the inverted model is robust against noise for this configuration. This point is illustrated by comparing the inverted GST histories for optimum values of ϵ (figure 2.4). The major feature of the GST histories is the temperature rise at the end of the last ice age. It is preserved in all of the results in comparable magnitude. In contrast, smaller temperature variations during the Holocene period are only resolved at the smallest noise level. Thus, the L-curve allows to decide whether a specific feature in the paleoclimatic record can be resolved by the data.

Finally, figure 2.5 shows a comparison of inversion results for a given noise level of $\sigma = 0.2$ K and a range of ϵ-values. The best value would be about 0.14, yielding a rather smooth model. Being possibly aware of a paleoclimatic proxy curve similar to the ones shown in the figure one might be tempted to choose a smaller value seemingly fitting better the temperature variations in the model during the Holocene. However, figure 2.3 demonstrates that the data fit does not improve for all ϵ-values smaller than 0.14. This suggests that the small amplitude variations on top of the temperature increase at the end of the ice age are merely numerical artefacts.

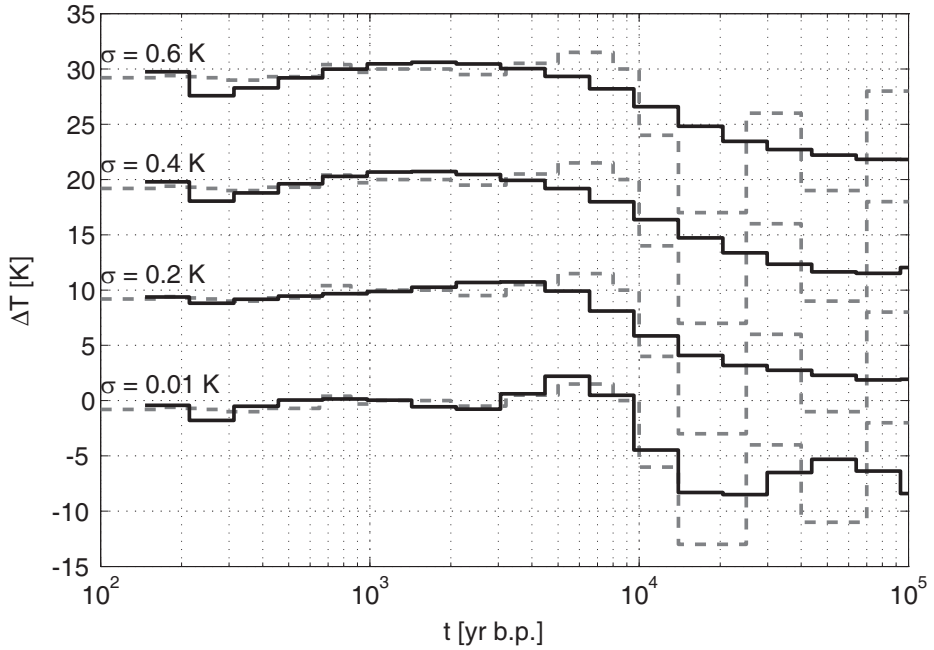

Figure 2.4: Inverted GST-history $\Delta T(t)$ for different noise levels σ and optimum values of ϵ from figure 2.3. The curves are offset from each other by 10 °C for better visibility. The dashed grey line shows the idealised GST history according to *Haenel et al.* [1988].

2.4 Sensitivity analysis

Results obtained from the inversion of temperature data are always subject to various sources of error. The effect of random noise can be assessed by computing the appropriate posterior covariance matrix. Systematic errors, for instance from biased estimates of subsurface properties, cannot be assessed in this way because the inversion procedure assumes the model to be exact. One way to quantify these errors is to vary systematically the relevant model parameter and to compare the results against the expected one. This will be the subject of the next sections. Several potential sources of errors will be considered: a) Length of the temperature log; b) Assumed thermal properties of the homogeneous subsurface; c) The effect of a heterogeneous subsurface. The discussion will be aided by the results of the previous section because the introduction of errors often results in an apparent decrease of the signal-to-noise ratio. This may be an effect of the inadequate model. Nevertheless, it is necessary to modify the regularisation in order to obtain a stable solution.

2.4.1 Length of the temperature log

In view of the limited depths of available boreholes it is important to know how much of the full depth range of the transient signature is required for a valid reconstruction of the GST history. To analyse this problem, a synthetic temperature log with a simplified GST history of the last

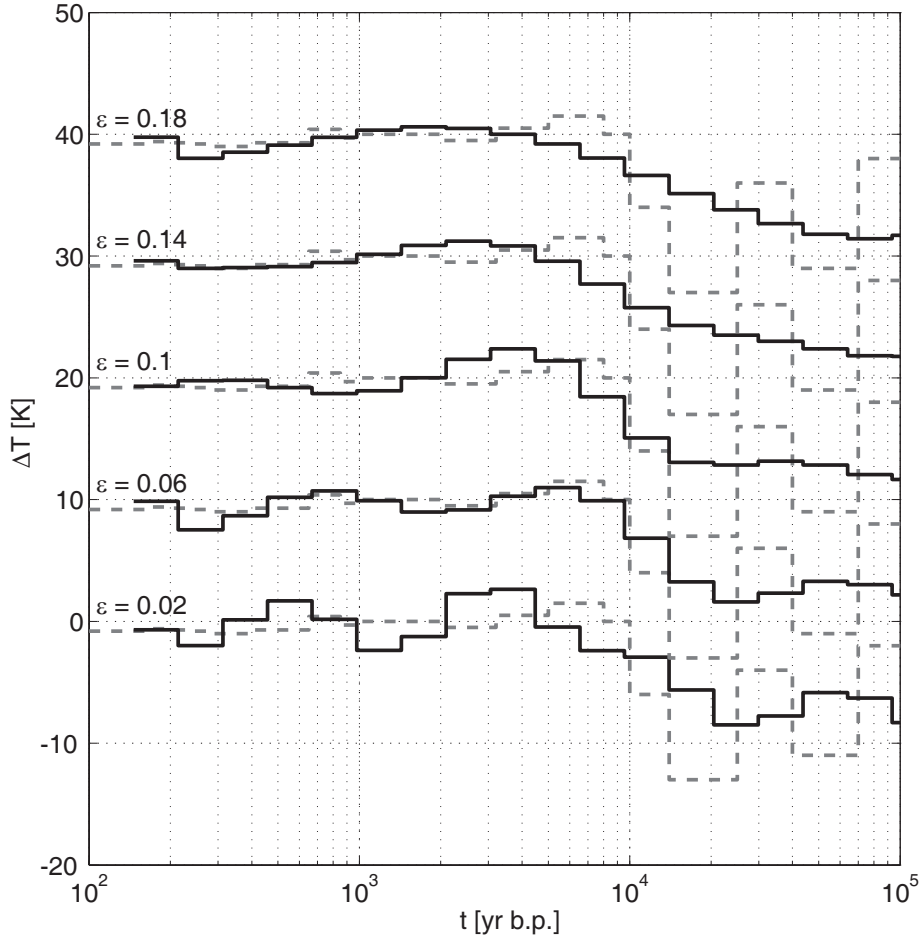

Figure 2.5: GST-histories $\Delta T(t)$ for a fixed noise level $\sigma = 0.2$ K and different values of the damping parameter ϵ. The optimum choice of ϵ according to the L-curve criterion is 0.14. The dashed grey line shows the idealised GST history according to *Haenel et al.* [1988].

1 million years was computed. The parameters for the synthetic temperature log are identical to those used in the L-curve studies (table 2.1). The GST history that produces the transient temperature signal (grey line, figure 2.6) does not represent an actual paleoclimatic curve but rather an idealised history with correct order of magnitude for amplitude and timing of the events.

For the inversion, the originally 3000 m deep log was truncated at depths of 2000 m and 1500 m. The inversion of these logs yielded a first set of results. Then, normally distributed noise with a standard deviation $\sigma = 0.3$ K was added to the data and the inversion was repeated. For the inversion of the noise-free and noisy logs, a constant damping parameter of $\epsilon = 0.1$ and $\epsilon = 0.2$ was used, respectively.

The resulting GST histories for the different inversion runs are displayed in figure 2.6. For both the noisy and the noise-free data, a log depth of 3000 m seems to be sufficient to recover fully the amplitude of the last glacial stage. A decrease of the maximum log depth also reduces the

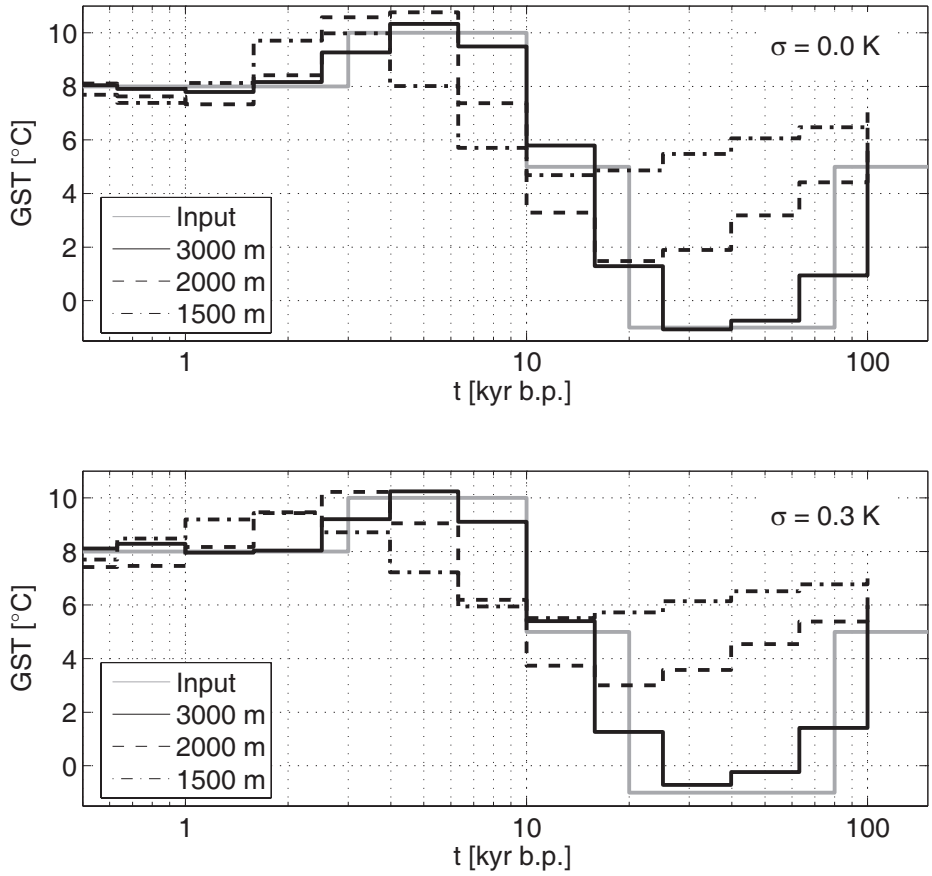

Figure 2.6: Truncation of logs results in different GST reconstructions. The black solid lines represent the GST history that was used to drive the forward model. The other lines show reconstructions for different depths of the logs. The temperature of the last glacial minimum is only resolved for the 3000 m log. Note that events in the Holocene are shifted with respect to input GST history. *Top:* Noise-free data. *Bottom:* $\sigma = 0.3$ K.

amplitude of the glacial cooling. Further, the times of the minimum and maximum temperatures of the GST reconstruction are shifted to earlier times. The effect is more pronounced for the noisy data. But even for noise-free data any reconstruction of the last ice age GST based on logs shallower than 2000 m seems to be inadequate.

A similar procedure of log-truncation can be used to estimate the necessary depth of temperature logs for millennial-scale GST inversions. This is important as today the temperatures of the last millennium are usually inferred from proxy reconstructions. Competing models correspond to different climate variability for the last millennium. Currently, the validity of these reconstructions is a subject of an ongoing debate in the scientific community. The geothermal method can provide valuable insight into this problem as it is the only one based directly on paleotemperature. All the more it is important to analyse the amount of information about past temperatures which can be extracted from the data.

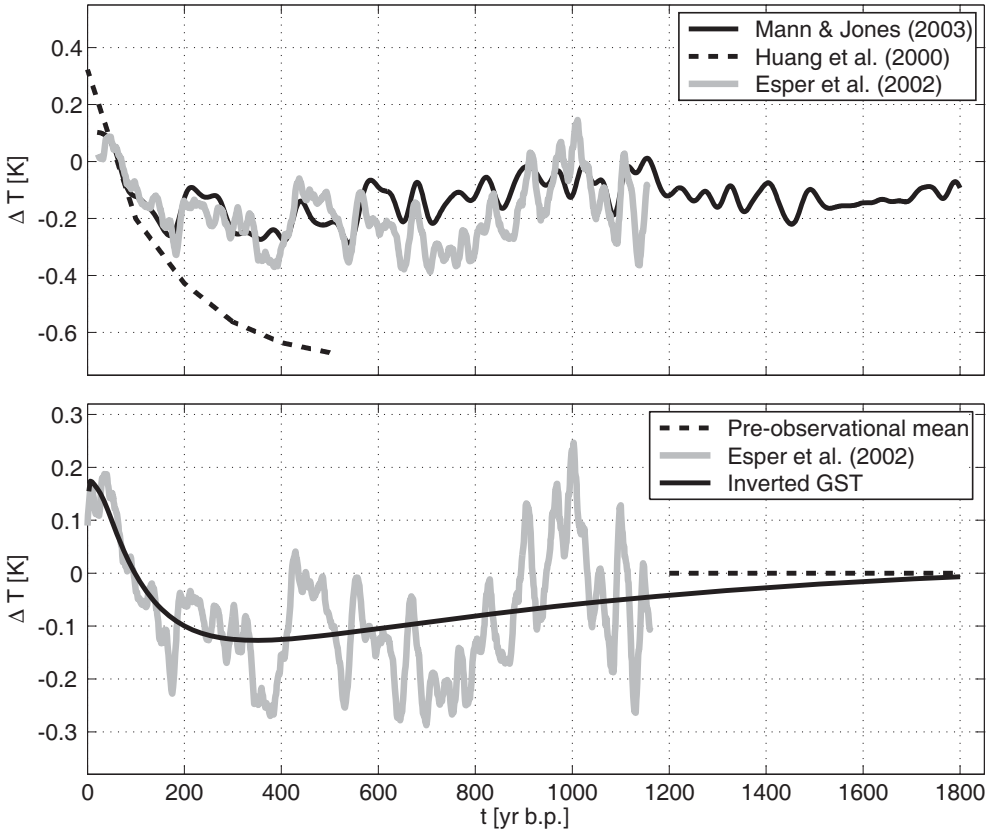

Figure 2.7: *Top:* Two reconstructions of the northern hemisphere annual mean surface air temperatures during the last two millennia [*Mann and Jones*, 2003; *Esper et al.*, 2002] compared to a northern hemisphere GST history for the last 500 years [*Huang et al.*, 2000]. *Bottom:* Inversion results for a 2000 m deep, noise free temperature log computed from the proxy-curve of *Esper et al.* [2002].

Figure 2.7, upper panel, shows selected reconstructions of the northern hemisphere annual mean surface air temperature (SAT) together with a reconstruction based on borehole temperature data [*Mann and Jones*, 2003; *Esper et al.*, 2002; *Huang et al.*, 2000]. In the following, the reconstruction of *Esper et al.* [2002] serves as a forcing function to compute the transient temperature perturbation along the depth of a borehole. The other parameters of the forward model are taken again from table 2.1. To compute the T-z profile, a pre-observational mean surface temperature needs to be specified (parameter T_0 in equation 2.1). As the proxy curve contains no information about this parameter, it was arbitrarily chosen to be the mean temperature of the curve in the interval 800 years to 1200 years before present. Figure 2.7, lower panel, displays an inversion result for this synthetic temperature log. The temperature data are noise-free and the log runs down to 2000 m. Because of the favourable conditions for this particular inversion, the information provided by this reconstruction can be considered to be the maximum that can be extracted by inverting temperature-depth data. The warming trend of the last 200 years is captured very well. The reconstruction does not reveal any climate variations of the preceding centuries

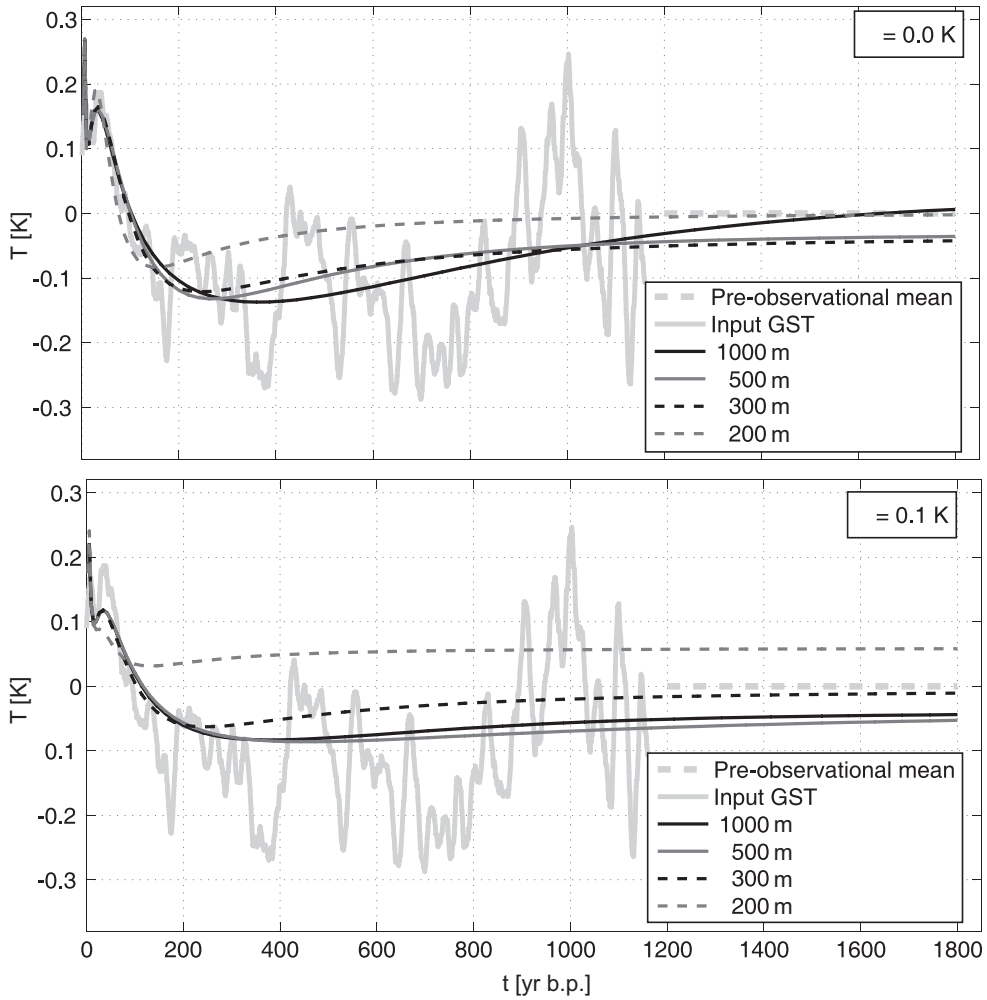

Figure 2.8: Inversion results for increasingly shallower temperature logs, truncated at different depths from 1000 m to 200 m. Thermal parameters are the same as in table 2.1. *Top:* Noise-free input temperature data using a damping parameter of $\epsilon = 0.1$. *Bottom:* Temperature data are disturbed by Gaussian noise with a standard deviation of $\sigma = 0.1$ K. A larger value of $\epsilon = 0.6$ was used in these cases.

but preserves the pre-observational mean. Thus the borehole method effectively provides two unknown pieces of information: (1) The average temperature of the last millennium and (2) the mean temperature before this period.

These conclusions only hold for optimum quality data. In reality, data are noisy and boreholes are often not sufficiently deep. Figure 2.8 compares inversion results where only shorter logs are available and noise is added to the data. For the case without noise, the average temperature of the last millennium can be resolved for logs with a depth of 300 m to 500 m. Inversion of shallower logs yield a strong reduction of the amplitude of the GST reconstruction. In the presence of noise even the 1000 m deep log fails to recover the mean temperature of the last

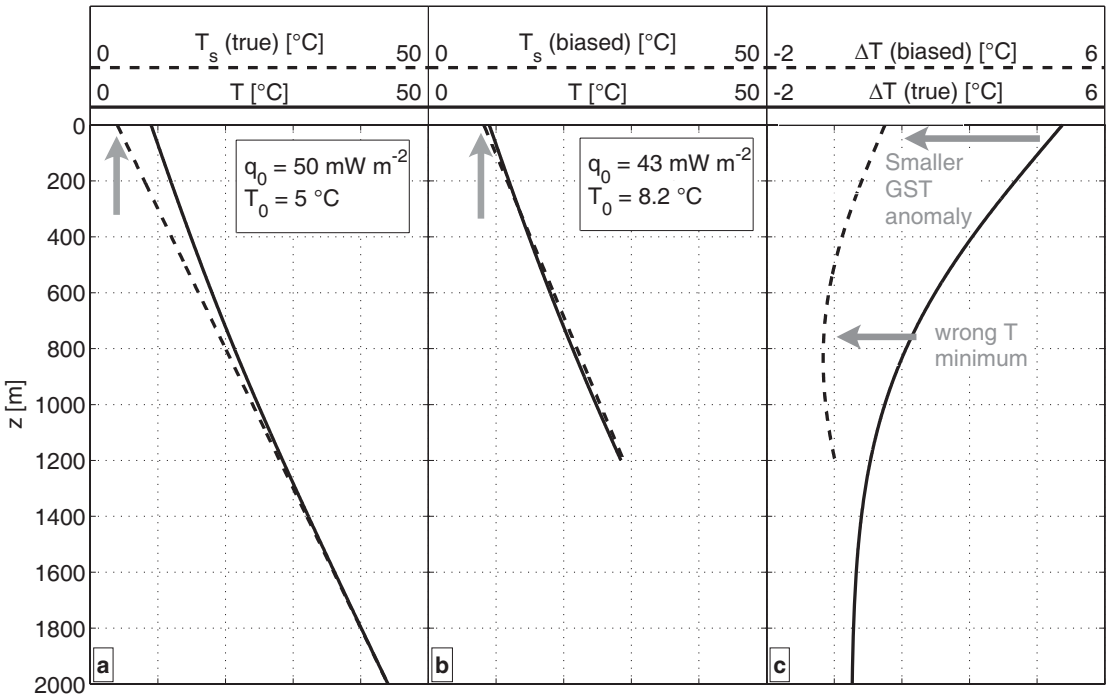

Figure 2.9: Example of a biased estimate of the steady-state gradient and ground surface temperature. *a)* Steady-state T-profile (dashed line) and corresponding transient profile (solid line) due to a step increase in GST. *b)* Truncated version of the transient log in (a) (solid line) and steady-state T-profile from regularised inversion of this log (dashed line). *c)* Transient temperature anomalies $\Delta T = T - T_s$, true (solid line) and biased (dashed line). The decrease in temperature anomaly and the introduction of a wrong temperature minimum for the biased case are highlighted.

1000 years. This differs from the results for pleistocene reconstructions which suffered only slightly from measurement noise. The reason is that the amplitude of the transient surface air temperature signal in the past few thousand years is one order of magnitude smaller than that of the post-glacial temperature rise (see figure 2.1). The SAT reconstruction used in the analysis as a driving function represents a global temperature average. At a specific site, however, the amplitude of the transient signal may be larger, yielding a better signal-to-noise ratio compared to the data in this analysis. Thus, in practise, the expected signal should be compared to the inherent noise of the data in order to assess if the desired signal can be extracted from these data.

Both types of GST reconstructions, millennial-scale and pleistocene-scale, show a strong dependence of the inverted GST history on shorter borehole depth and a systematic decrease of GST amplitudes and phase shifts of minimum or maximum temperatures in the record. This is caused by regularising the ill-posed inverse problem using a dampened singular value decomposition such as in the analysed algorithm. Section 2.3 discussed in detail the trade-off resulting from regularising: Besides preventing numerical instability of the result it also minimises the norm of the parameter vector. Usually this effect is desired to avoid unnecessarily complicated models [*Constable et al.*, 1987]. However, in our case a minimum solution in this sense will yield smaller GST variations than those which actually occurred. This causes additional problems since the

inversion also yields the mean GST T_0 and the surface heat flux density q_0. Figure 2.9 illustrates this problem: Panel (a) shows a temperature profile (solid line) due to a step increase in ground surface temperature and the corresponding steady-state temperature profile (dashed line). Panel (b) shows a temperature log truncated at 1200 m which is used to estimate simultaneously GST history, q_0, and T_0. The steady-state model in this case is biased towards higher and lower values for T_0 and q_0, respectively. True and biased temperature anomalies are compared in panel (c). The amplitude of the biased anomaly is reduced, corresponding to smaller GST variations in the model. Also, a wrong minimum is introduced in the reconstruction that is not present in the original GST history. Thus, the inverted GST history is in error. Instead of a step increase in GST it yields a decrease in ground surface temperature followed by a subsequent increase. Even if an optimum ϵ is chosen for the inversion, this problem will persist as it is inherent of the regularisation process. A different method of regularisation is therefore desirable and a subject of current research [*Rath and Mottaghy*, 2007].

2.4.2 Thermal parameters

The inversion procedure requires that thermal conductivity, thermal diffusivity, and heat production rate are known exactly. In reality, errors in these parameters can be minimised but never avoided altogether. For instance, errors may arise from preferential sampling of units that are not representative of the entire geologic sequence. Also, missing or wrong corrections for in-situ conditions with respect to temperature and pressure may cause systematic errors of the thermal rock properties. The following discussion analyses uncertainties in the inversion resulting from these systematic errors.

Thermal properties are relevant in three terms in the right hand side of the governing equation 2.1. Whereas heat production rate and thermal diffusivity appear only in one term each, thermal conductivity appears in all three of them, either directly or via the equation for thermal diffusivity $\kappa = \lambda/(\rho c)$. The analysis could proceed by discussing the relevant thermal properties one after another. However, it is more instructive to study the combined influence of each of the different terms of equation 2.1. The inversion procedure interprets curvature in the temperature log as a transient signal. Thus, only terms with a potential to create curvature in the equation will have an influence on the result.

Transient term The only rock property in the function $T_t(z,t)$ (equation 2.2) is thermal diffusivity κ. One may expect that this term will have the largest influence on the solution. Errors introduced by the transient term can be modelled by varying κ.

Heat production term Because of the quadratic depth dependence, the heat production term $Az^2/2\lambda$ contributes curvature to equation 2.1 which may misleadingly be interpreted as a transient signal. Because the heat production rate is usually small, the influence of this term is expected to be less important for boreholes of moderate depth. Heat production rate and thermal conductivity are inversely proportional in this term. Thus, to study the error associated this term,

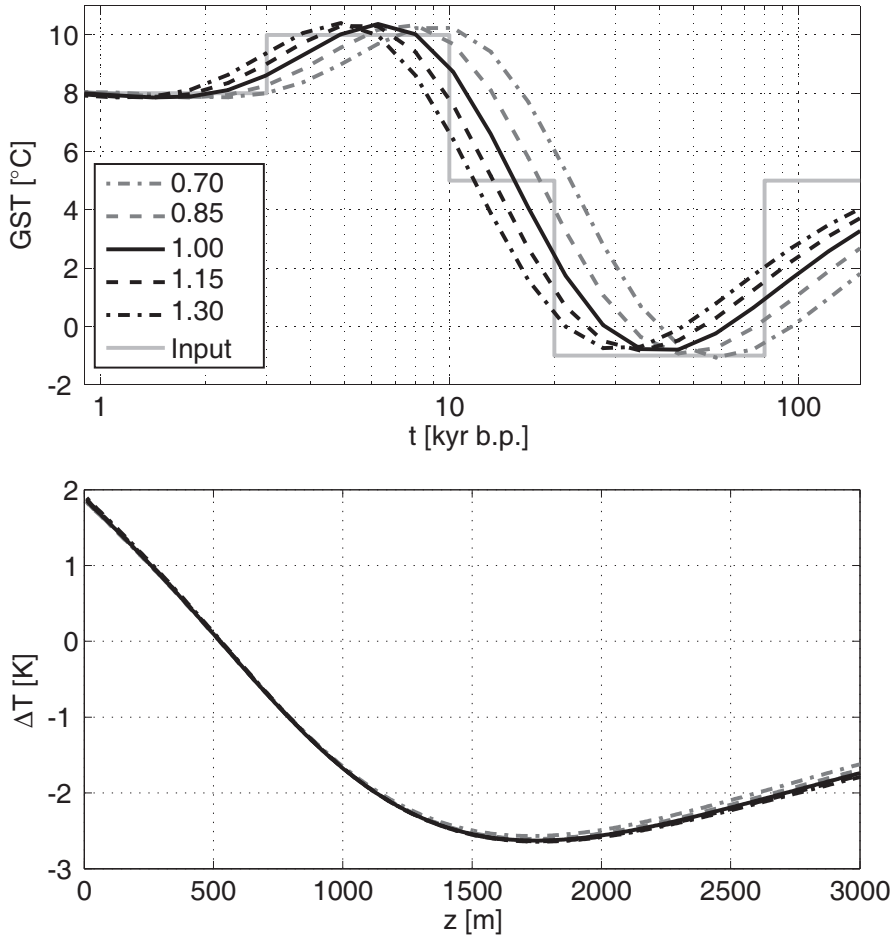

Figure 2.10: Systematic changes in thermal diffusivity shift the timing of the events. Thermal conductivity is varied from 70 % to 130 % of the original value. For better comparison, inverted curves are plotted as smooth lines rather than a series of step functions. *Top:* Input GST and inversion results for different values of thermal diffusivity κ (in 10^{-6} m^2 s^{-1}). *Bottom:* Different temperature anomalies ΔT corresponding to the GST's in the top panel.

the ratio of A/λ should be analysed. This can be done by either varying thermal conductivity or heat production rate. In the following quantitative analysis, heat production rate will be varied.

Steady-state heat conduction Thermal conductivity λ is the rock property governing the heat-conduction term qz/λ. In the framework of a homogeneous subsurface, this term contributes no curvature. Therefore, the GST reconstruction will be unaffected and it is not necessary to study the effect of the term here. The effect of a variable thermal conductivity is discussed in section 2.4.3. Also, one must be aware that an error in λ will cause a proportional error in the heat flux density.

In order to support this qualitative discussion with quantitative results, a synthetic temperature

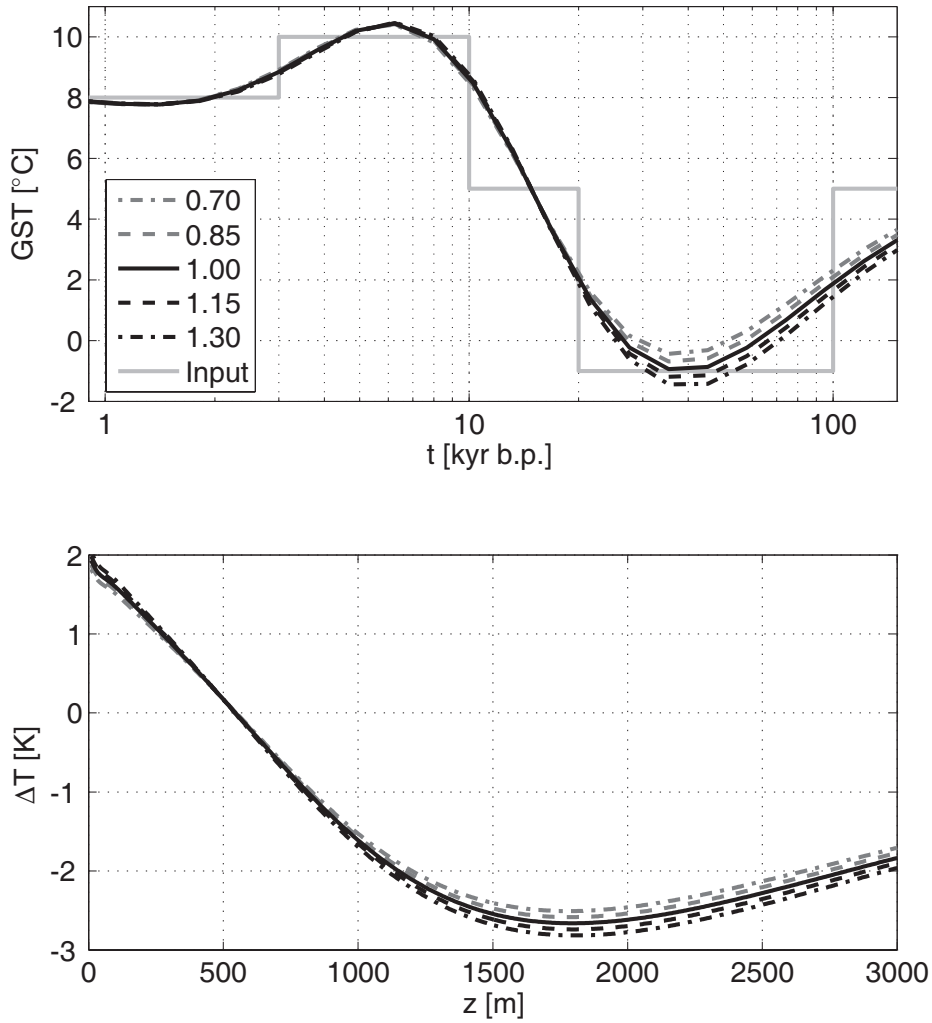

Figure 2.11: Systematic changes in heat production rate cause variations in the amplitude of the events. Heat production rate is varied from 70 % to 130 % of the original value. For better comparison, the inverted curves are plotted as smooth lines rather than a series of step functions. *Top:* Input GST and inversion results for different values of heat production rate A (in 10^{-6} W m^{-3}). *Bottom:* Different temperature anomalies ΔT corresponding to the GST's in the top panel.

log was inverted with systematic errors in thermal diffusivity and heat production rate in two separate inversion runs. The parameters were varied by $\pm 30\%$ relative to the original values of $\kappa = 10^{-6}$ m^2 s^{-1} and $A = 10^{-6}$ W m^{-3}. A simplified GST history was used in the forward model to compute the transient temperature anomaly. It comprises several step changes aimed to reflect the general magnitude and timing of the expected effects and not representing an actual GST history.

The results of these experiments are shown in figures 2.10 and 2.11. Variation of thermal diffusivity shifts the timing of events in the reconstructed time series. Phase shifts of the entire

reconstructions correspond to wrong estimates of thermal diffusivity. However, the amplitude of the inverted GST remains unaltered.

The heat production rate influences the amplitude of the paleoclimatic events but retains their timing. It is no surprise that this effect increases with time. This is consistent with the fact that the heat production term (equation 2.1) increases with the square of depth z. From figure 2.11 it is clear that only very large errors in heat production rate will become significant and only for boreholes deeper than 1000 m. In particular, they should be irrelevant for millennium-scale studies. Thermal diffusivity, in contrast, may change the timing of events on all time scales. Thus, it is important also for inversions on much shorter time scales than the ones considered here.

2.4.3 Heterogeneity

The previous discussion was restricted to the case of a homogeneous subsurface. In the following it will be studied whether the conclusions drawn are also valid for a heterogeneous medium. To address this question the impact of a heterogeneous, layered earth model on the inversion results is assessed. For this purpose, transient profiles computed by a finite-difference (FD) algorithm [*Rath and Mottaghy*, 2007] are considered as ground truth. Random variations of the thermal properties are introduced on increasing length scales for the analysis of inversion results. In addition to the effect of random variations, systematic changes with depth of thermal properties can be relevant. This is discussed qualitatively using a synthetic steady-state temperature profile of a sedimentary rock column where petrophysical changes arise from compaction of the material and elevated temperatures in the subsurface.

For the forward computation, a simplified GST history of the last 100 000 years is used, with a pre-observational mean of 5 °C. The profile is computed down to 10 000 m at a vertical resolution of 5 m. The analysis uses only the top 3000 m, the deeper parts are only necessary to avoid edge effects of the FD solution. Thermal parameters are those of table 2.1 if not specified differently.

The largest influence on the temperature profile will derive from variations in thermal conductivity. Deviations from the constant temperature gradient corresponding to the steady-state conditions will be interpreted misleadingly as noise or paleoclimate. To study separately the effects of thermal diffusivity and thermal conductivity for a given temperature profile, the inverse algorithm is modified. The steady-state part of the equation is cast in terms of the Bullard depth z_b [*Bullard*, 1939], for the homogeneous case defined by $z_b = z/\lambda$, physically a thermal resistance. Consider the differential equation for 1D heat transport in a homogeneous medium:

$$\frac{\partial^2 T}{\partial z^2} = \frac{1}{\kappa}\frac{\partial T}{\partial t} + \frac{A}{\lambda}. \tag{2.5}$$

Substituting $\partial z = \lambda \partial z_b$ yields

$$\frac{\partial^2 T}{\lambda^2 \partial z_b^2} = \frac{1}{\kappa}\frac{\partial T}{\partial t} + \frac{A}{\lambda}, \tag{2.6}$$

$$\Rightarrow \frac{\partial^2 T}{\partial z_b^2} = \frac{\lambda^2}{\kappa}\frac{\partial T}{\partial t} + \lambda A. \tag{2.7}$$

Thus if $\kappa' = \kappa/\lambda^2$ and $A' = A/\lambda^2$, equation 2.1 can be written as:

$$\begin{aligned} T(z_b) &= T_0 + q_0 z_b + \frac{A' z_b^2}{2} \\ &+ \sum_{j=1}^{N} T_n^G \left(\text{erfc}\left(\frac{z_b}{2\sqrt{\kappa' t_j}} \right) - \text{erfc}\left(\frac{z_b}{2\sqrt{\kappa' t_{j-1}}} \right) \right). \end{aligned} \tag{2.8}$$

Using the transformed variables and taking the heat production term to the left-hand side, the steady-state part of the profile can be reduced to the problem of a homogeneous half-space with constant thermal resistance. The transient term still contains the depth dependent property κ'. However, this will be assumed to be constant with depth.

The input data will always be computed using variable thermal conductivity and diffusivity. Using either the normal or the transformed model for the inversion, two configurations with wrong assumptions are possible; (1) Constant λ and κ; (2) Constant κ only. This configuration allows to separate the effects of variable thermal diffusivity and conductivity. Thermal diffusivity variations can be analysed by introducing an error in the diffusivity while at the same time keeping the correct model for the steady-state part of the profile.

The noise on varying vertical length scales is studied by modifying the FD model to compute the temperature profiles. The layers of the model are assigned random values of thermal conductivity with a mean of 2.5 W(m K)^{-1} and a standard deviation of 0.5 W(m K)^{-1}. Volumetric heat capacity is held constant throughout the experiment, resulting in a simultaneous variation of thermal conductivity and diffusivity. Ten different configurations are considered with layer thickness x increasing from 5 m to 1000 m. For each configuration 50 realisations of the thermal conductivity-depth profile are generated. These are then used in the forward model to compute 50 temperature depth profiles. Additionally, temperature profiles for an equivalent half-space and for a layered representation (equation 2.8) are computed. An example of this computation is given in figure 2.12. Two realisations of the resulting thermal conductivity profile for length scales of 5 m and 200 m are shown. The differences between the "true" temperature profile and the two profiles with assumptions are shown in figure 2.13. The misfit of the equivalent homogeneous model is large because variations in the steady-state temperature profile are not reflected in the homogeneous model. This emphasises the importance of information on thermal conductivity. In contrast, the model with homogeneous κ shows only deviations of the order of a few mK, suggesting that random variations of thermal diffusivity are smoothed out.

Next, the random data are used as input to the inversion procedure. For each inversion the value and timing of the maximum temperature in the Holocene is recorded in order to compress the results (figure 2.14). To accommodate the increasing misfit between model and data for increasing noise length scale, the damping parameter is increased from $\epsilon = 0.35$ to $\epsilon = 1$, qualitatively reflecting an increase in noise length scale from 5 m to 1000 m. This results in stronger attenuation and is reflected in the decrease of the maximum temperature value because models with smaller norms are preferred for large ϵ. The influence of noise on the result becomes most pronounced for length scales larger than 100 m when the scale of the signal is on the order of the noise scale. The timing of the event is modified in a similar way.

In crystalline rocks, random variations of thermal properties might prevail. In contrast, in

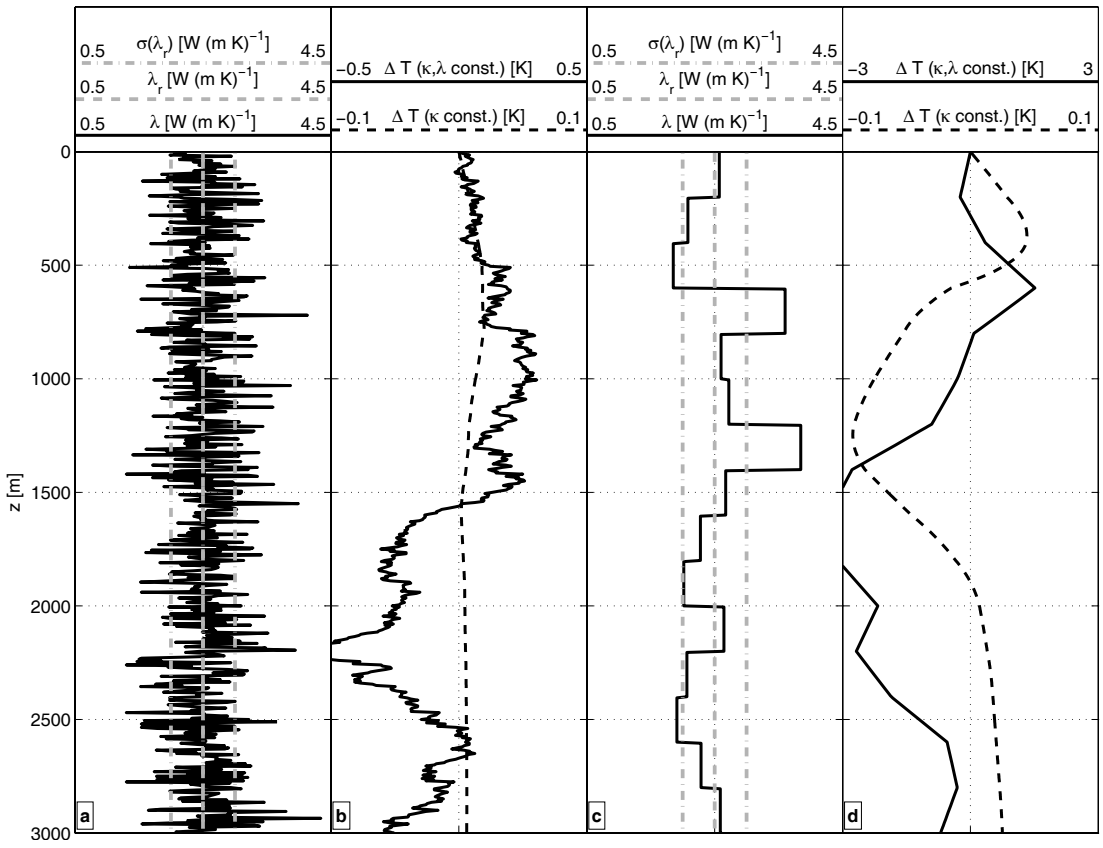

Figure 2.12: Examples for realisations of the random heterogeneous model. *a)* Length scale of noise is 5 m. Shown are mean value (λ_r) and standard deviation ($\sigma(\lambda_r)$) of the normal distribution and one random realisation (λ). *b)* Based on the λ profile in panel (a) differences ΔT are computed between the FD model and the models with constant κ and with both constant κ and λ. *c)* Same as for panel (a), but for a noise length scale of 200 m. *d)* Same as for panel (b) but based on profile of panel (c).

sedimentary rocks systematic changes are much more important. Changing depositional environments throughout time create diverse rock types. The influence on the inversion depends on the particular setting. One aspect that is often neglected is the variation of thermal properties in uniform sequences of rock due to the temperature dependence of thermal properties and the compaction with increased overburden. In figure 2.15 a geologic profile of a single rock type is considered. The thermal conductivity of the matrix is taken as $\lambda = 3.5$ W(m K)$^{-1}$. An exponential decrease of porosity due to compaction is assumed, sometimes referred to as Athy's law [*Athy*, 1930], with a surface porosity of 0.45 and a characteristic depth of 750 m [*Allen and Allen*, 1990]. Thermal conductivity of the matrix is taken inversely proportional to temperature [*Haenel et al.*, 1988] and volumetric heat capacity of the matrix is approximately proportional to temperature in the range considered [*Rath and Clauser*, 2005]. For simplicity, the pore fluid is assumed to be fresh water. Its thermal properties are taken from reference tables [*Wagner and Pruß*, 2002]. Temperature and heat flux density at the surface are 10 °C and 0.06 W m^{-2}, respectively.

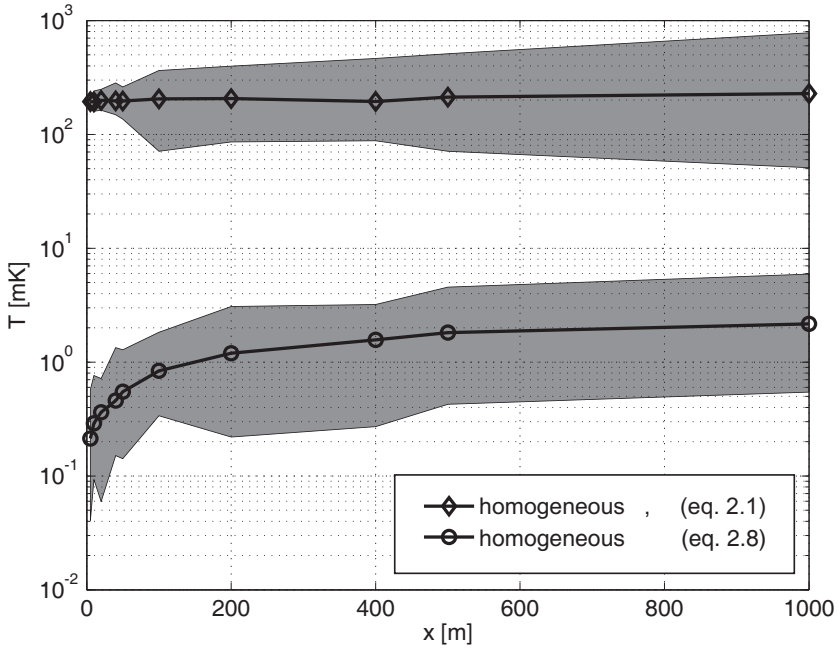

Figure 2.13: Misfit ΔT between temperature profiles computed from the FD-model and homogeneous models for varying vertical length scales x. Mean RMS-values are given for a homogeneous subsurface ($\diamond$) and for homogeneous κ only ($\circ$). Grey shading denotes minimum-maximum range.

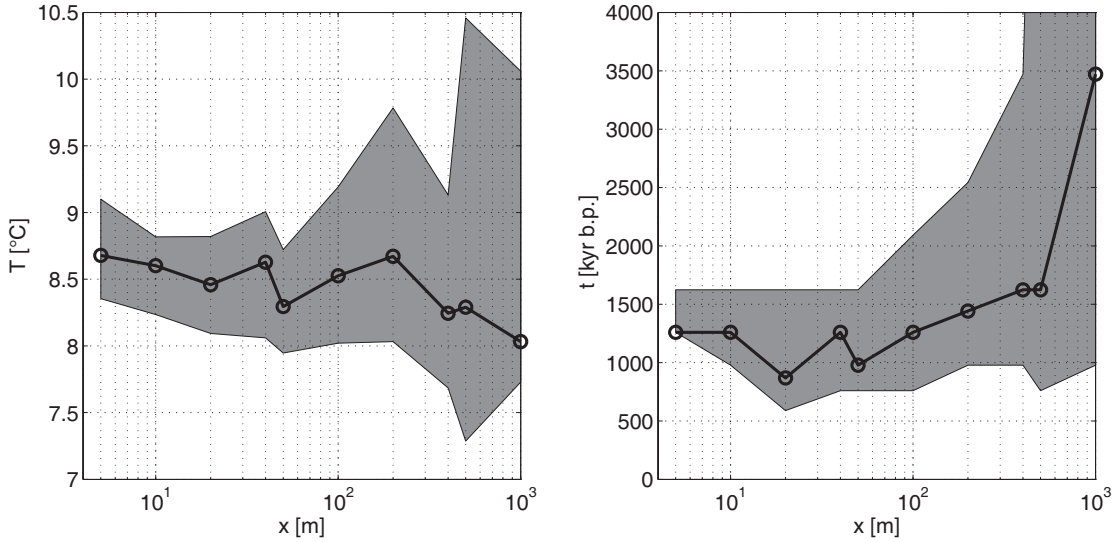

Figure 2.14: Variation of the amplitude T (*left*) and timing t (*right*) of the maximum temperature in the Holocene versus the vertical length scale of the random noise as defined in the text. Grey shading denotes 75 % quantiles of all realisations.

These assumptions result in a strong variation of the thermal properties with depth (figure 2.15 c). Bulk thermal conductivity λ increases considerably, due to the decreasing amount of low-

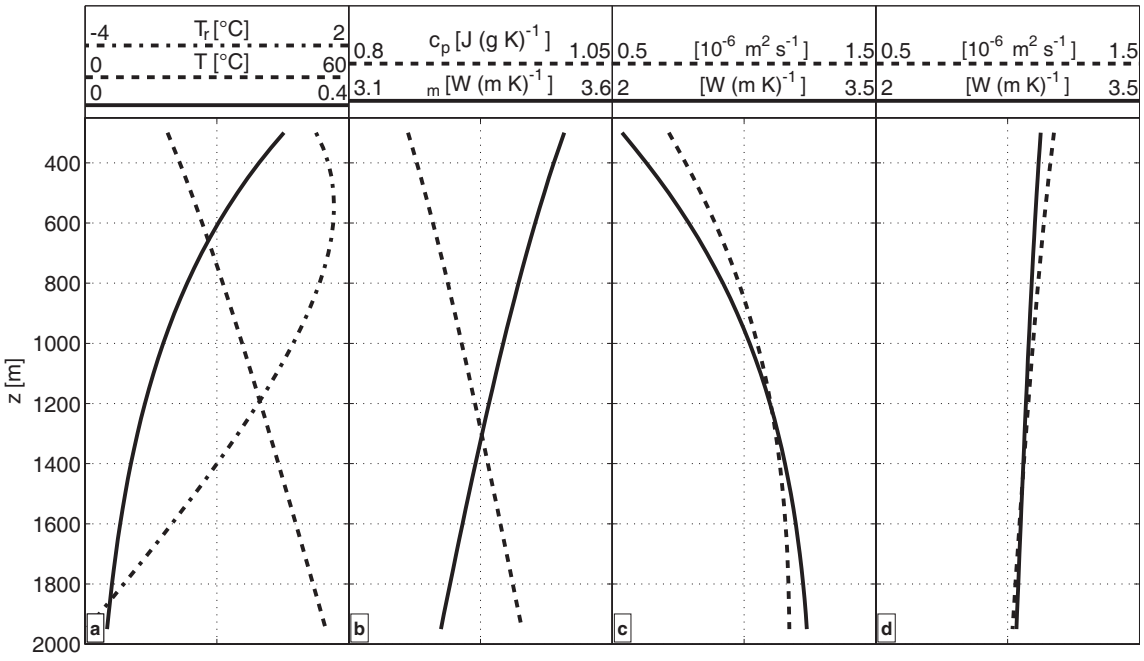

Figure 2.15: Systematic variation of thermal properties with depth. *a)* Porosity ϕ, temperature T, and reduced temperature T_r. *b)* Thermal conductivity λ_m and specific isobaric heat capacity c_p of the rock matrix, depending on temperature. *c)* Effective thermal conductivity λ and diffusivity κ using porosity from panel (a) and a geometric mixing law. *d)* Effective thermal properties for a constant porosity of 0.1, assuming a geometric mixing law.

conductivity fluid with depth. With an increase of over 50 % in λ, it is clear that the porosity decrease is the dominant factor and masks the influence of temperature. Thermal diffusivity κ increases by over 60 %. Similar to thermal conductivity, the effect is caused by compaction rather than a temperature effect. Volumetric heat capacity (ρc) of the rock decreases because the amount of water, having a high heat capacity, is reduced with depth. The strong curvature of the profiles is reflected in the reduced temperature T_r (figure 2.15 a) for this case. Obviously, an assumption of a constant conductivity or diffusivity will cause errors in the interpretation of the resulting temperature anomaly (T_r in panel a). The type of curvature introduced in the temperature profile by the variation of rock properties with depth is similar to a paleoclimatic signal in magnitude and length scale.

For comparison, effective thermal rock properties are also shown for a constant porosity of 0.1 for an appraisal of only the temperature and pressure effects (figure 2.15 d). Thermal conductivity and diffusivity experience a decrease of 5 % and 15 %, respectively, over the depth range considered. The matrix value of thermal conductivity decreases strongly with temperature but this is partly offset by an increase in water conductivity, resulting in only a moderate decrease of effective conductivity. Specific heat capacity of the matrix increases with temperature while specific heat capacity of the fluid remains nearly constant. Together with nearly constant bulk density, this yields an increasing volumetric specific heat capacity. Thus, for thermal diffusivity $\kappa = \lambda/(\rho c)$ the denominator increases and the numerator decreases, leading to a stronger

decrease as for thermal conductivity. However, a treatment of the subsurface as homogeneous might be justified because variations of λ are small and variations of κ will, according to the previous discussions, modify the result but do not render it useless.

Both cases, an exponentially decreasing porosity and a constant porosity are idealised. In reality, sedimentary sequences will have properties somewhere in between these two cases. However, the comparison shows that compaction cannot be ignored, whereas temperature and pressure effects might be neglected. It is therefore prudent to analyse the gradual, systematic changes of rock properties prior to a GST inversion of temperature data.

2.5 Case study: KTB

A temperature log assumed to be in equilibrium was recorded in the KTB (see figure C.2 for well location) pilot hole down to 3990 m on September 17, 1997 and analysed in *Clauser* [1999]. An earlier recording, dating from February 1996, was analysed in detail for thermal processes, including transient effects of paleoclimate [*Clauser et al.*, 1997]. Shallow temperature logs in the vicinity of the KTB site have also been interpreted in terms of paleoclimatic influence [*Clauser and Mareschal*, 1995; *Clauser*, 1999]. In the light of the previous sections, the analysis of the KTB borehole is revisited and the uncertainties connected with the interpretation are discussed. In that study the temperature data was inverted for paleoclimate in the period from 10^5 to 10^2 years before present, using 100 time steps, a thermal conductivity of 2.92 W (m K)$^{-1}$, a thermal diffusivity of 10^{-6} m^2 s^{-1}, and a heat production rate of 1.1 μW m^{-3}. The analysis yielded a peak-to-peak amplitude of 10 K for the temperature increase from the latest glacial stage to the Holocene.

The geological profile in the KTB pilot hole is primarily composed of two lithologies: Metabasites and gneisses. These can easily be separated using the Gamma-ray-log (SGR) (figure 2.16). Thermal conductivity (figure 2.16) does not seem to vary systematically over the depth of the borehole, justifying the assumption of a homogeneous half-space. The mean thermal conductivity is (2.93 ± 0.60) W(m K)$^{-1}$. This value reduces to 2.82 W(m K)$^{-1}$ if a temperature and pressure correction is applied to the data [*Buntebarth*, 1991]. Knowledge of the thermal diffusivity is much more uncertain. For Gneiss a range of $(0.5 - 1.2) \cdot 10^{-6}$ m^2 s^{-1} is reported, for Amphibolites a range of $(0.6 - 0.8) \cdot 10^{-6}$ m^2 s^{-1} [*Čermák and Rybach*, 1982]. *Seipold* [1995] measured a value of $(0.8 \pm 0.2) \cdot 10^{-6}$ m^2 s^{-1} for Amphibolite samples from neighbouring sites. Again, a correction for temperature and pressure of the value given by *Seipold* [1995] reduces the mean diffusivity to a value of $0.70 \cdot 10^{-6}$ m^2 s^{-1}. Heat production rate is computed from spectral and total γ-ray logs [*Rybach*, 1988; *Bücker and Rybach*, 1996], yielding values of (1.19 $\pm$ 0.46) μW m^{-3} and (1.23 $\pm$ 1.14) μW m^{-3}. A value of 1.2 μW m^{-3} is used in the inversion.

The next step in the analysis is the choice of the optimum regularisation parameter ϵ. Figure 2.17 shows the L-curve for varying values of ϵ. The optimum choice seems to be $\epsilon = 0.4$, the value also chosen in the study of *Clauser et al.* [1997]. Figure 2.18 illustrates this in more detail showing inverted time series for the different values of ϵ. The direct comparison of results is particularly helpful to analyse which features of the GST history are numerical oscillations and which ones represent actual information. At a level of $\epsilon = 0.4$, oscillations that change the

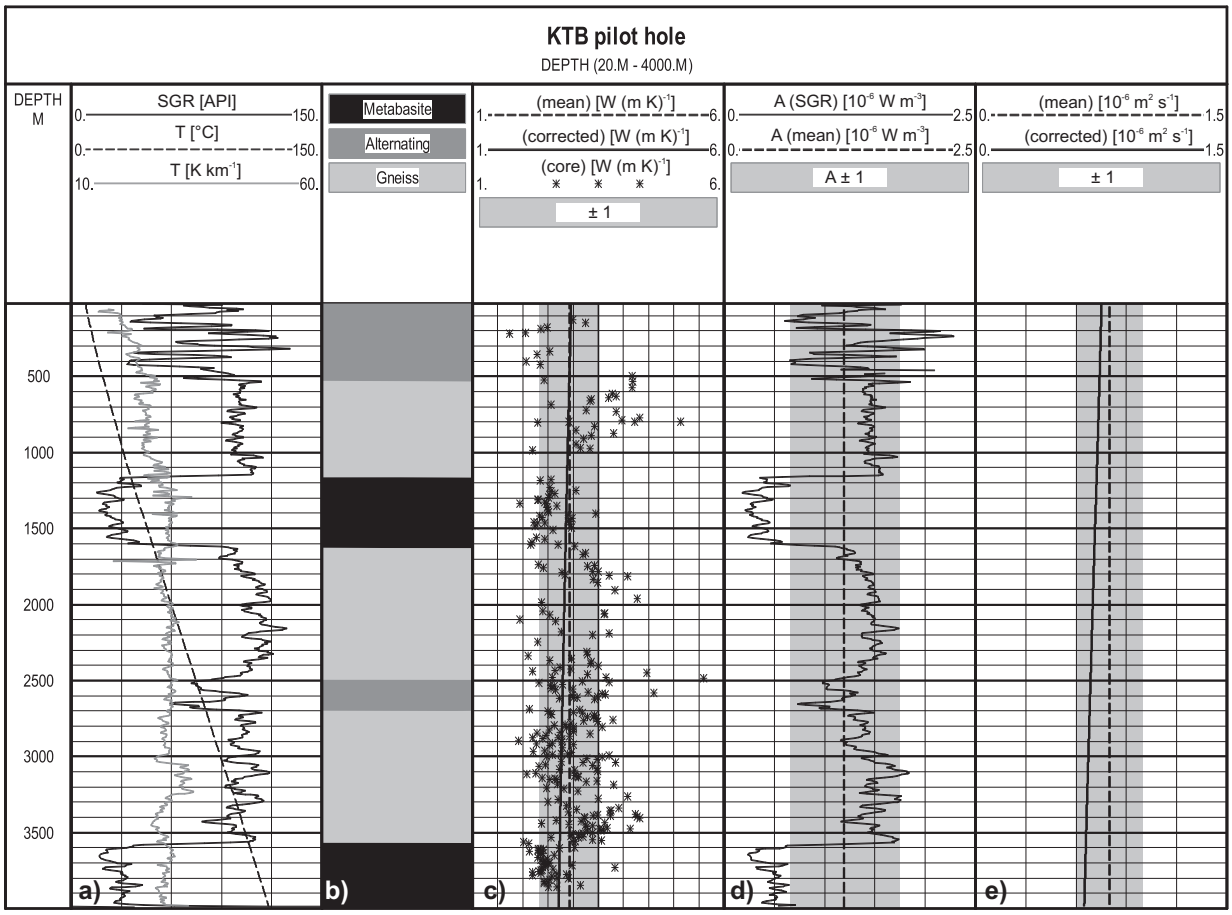

Figure 2.16: Composite log of the KTB pilot hole. *a)* Spectral Gamma Ray (SGR), temperature (T), temperature gradient (∇T). *b)* Generalised lithology. *c)* Core thermal conductivity (λ core) [*Clauser et al.*, 1997], mean value (λ mean), standard deviation of the mean value ($\lambda \pm 1\sigma$), thermal conductivity corrected for temperature and pressure (λ corrected). *d)* Heat production rate from spectral gamma ray (A SGR), mean value (A mean), standard deviation ($A \pm 1\sigma$). *e)* Mean thermal diffusivity from cores (κ mean), corrected for PT-conditions (κ corrected), standard deviation of the core measurements ($\kappa \pm 1\sigma$). Logging data courtesy of the KTB project management (`http://www.icdp-online.org`).

warming amplitude seem to be attenuated. A more conservative interpreter might choose an even higher value of $\epsilon = 0.6$, but in this range of ϵ-values the main features are only changed by a few tenths of a Kelvin.

Following the choice of the damping parameter, the detrimental effect of a reduced log length will be illustrated. The maximum depth of originally 3990 m is successively truncated to lengths of 3000 m, 2000 m, and 1500 m. Figure 2.19 shows the reconstructed GST history and transient temperature perturbation in the borehole for these truncation depths. The differences in this example are similar to those analysed in section 2.4.2.

Deviations from the inversion result for the full depth of the temperature log become significant for depths of less than 3000 m. The minimum temperature of the last glacial stage increases

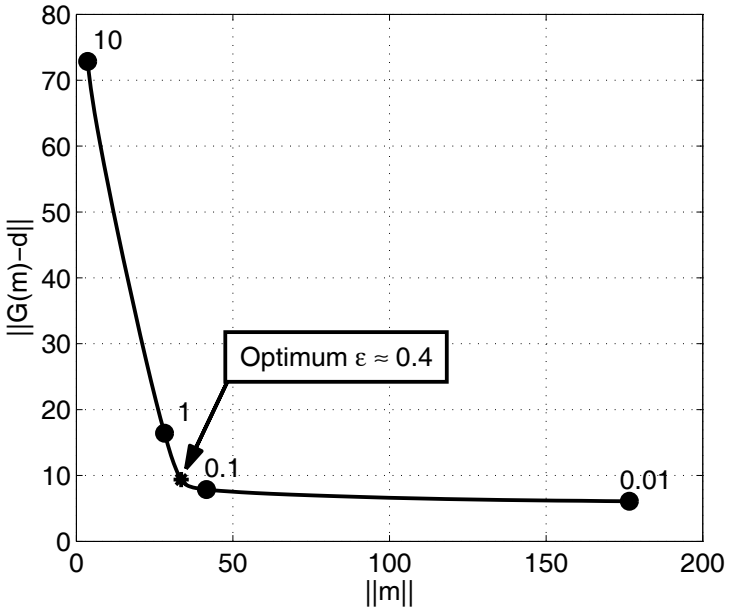

Figure 2.17: L-curve for the inversion of the KTB pilot hole-temperature log.

Table 2.2: Inversion results for the KTB log, truncated at successively smaller depths. The inverted parameters vary systematically with the depth of the log.

Depth [m]	T_0 [°C]	q_0 [W m^{-2}]	∇T [mK m^{-1}]
4000	4.14	0.0863	29.6
3000	4.70	0.0848	29.6
2000	5.51	0.0818	28.0
1500	6.15	0.0781	26.7

and the temperature maximum in the Holocene is shifted, consistent with the discussion in section 2.4.1. Table 2.2 shows the inversion results for the steady-state GST T_0, the surface heat flux density q_0, and the steady-state temperature gradient ∇T. This emphasises that the systematic variation of the GST history is accompanied by a corresponding change in the steady-state parameters. As discussed before with respect to the length of temperature logs, the heat flux density value decreases whereas the steady-state ground surface temperature T_0 increases. This is consistent with inverting a step increase in ground surface temperature using a log that is too short to fully resolve the GST history. It can be expected from this data that crustal heat flux density estimates may be too low if a paleoclimatic correction is used based on insufficiently deep temperature data. In this case this amounts to 8 mW m^{-2}, about 10 % less than the value obtained for the inversion of the full depth temperature log. The amount by which an undisturbed heat flux density value is underestimated depends on (1) the maximum depth of the temperature log used for the inversion and (2) the magnitude of the paleoclimatic variation at the site of the

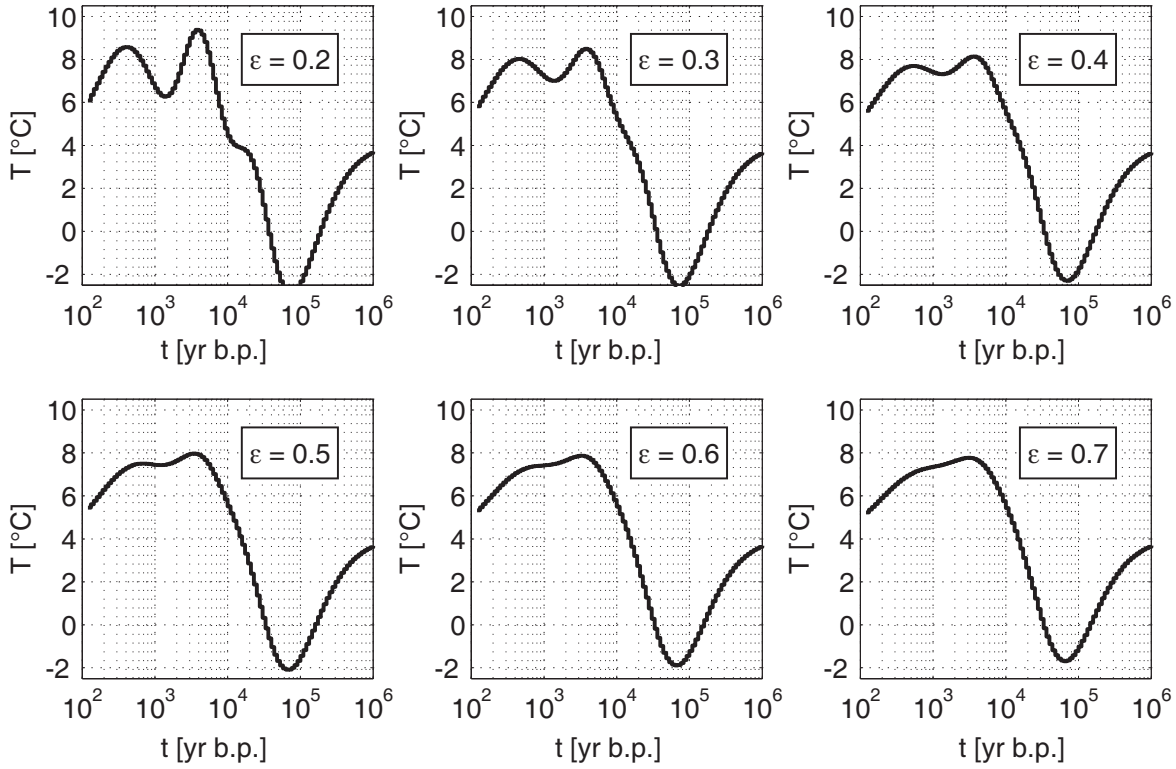

Figure 2.18: Inverted GST histories $T(t)$ for increasing values of the damping parameter ϵ.

borehole. While the former effect can be estimated using synthetic forward models of differing depths, as was done here, the latter influence is much harder to estimate because this requires information on the paleotemperature prior to the inversion.

2.6 Conclusions

The sensitivity analyses in the previous sections show that the inversion results depend strongly on data quality. Which aspects of data quality are most important is determined by the amplitude of the GST changes to be analysed. The amplitude is roughly equivalent to the time scale of the inversion: One can distinguish millennial scale inversion and glacial reconstruction with amplitudes on the order of 1 °C and 10 °C, respectively.

For inference of the post-glacial temperature increase, the minimum depth of the temperature log needed is the most challenging requirement. If it is met, the inversion is robust against noise in the temperature data. A depth of more than 3000 m seems to be required to resolve the post-glacial temperature increase adequately. Unfortunately, undisturbed temperature logs of this depth are rare. In contrast, reconstructions of the last millennium require only modestly deep logs. A depth of about 300 m to 500 m is suitable to derive a mean temperature for the last 1000 years. The exact values will depend on the magnitude of the noise and the transient

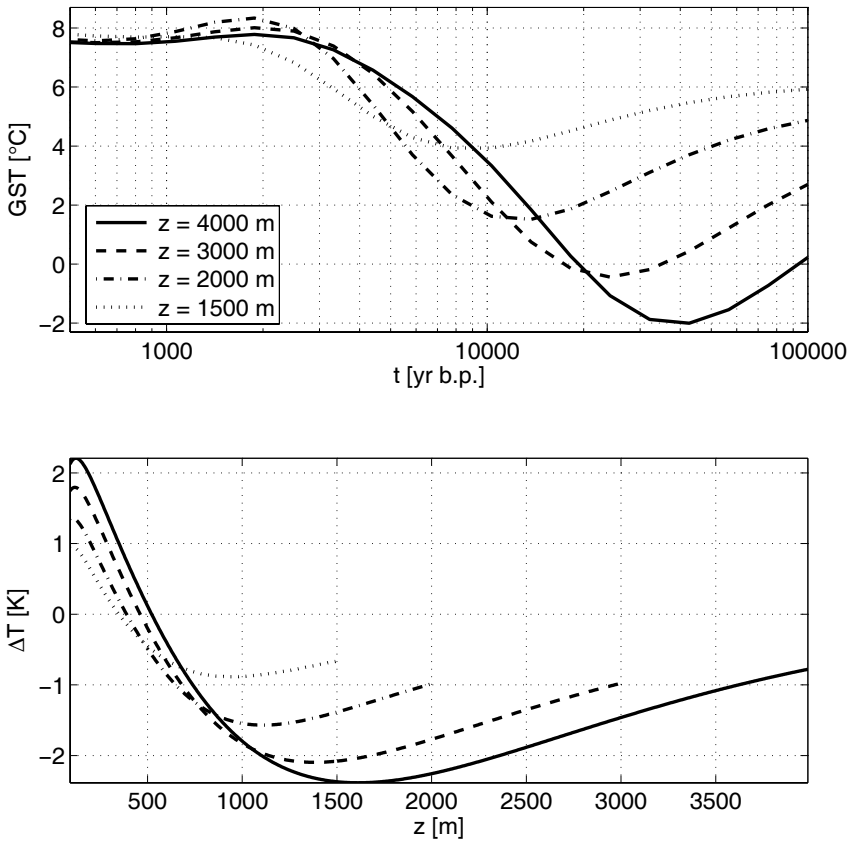

Figure 2.19: Inversion results for the KTB log for different depths of the log. *Top:* Inverted GST history for different log lengths. For clarity, the step amplitudes of the GST histories are shown as continuous lines. *Bottom:* Variation of transient temperature signalΔT with depth z.

signal at a specific site. For instance the IHFC database[2] for borehole temperatures and climate reconstruction lists 473 out of 754 temperature logs with a maximum depth greater than 300 m. However, this type of inversion demands on data of high quality. Even a noise level of 0.1 K may seriously degrade the inversion results.

Incorrect values of thermal diffusivity and heat production rate seem not to be the main source of error. The diffusive nature of the signal and the spreading over a wide depth range greatly mitigate the influence of the thermal diffusivity. The importance of the heat production rate increases with the length of the reconstructed time series. But even for studies of the last 100 000 years, errors introduced by incorrect assumptions of the heat production rate will be small compared to the influence of the log depth. The effect of thermal conductivity is twofold: (1) Unaccounted random variations increase the noise level, requiring a stronger regularisation, and thus reduce the amplitude of GST variations; (2) Systematic changes, in particular those causing only a mild variation with depth, have the potential to render results useless if they remain unnoticed. Thus,

[2] `http://www.geo.lsa.umich.edu/~climate`

a complete, temperature and pressure corrected thermal conductivity profile is highly desirable for obtaining best results. This aspect will be discussed further in chapters 3 and 4.

The studies on the regularisation parameter ϵ show that a thorough noise analysis should accompany any attempt to invert GST histories from geothermal data. An appropriate choice of the regularisation is crucial and should be justified by some objective means. A non-optimum choice of the regularisation can easily produce artefacts that are much larger than the calculated model errors. Particularly, selecting too small a value for ϵ introduces numerical oscillations that could be misinterpreted as a real variation of paleotemperatures. Here, the L-curve criterion was used, but other methods like generalised cross validation [e.g. *Hansen*, 1998; *Haber and Oldenburg*, 2000; *Aster et al.*, 2004] or truncated iterative methods [e.g. *Hansen*, 1998; *Hanke*, 1995; *Berglund*, 2002] may be used as well.

Finally, although the least-squares fit with a Tikhonov regularisation which minimises the model norm is common practise in solving ill-posed problems, it might not be necessarily the best choice, as pointed out by *Hansen* [1998]. Other regularisation methods might preserve the information contained in borehole temperatures better. These include Bayesian-type smoothing approaches [*Şerban and Jacobsen*, 2001] as well as nonlinear minimum support regularizers [*Portniaguine and Zhdanov*, 1999; *Zhdanov and Tolsataya*, 2004]. Research in the development of novel approaches to regularisation and the incorporation of prior knowledge are important tasks for the future.

Chapter 3

Thermal properties from core and logging data

The previous discussion showed that systematic variations of thermal conductivity with depth may flaw a paleoclimatic reconstruction. In such a case, in particular in sedimentary basins with strong variations of petrophysical properties, a continuous profile of thermal conductivity is highly desirable. This can be obtained either from an extensive analysis of core samples or from interpreting borehole geophysical data. This chapter studies an example from Southern Germany where core data and wireline data are analysed jointly to obtain a complete section of thermal conductivity.

This study was part of a research project that used geothermal methods to determine groundwater flow rates in the deep subsurface [*Clauser et al.*, 2002; *Rath and Clauser*, 2005]. This requires to determine accurately and separately from each other the effects of the different heat transport processes: Steady-state heat conduction, transient heat diffusion, and heat advection by groundwater flow. Computing the steady-state conductive temperature field requires detailed thermal conductivity data. Two requirements should be met: First, lateral variations in thermal conductivity have to be known accurately for regional studies. Second, a detailed analysis of a particular borehole requires a high-resolution thermal conductivity profile. Core material often is either confined to a few boreholes or available only for a particular layer, violating both requirements. Standard geophysical logging data offer better depth resolution. In a situation with an incomplete coring sequence this may prevent biased sampling in lithologies not representative of the full sequence. Spatial coverage can be improved as well, particularly in sedimentary basins with past or present hydrocarbon exploration activity.

3.1 Direct and compositional methods

The problem of determining thermal conductivity from well log data has been subject of research for quite some time. A review of methods for computing thermal conductivity from wireline logs is given in *Blackwell and Steele* [1989]. They can be classified into two main categories [*Beardsmore and Cull*, 2001; *Blackwell and Steele*, 1989]: The first approach relates one or

Table 3.1: Coefficients for equation 3.1 [*Vacquier et al.*, 1988]. The equation establishes a multi-linear relation between specific logging measurements and thermal conductivity.

Rock Type	a_0 [W (m K)$^{-1}$]	a_1 [W m^2 (g K)$^{-1}$]	a_2 [10^{-3} W (µs K)$^{-1}$]	a_3 [W (m K)$^{-1}$]	a_4 [W (m K)$^{-1}$]
Sand	-0.8445	1.803	-2.912	1.714	-3.228
Carbonates	2.863	-0.5305	-1.570	1.405	-0.003931
Argillaceous rocks	1.954	-0.3684	-0.3016	3.138	-1.368
Mixture of the three types	9.148	-2.662	-5.115	1.914	-0.5003
Sandy Limestones & Dolomites	-1.463	0.1000	12.05	1.960	-1.558
Limy & dolomitic Shales	1.837	-0.03033	-1.215	1.250	-0.5501
Shaly Sands	-3.428	0.7178	3.669	7.038	-1.218

more logging measurements or some derived property directly to thermal properties via empirical relationships. This method has been used to compute thermal conductivity in a number of studies [*Goss et al.*, 1975; *Evans*, 1977; *Vacquier et al.*, 1988; *Doveton et al.*, 1997; *Goutorbe et al.*, 2006]. For example *Vacquier et al.* [1988] used data from two oil wells in France. A direct empirical relationship was used for calculating thermal conductivity λ:

$$\lambda = a_0 + a_1\rho_b + a_2\Delta t + a_3(1-\phi_n) + a_4 V_{sh}. \tag{3.1}$$

Here the a_i are empirical constants determined from laboratory measurements by multiple regression. The resulting effective thermal conductivity λ is given in $\mathrm{W(m\,K)^{-1}}$, while input bulk density ρ_b should be given in $\mathrm{kg\,m^{-3}}$, slowness Δt in $\mathrm{\mu s\,m^{-1}}$, and neutron porosity ϕ_n in fractional porosity values. Volume of shale V_{sh} is computed from the γ-ray log GR by linear interpolation between the shale value GR_{sh} and the clean sand value GR_{sn}:

$$V_{sh} = \frac{GR - GR_{sn}}{GR_{sh} - GR_{sn}} \tag{3.2}$$

Different sets of coefficients were determined for differing lithologies (table 3.1). This approach is quite simple to implement, but requires a specific set of logs.

In the second approach, the major mineral or rock components are identified and the volumetric fractions of these components are derived from analysing regular wireline data. Using thermal conductivity values for each component, one can then compute the effective thermal conductivity assuming an appropriate mixing law (see for instance *Brigaud et al.* [1990]; *Williams and Anderson* [1990]; *Demongodin et al.* [1991]; *Lucazeau et al.* [2004]). This approach is more flexible than the first one. For instance, it does not require the same suite of logs in each borehole as long as they are suitable to compute component volumes. *Brigaud et al.* [1990] conducted a study on three wells in the Uinta Basin. They used a four component geometric mixing model for rock computing the effective thermal conductivity λ_e:

$$\lambda_e = \prod_{i=1}^{4} \lambda_i^{V_i} \tag{3.3}$$

with the following constituents: sandstone, shale, carbonate, and void (water filled) volume. The fractional volumes V_i of the three rock types are determined from lithological logs based on core cuttings from the wells. Porosity was calculated using two methods: (1) From the sonic log Δt using Wyllie's travel time equation

$$\phi_s = \frac{\Delta t - \Delta t_m}{\Delta t_f - \Delta t_m}. \tag{3.4}$$

Here Δt_m is the slowness in the matrix and Δt_f is the slowness in the pore fluid; (2) From the neutron porosity log ϕ_n by correcting it for the shale volume V_{sh}:

$$\phi_{ns} = \phi_n - \phi_{sh} \cdot V_{sh}, \tag{3.5}$$

where ϕ_{ns} is the corrected neutron porosity value and ϕ_{sh} is the shale value of the neutron porosity log.

The matrix thermal conductivities for different rock types were determined by laboratory measurements and subdivided into the main formations found in the Uinta Basin. *Brigaud et al.* [1990] found that their prediction of λ_e yielded an accuracy better than 20 % for 90 % of the samples.

It has been pointed out [*Goss et al.*, 1975; *Blackwell and Steele*, 1989] that results, in particular those of direct and empirical methods, are restricted to a geographical region or geological setting. Mixing law methods tend to yield better results than direct empirical methods because more information can be incorporated on the lithology and structure of the rock. However, they generally require a full suite of well logs and costly interpretation of the data. This can be a disadvantage when old data is used where not all modern logs were recorded and documentation of the data is poor. In the following, a set of parameters is derived that allows computing of thermal conductivities for the Tertiary Flysch sequence of the Molasse Basin located in Southern Germany. Because this area was explored for hydrocarbons decades ago, the possibility of using older and incomplete log data from this area is also evaluated. This analysis is preceded by an analysis and comparison of possible mixing laws for computing the effective thermal conductivity.

3.2 Choice of an appropriate mixing law

Mixing-law models allow to compute thermal conductivity from rock composition. Regardless of the source of this data, be it wireline data or a mineralogical analysis, it is necessary to decide on the most appropriate way to compute the effective thermal conductivity. Figure 3.1 illustrates this problem in a plot of the ratio of dry over water-saturated thermal conductivity versus porosity based on measurements of different studies: Data Set 1 consists of average values from 13 studies with a total number of 897 samples, measured on sedimentary rocks from Russia [*Popov et al.*, 1990; *Kobolev et al.*, 1990; *Popov et al.*, 2003a]. Set 2 comprises 58 samples of oceanic Basalt from DSDP boreholes [*Robertson and Peck*, 1974]. Set 3 has 191 values of thermal conductivity measured on sandstones, limy and shaly sandstones, and marlstones from Southern Germany

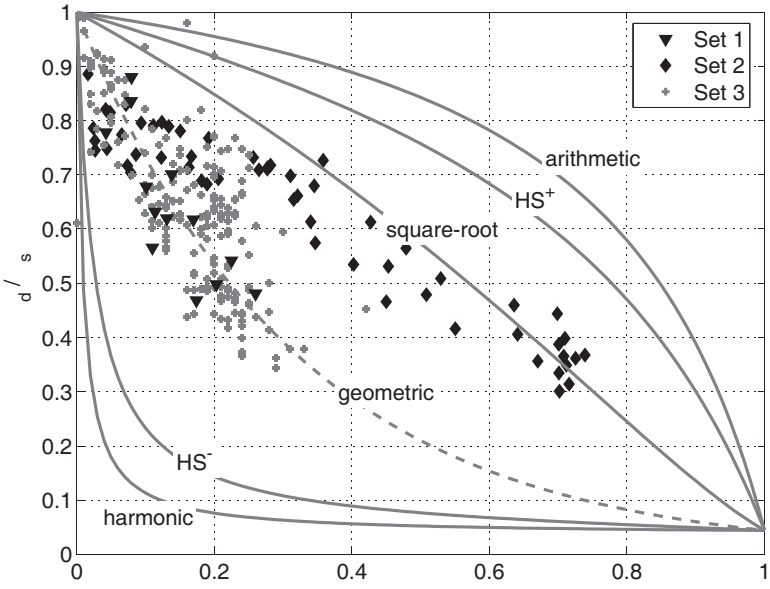

Figure 3.1: Crossplot of the ratio of thermal conductivity values, measured on dry and water saturated samples versus porosity. Actual data is compared to several mixing laws. Every point for data sets 2 and 3 corresponds to a sample value. Every data point for set 1 corresponds to the mean value of a study. See text for references to data sources.

[*Clauser et al.*, 2002; *Rath and Clauser*, 2005]. There is considerable scatter in some of the data sets. However, sets 1 and 3 (sediments) seem to follow approximately the geometric mean, while set 2 (vesicular basalt) shows quite a different trend. Thus, the choice of the appropriate mixing model depends on the lithology and thus the data set.

Several mixing models have been proposed and it is instructive to review the relationships most commonly used in geothermics [*Beardsmore and Cull*, 2001]. Effective thermal conductivity λ of a layered medium with thermal conductivities λ_1 and λ_2 depends on the direction of the temperature gradient. If the heat flux is parallel to layering, the effective conductivity is equal to the arithmetic mean (λ_a) of the layer thermal conductivities, weighted by their volume fractions. Heat transport perpendicular to layering corresponds to the harmonic mean (λ_h) [*Carslaw and Jaeger*, 1959]:

$$\lambda_a = V_1\lambda_1 + V_2\lambda_2, \tag{3.6}$$

$$\frac{1}{\lambda_h} = \frac{V_1}{\lambda_1} + \frac{V_2}{\lambda_2}. \tag{3.7}$$

While these averages are useful to estimate the average thermal conductivity of a vertical rock sequence they are inappropriate for estimating effective sample thermal conductivities. Narrower bounds can be derived by assuming a geometry where the solid consists of spheres dispersed in the pore fluid or were the fluid is confined in spherical inclusions in the rock matrix [*Hashin and Shtrikman*, 1962; *Horai*, 1971]. These configurations yield the lower and upper Hashin-

Shtrikman bounds (HS$^-$, HS$^+$):

$$\lambda_{HS^-} = \lambda_p + \frac{1-\phi}{\frac{1}{\lambda_m-\lambda_p} + \frac{\phi}{3\lambda_p}}, \tag{3.8}$$

$$\lambda_{HS^+} = \lambda_m + \frac{\phi}{\frac{1}{\lambda_p-\lambda_m} + \frac{\phi}{3\lambda_m}}. \tag{3.9}$$

Here ϕ denotes porosity, and the subscripts p and m denote pore and rock matrix properties, respectively. These bounds are of theoretical importance because effective thermal conductivities of rock samples should generally fall in between these bounds. However, in many cases they are too far apart to be of practical use. In this situation an estimate can only be obtained from empirical relationships such as the geometric mean λ_g [*Sass et al.*, 1971], that is often used in geothermal studies:

$$\lambda_g = \lambda_p^{\phi}\lambda_m^{1-\phi}. \tag{3.10}$$

However, other researchers prefer to use the average of the upper and lower HS bounds [*Horai*, 1971], or the square root average λ_s [*Roy et al.*, 1981; *Beardsmore and Cull*, 2001]:

$$\sqrt{\lambda_s} = \phi\sqrt{\lambda_p} + (1-\phi)\sqrt{\lambda_m}. \tag{3.11}$$

The self consistent approach [*Hill*, 1965; *Budiansky*, 1970] is popular for elastic properties but is not widely used in geothermal research. For porosity ranges typical of rocks, it yields results similar to the square-root average. The thermal conductivity λ_b for a two component medium is given by the equation:

$$\frac{\phi}{2/3 + \lambda_p/(3\lambda_b)} + \frac{1-\phi}{2/3 + \lambda_m/(3\lambda_b)} = 1. \tag{3.12}$$

The particular choice of a model becomes important when the contrast in thermal conductivity of the constituents increases. Figure 3.2 illustrates this by showing bounds and estimates for the saturated and the dry case. Thermal conductivity is assumed to be 5 W(m K)$^{-1}$ for the matrix, 0.6 W(m K)$^{-1}$ for water, and 0.026 W(m K)$^{-1}$ for air. In this case, the maximum difference between lower and upper HS bounds is 3.7 W(m K)$^{-1}$ and 1.0 W(m K)$^{-1}$ for dry and saturated samples, respectively. For a two-phase mineral assemblage of crystalline quartz (7.7 W(m K)$^{-1}$) and orthoclase (2.3 W(m K)$^{-1}$) the maximum difference is as low as 0.4 W(m K)$^{-1}$. This shows that the choice of a correct mixing law for a mineral assemblage is somewhat arbitrary while it is essential when considering dry samples. Although a dry sample will rarely occur in nature, these considerations are important when laboratory measurements on dry samples are used to predict in-situ saturated thermal conductivity.

Another important conclusion is, that in the case of a mineral assemblage the geometric mixing law closely follows the lower Hashin-Shtrikman bound, corresponding to a rock model consisting of grains suspended in a fluid. The square root law, in contrast, is very close to the upper Hashin-Shtrikman bound and could be interpreted as a well lithified rock with spherical pores. Thus, as each particular empirical mixing laws corresponds to a particular rock-structure, one single model cannot be adequate for all different rock structures.

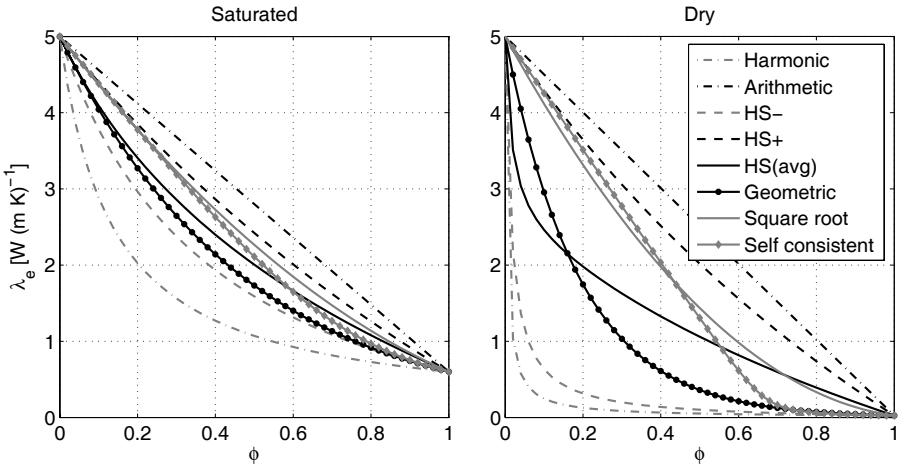

Figure 3.2: Comparison of different mixing laws for the effective thermal conductivity of saturated (*left*) and dry (*right*) rock samples. Matrix, water, and air thermal conductivities are 5 W(m K)$^{-1}$, 0.6 W(m K)$^{-1}$, and 0.026 W(m K)$^{-1}$, respectively. HS$^{\pm}$: Hashin-Shtrikman upper and lower bounds; HS(avg): mean of HS^{+} and HS^{-} bounds.

To overcome this problem, additional parameters can be introduced in order to incorporate rock structure into a mixing law. Several models assume spheroidal pores where α is the aspect ratio of the spheroids [*Korvin*, 1978; *Schulz*, 1981; *Zimmerman*, 1989; *Buntebarth and Schopper*, 1998; *Popov et al.*, 2003b]. The models differ in the way they average over the representative elementary volume (REV). Two of the models are discussed as examples: The first one [*Zimmerman*, 1989] assumes a homogeneous mixture of randomly distributed spheroids. For a rock with oblate spheroidal pores one obtains the effective thermal conductivity λ_e:

$$\frac{\lambda_e}{\lambda_m} = \frac{(1-\phi)(1-r) + r\beta\phi}{(1-\phi)(1-r) + \beta\phi}. \tag{3.13}$$

The parameters r, β, M, and θ are defined by:

$$r = \frac{\lambda_f}{\lambda_m}, \tag{3.14}$$

$$\beta = \frac{1-r}{3}\left(\frac{4}{2+(r-1)M} + \frac{1}{1+(r-1)(1-M)}\right), \tag{3.15}$$

$$M = \frac{2\theta - \sin 2\theta}{2\tan\theta\sin^2\theta}, \tag{3.16}$$

$$\theta = \arccos\alpha. \tag{3.17}$$

Here, α is the aspect ratio of the spheroidal inclusions. In an application of this model aspect ratios as low as 0.1 were found for basalts [*Horai*, 1991], much less than the actual one of the pores. This was interpreted to represent the aspect ratio of the grain contact area rather than that of the pores.

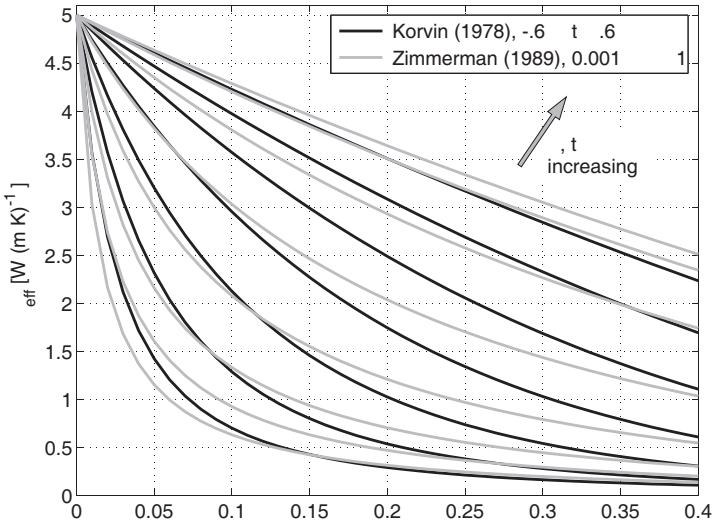

Figure 3.3: Comparison of effective thermal conductivities for the two models with an additional structural parameter that are discussed in the text. A dry rock is considered with a thermal conductivity of 5 W(m K)$^{-1}$ for the matrix and 0.026 W(m K)$^{-1}$ for air. t is varied in steps of 0.2 from -0.6 to 0.6; $\ln \alpha$ is varied from -3 to 1 in 8 steps of width 0.9868.

A different approach was taken by *Korvin* [1978, 1982]. They introduced a parameter that has no direct physical meaning. A mean equation was derived as a special case of a Kolmogorov-Nagumo mean [*Rényi*, 1976], satisfying widely-used empirical means. Their analysis yielded the "generalised t-th order mean". In terms of the thermal conductivity of a two-phase system, this mean can be written as

$$\lambda_t(\phi, \lambda_p, \lambda_m, t) = \left[\phi\lambda_p^t + (1-\phi)\lambda_m^t\right]^{1/t}. \tag{3.18}$$

For values of $t = -1, 0, 1$ λ_t is equivalent to the harmonic mean, geometric mean, and arithmetic mean, respectively[3]. However, the upper and lower Hashin-Shtrikman bounds cannot be reproduced exactly. This is in contrast to the model of *Zimmerman* [1989] where the Hashin-Shtrikman bounds are special cases of the relationship but empirical relations cannot be reproduced exactly.

Figure 3.3 compares both models for a range of their structural parameters. When the uncertainty of measurement data for thermal conductivity and porosity is taken into account (e.g. data scatter in figure 3.1) it is clear that both relationships should describe equally well a particular data set with a limited range of porosity. In the following analysis the model of *Zimmerman* [1989] is used.

[3] The case $t = 0$ is solved by using the rule of de l'Hospital, see Appendix A.1

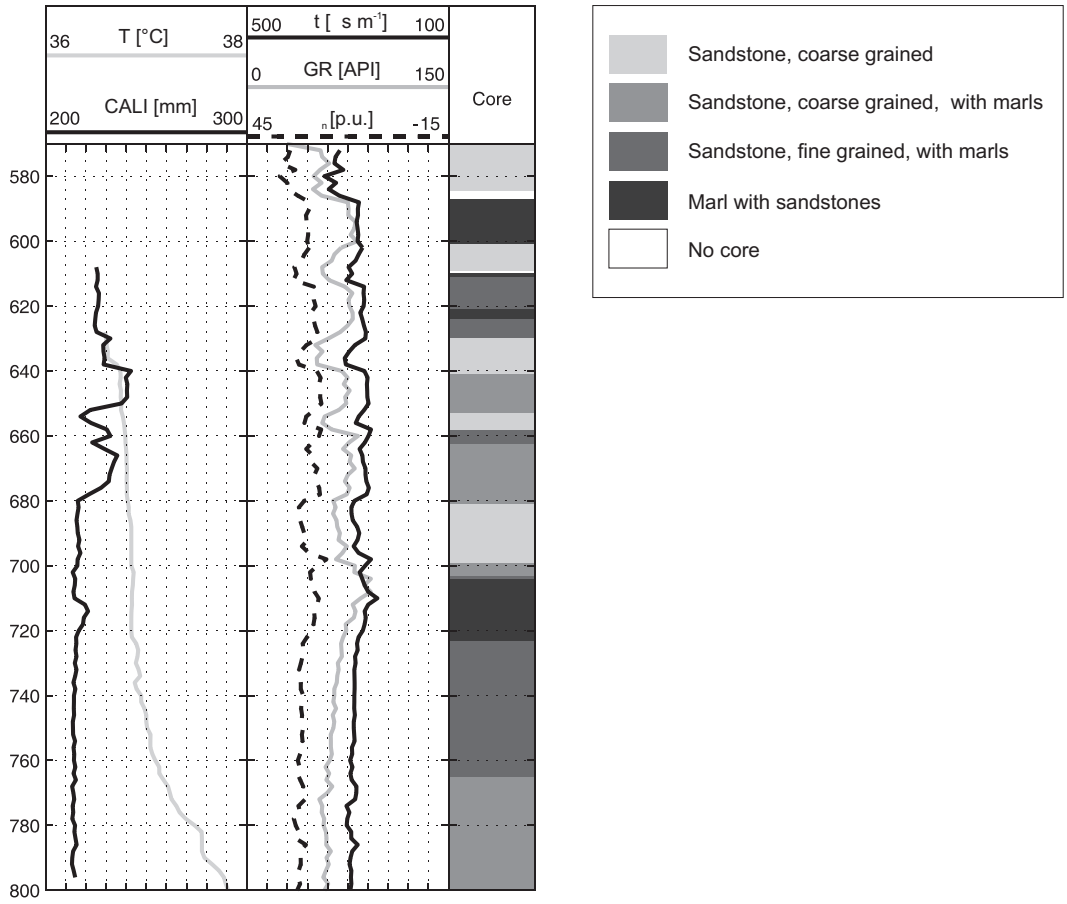

Figure 3.4: Composite log showing temperature (T), caliper ($CALI$), acoustic slowness (Δt), neutron porosity (ϕ_n), γ-ray (GR), and core lithology (core). Porosity unit (p.u.) refers to limestone porosity of the ϕ_n-log.

3.3 Analysis of laboratory data

The different methods for inferring thermal conductivity will be assessed on a data set from a borehole in the Molasse region in Southern Germany (Appendix C, figure C.1, well A). Following the description of the data set and the measurements, the laboratory data is analysed in order to derive cross-correlations of rock properties that are suitable for direct empirical determination of thermal conductivity. Following this analysis, necessary corrections to transform values to in-situ conditions are discussed.

3.3.1 Description of methods and samples

The data set for laboratory analysis is obtained from a borehole drilled for hot water into the Upper Marine Molasse formation. This formation consists of shaly sandstones and marls (Figure 3.4). The borehole was cored between 570 m and 810 m depth with nearly total recovery. The sequence consists of a succession of shaly sandstones and marl beds. Average core porosity is

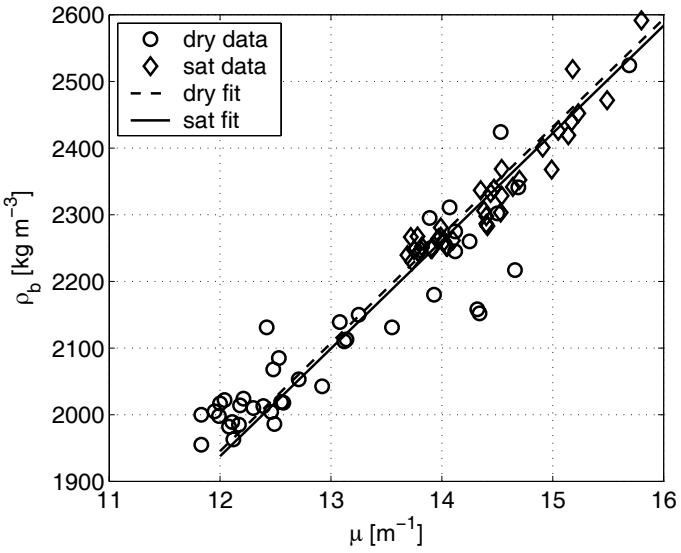

Figure 3.5: Calibration of bulk density measurements ρ_b. The absorption coefficient μ measured on dry and saturated samples is converted into bulk density using equation 3.20.

about 20 %, ranging from 10 % to 30 %. Split cores were available for measurements in sections of 1 m length. In general, every fifth section was analysed, but in some depth intervals all cores were studied. The cores had been broken into several pieces during coring and splitting. Two to five samples from each core section were selected for further analysis. The samples were dried at 60 °C to prevent cracking or alteration of clay minerals. After drying, thermal conductivity, sonic velocity, and bulk density were measured on the samples. Then the samples were saturated under vacuum and the same measurements were repeated on the saturated samples. A number of samples was damaged or destroyed during saturation due to occasionally poor consolidation. This results in a lower number of saturated than dry measurements.

Thermal conductivity was measured using the optical scanning technique which yields a continuous profile of thermal conductivity along the core axis ($\lambda_\parallel$) of the sample [*Popov*, 1997; *Popov et al.*, 1999; *Surma and Geraud*, 2003]. Thermal conductivity was also measured perpendicular to the core axis ($\lambda_\perp$) to obtain the anisotropy ratio Γ_λ:

$$\Gamma_\lambda = \frac{\lambda_\parallel}{\lambda_\perp}. \tag{3.19}$$

Values of Γ_λ were generally less than 1.03 to 1.04, so that the rock can be considered isotropic. For each sample the thermal conductivity was computed as the average value of the scanning line. Bulk density and sonic velocity were measured with a multi-sensor core-logger (*Weber et al.* [1997]). The measurement is performed perpendicular to the core axis. Again, additional measurements parallel to the core axis confirmed that anisotropy can be ignored.

Bulk density is measured by γ-ray absorption which is mainly due to Compton scattering for the considered energy range [*Ellis*, 1987]. It is calibrated routinely using an aluminium standard. Since electron density is measured rather than real density, better results are obtained when using a calibration standard with a similar electron density [*Ellis*, 1987]. Therefore, bulk density

and porosity were measured independently on a number of samples using either Archimedes' principle or gas- and powder-pycnometers. This bulk density is then plotted versus the absorption coefficient μ measured with the core-logger for dry and saturated samples (figure 3.5). This yields a linear relationship which can be used for the calibration of the dry and saturated measurements $\rho_{b,d}$ and $\rho_{b,s}$, respectively:

$$\begin{aligned} \rho_{b,d} &= 162.1\mu_d, \\ \rho_{b,s} &= 161.5\mu_s. \end{aligned} \tag{3.20}$$

The slope is slightly lower for saturated measurements. Considering the data scatter of the measurements, a single calibration factor (161.8) was used, computed as the average of the two values in equation 3.20.

3.3.2 Corrections to in-situ conditions

The measurements were performed in the laboratory at ambient conditions. As the samples are taken from depths of less than 800 m, it was first assumed that the correction to in-situ conditions would be small. However, large discrepancies between sonic velocity measured on cores and from wireline tools in the borehole indicated that this assumption may not be valid (figure 3.6, right). Within the scope of this study, it was impossible to perform a complete study of the in-situ physical properties of all samples because (1) the increased experimental complexity and time required prohibited measuring all samples; (2) when put under stress, the poorly consolidated samples often failed before any measurement could be performed. Thus, only a few selected samples were analysed to study the magnitude of the effects. At depth, the rock sample is exposed to elevated pressure and temperature. The temperature dependence of thermal conductivity and the pressure dependence of sonic velocity are discussed in the following.

The temperature dependence of sonic velocity should be small in the range appropriate for these samples and mostly due to the influence on the pore fluid, in our case water. It is, however, well known that pressure has a profound influence on the elastic properties of rock [e.g. *Mayr*, 2002; *Zimmerman et al.*, 1986]. An empirical relationship with linear and exponential terms can be used to correct this effect. In order to obtain the appropriate correction, sonic velocity was measured on three samples[4] as described in *Mayr* [2002]. In this case, uniaxial pressure was applied by a hydraulic press, creating a primary stress field in the axial direction of the sample. Unconfined, the sample would react by a compression in axial direction and an expansion in radial direction. The geometry of the sample holder and friction on the buffers connecting the ultrasonic transducers to the sample prevent this expansion, inducing a secondary stress field in radial direction comparable to in-situ conditions[5].

Two of the samples could only be tested up to 3.4 MPa. Two exponential equations are fitted to the remaining data set (Figure 3.6 and Appendix B, table B.2), both with an exponential term and one with an additional linear term. The following coefficients were obtained, with pressure

[4]Courtesy of Dr. S. Mayr, TU Berlin.

[5]Personal communication, Dr. S. Mayr, TU Berlin, 2003.

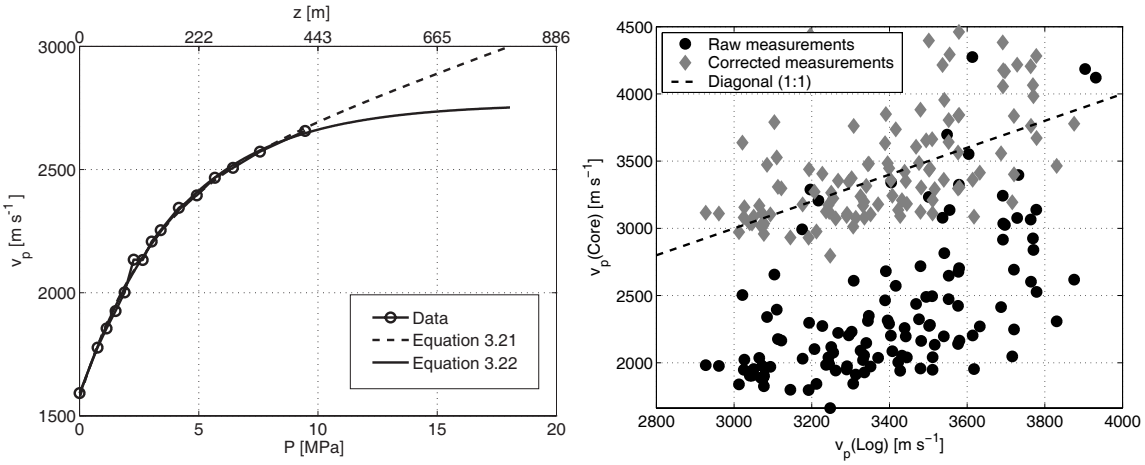

Figure 3.6: Variation of sonic velocity v_p with confining pressure P. *Left*: Laboratory data, linear-exponential fit, and exponential fit. The two fits differ only in the extrapolated range. Pressure was converted to depth using a constant density of 2300 kg m^{-3}. *Right*: Data before and after pressure correction based on equation 3.22.

P in MPa and velocity v in m s^{-1}:

$$v(P) = 2360 - 787\mathrm{e}^{-0.356P} + 35.7P, \tag{3.21}$$

$$v(P) = 2760 - 1180\mathrm{e}^{-0.243P}. \tag{3.22}$$

The RMS-errors are 19 m s^{-1} (Equation 3.21) and 18 m s^{-1} (Equation 3.22). Pressure was converted to depth assuming a constant density of 2300 kg m^{-3}, corresponding to a pressure gradient of 22.6 MPa km^{-1}. Both equations fit the pressure-velocity data equally well and differ only in the extrapolated range (450 m to 820 m). To decide on the best fit, laboratory data corrected with both equations is compared to logging data. Equation 3.22 yields a better match of corrected laboratory data and the logging data. Equation 3.21 slightly over-corrects the laboratory data. This is caused by limiting the measurements to a maximum pressure of 10 MPa. In this pressure range, the exponential term is more significant, and the linear term is not well defined. Therefore, equation 3.22 was used to correct the data (Figure 3.6, right).

However, even after correction large scatter remains. This may be caused by assessing the pressure dependence only on one type of rock although more rock types are sampled by the borehole. A more detailed analysis would need to account for the variable composition of the samples. The corrected data were used for the correlation analysis (section 3.3.3) but not for a direct correlation with properties measured in the borehole.

The temperature dependence of thermal conductivity was studied on 22 samples from the Molasse Basin, with one of the samples from the borehole considered here [*Clauser et al.*, 2002]. The samples were measured in the temperature range from 5 °C to 150 °C (Figure 3.7 and Appendix B, table B.1). A general equation that describes the temperature dependence of λ was derived by *Sass et al.* [1992]:

$$\lambda(T) = \frac{\lambda_0}{a + T(b - c/\lambda_0)}. \tag{3.23}$$

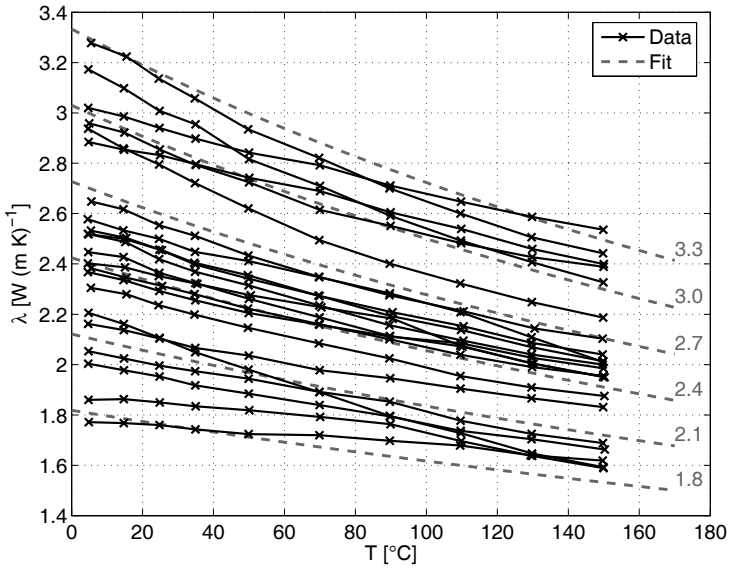

Figure 3.7: Variation of thermal conductivity λ with temperature T. Thermal conductivity was measured on 22 samples (black lines) and fitted with equation 3.23 (grey lines). Numbers denote the value of λ_0 (equation 3.23).

Table 3.2: Coefficients describing the temperature dependence of thermal conductivity in equations 3.23 and 3.24. Also given is the equation *Sass et al.* [1992] used to compute λ_0.

Reference	Rock type	a	b	c	A	B	C
		[ ]	[K^{-1}]	[W m^{-1} K^{-2}]	[ ]	[ ]	[W $(m K)^{-1}$]
Vosteen and Schellschmidt [2003]	Sedimentary	0.99	0.0034	0.0039	0.54	1.16	0.39
Vosteen and Schellschmidt [2003]	Crystalline	0.99	0.0030	0.0042	0.53	1.13	0.42
Sass et al. [1992]	Crystalline	1.007	0.0036	0.0072	(λ_0 = 1.0995λ_{25} - 0.185)		

a, b, and c are coefficients to be determined and λ_0 is the thermal conductivity at 0°C. It can be derived from the thermal conductivity at room temperature λ_{25} using the equation

$$\lambda_0 = A\lambda_{25} + \frac{1}{2}\left(B\lambda_{25}^2 - C\lambda_{25}\right)^{\frac{1}{2}}. \tag{3.24}$$

Table 3.2 summarises the coefficients of the Molasse data set [*Vosteen and Schellschmidt*, 2003] together with those computed by *Sass et al.* [1992]. The variation of λ with temperature is stronger than that derived by Sass for crystalline rocks. For the borehole considered here the maximum depth was about 800 m. An aquifer test at this depth yielded a fluid temperature of 36 °C (figure 3.4). Using a range of 2.5 W$(\mathrm{m\,K})^{-1}$ to 3.5 W$(\mathrm{m\,K})^{-1}$ for the saturated thermal conductivity the necessary correction amounts to 5 % to 7 %.

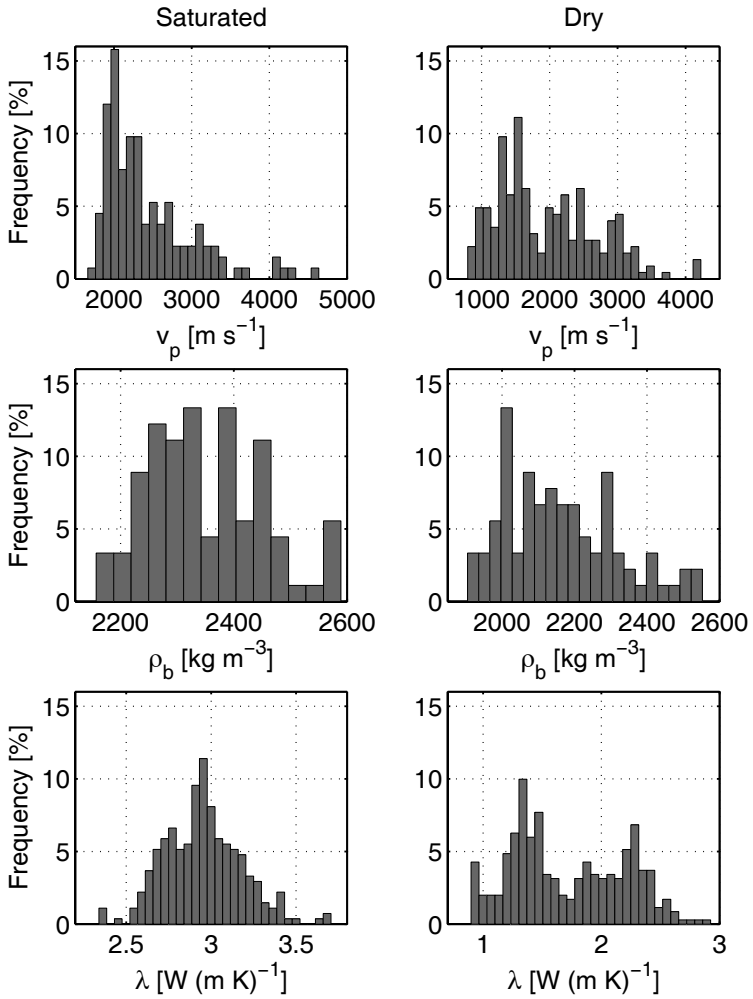

Figure 3.8: Histograms of sonic velocity v_p (*top*), bulk density ρ_b (*center*), and thermal conductivity λ (*bottom*) measured in the laboratory on saturated (*left*) and dry (*right*) on core samples. The bimodal distribution reflects two different lithologies in the borehole (see also figure 3.4).

3.3.3 Thermal conductivity predicted from laboratory data

Figure 3.8 shows a summary of the measurements processed as described in the previous section. Dry properties show a broader distribution of values, in the case of thermal conductivity it is even bimodal. This results from the larger ratio of fluid to matrix properties for the rock/air-system than for the rock/water-system. Hence, also the range of the effective values is larger for dry properties.

Next, it is attempted to predict thermal conductivity from other petrophysical properties which can be measured in-situ. For this purpose linear correlations between thermal conductivity and other properties in dry and saturated conditions are analysed. Figure 3.9 shows cross-plots of these data. Porosity was computed from dry and saturated bulk density but not from the sonic

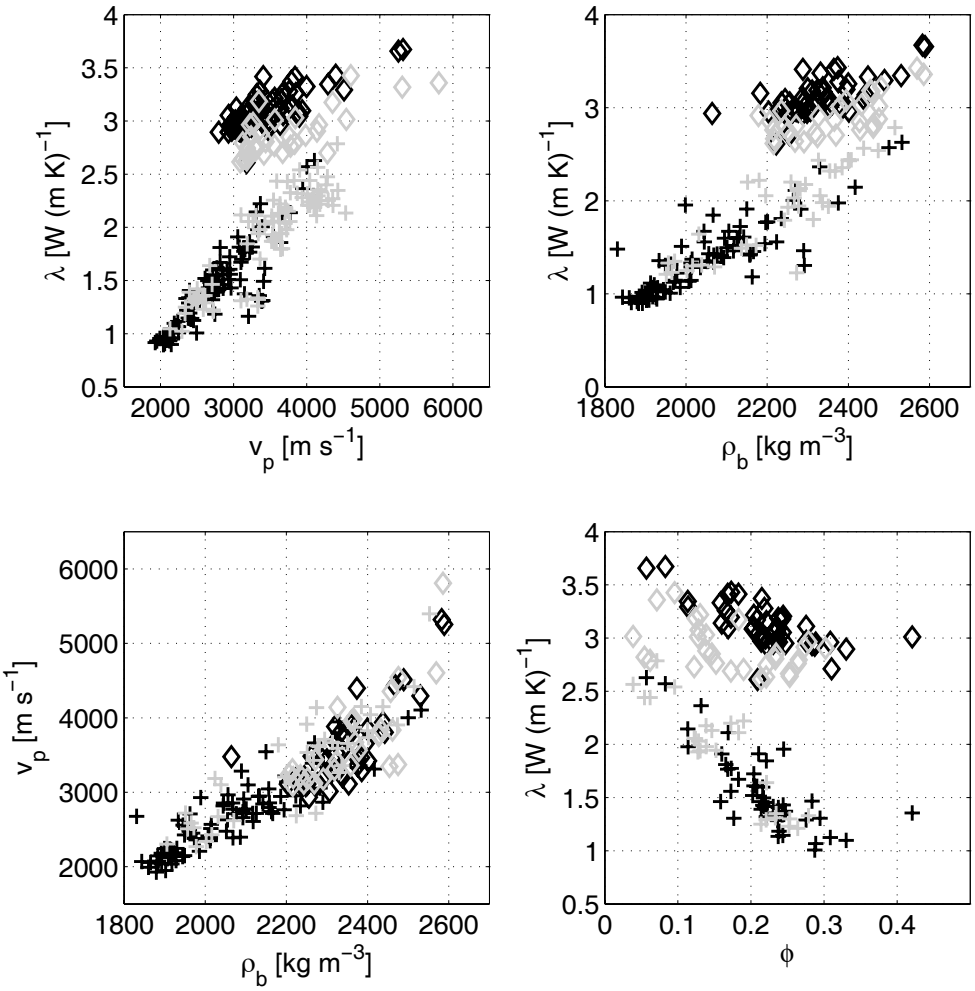

Figure 3.9: Cross-plot of properties measured in the laboratory: Thermal conductivity λ versus sonic velocity v_p (*top left*), bulk density ρ_b (*top right*), and porosity ϕ (*bottom right*). ϕ is derived from dry and saturated γ-density measurements. Sonic velocity v_p versus bulk density ρ_b is plotted in the lower left. Black and grey symbols correspond to sandy and carbonaceous samples. Dry measurements are shown as crosses (+), saturated ones as diamonds ($\diamondsuit$).

measurements. The reason is that velocity-porosity models work best when velocity is measured under confining pressure such that the rock is at its terminal velocity [*Wyllie et al.*, 1956; *Mavko et al.*, 1998]. Samples are grouped according to their lithology: The first group contains shaly sandstone samples (‘‘sandy samples’’), the second group marlstones (“carbonaceous samples’’). This division is somewhat preliminary as it is based on geological core descriptions and not on an analysis of the mineral assemblages.

Regression analyses of thermal conductivity versus sonic velocity, bulk density, and porosity were performed and linear equations of the form

$$y = a_1 x + a_0 \tag{3.25}$$

Table 3.3: Results of single regression analysis for thermal conductivity λ of core samples; a) for dry samples and b) for water saturated samples. The regressions are based on sonic velocity v_p, bulk density ρ_b, and porosity ϕ. For each regression the fit parameters a_1 and a_0 (Equation 3.25) together with their standard deviations, correlation coefficient r, and the RMS-error of the fit are shown. Fits were computed both for all samples and grouped by lithology. The physical unit of a_1 is [W(m K)$^{-1}$/km s^{-1}] for v_p, [W(m K)$^{-1}$/g cm^{-3}] for ρ_b, and [W(m K)$^{-1}$] for ϕ.

a) dry samples

Property	Lithology	a_1	a_0 [W (m K)]$^{-1}$	r	RMS
v_p	all samples	0.696 ± 0.018	-0.485 ± 0.050	0.921	0.18
ρ_b	all samples	2.715 ± 0.086	-4.167 ± 0.183	0.886	0.23
ϕ	all samples	-6.289 ± 0.570	2.926 ± 0.103	-0.849	0.24
v_p	sandy	0.744 ± 0.028	-0.601 ± 0.068	0.898	0.17
v_p	carbonaceous	0.68 ± 0.031	-0.457 ± 0.108	0.893	0.20
ρ_b	sandy	2.5 ± 0.123	-3.74 ± 0.250	0.844	0.22
ρ_b	carbonaceous	2.942 ± 0.179	-4.645 ± 0.412	0.851	0.24
ϕ	sandy	-5.783 ± 0.898	2.818 ± 0.178	-0.772	0.25
ϕ	carbonaceous	-6.49 ± 0.489	2.939 ± 0.097	-0.897	0.20

b) saturated samples

Property	Lithology	a_1	a_0 [W (m K)]$^{-1}$	r	RMS
v_p	all samples	0.378 ± 0.042	1.696 ± 0.145	0.551	0.20
ρ_b	all samples	2.214 ± 0.192	-2.151 ± 0.452	0.537	0.23
ϕ	all samples	-3.304 ± 0.394	3.701 ± 0.083	-0.363	0.27
v_p	sandy	0.372 ± 0.035	1.809 ± 0.118	0.784	0.12
v_p	carbonaceous	0.363 ± 0.056	1.537 ± 0.183	0.449	0.16
ρ_b	sandy	2.074 ± 0.263	-1.713 ± 0.618	0.687	0.16
ρ_b	carbonaceous	1.696 ± 0.230	-1.112 ± 0.540	0.548	0.16
ϕ	sandy	-3.229 ± 0.541	3.828 ± 0.106	-0.696	0.16
ϕ	carbonaceous	-2.352 ± 0.451	3.289 ± 0.101	-0.331	0.20

were fitted to the data. This regression analysis uses a total-least-squares solution to account for measurement errors in both the dependent and independent variables [*Huffel and Vandewalle*, 1991]. The Jackknife-method yields the variances of the parameter estimates [*Shao and Tu*, 1995]. Together with the correlation coefficient r and RMS-error [*Blobel and Lohrmann*, 1998] they are used to assess the quality of the fit.

Table 3.3 summarises the results. If the RMS-error is interpreted as the predictive error of the computed relationships it can be deduced that it is possible to calculate thermal conductivity from density and sonic velocity with an average accuracy of about 0.1 W(m K)$^{-1}$ to 0.2 W(m K)$^{-1}$,

Table 3.4: Results of the multiple regression of thermal conductivity λ versus sonic velocity v_p, bulk density ρ_b, and porosity ϕ (equation 3.26). Each regression coefficient a_i is shown with its standard deviation. Also shown are explained variance R^2 and RMS-error of the fit. Fits were computed both for all samples and grouped by lithology.

Lithology	Saturation	a_3	a_2	a_1	a_0	R^2	RMS
		[W (m K)$^{-1}$]	[10^3 W m^2 K^{-1} kg^{-1}]	[10^{-3} J m^{-2} K^{-1}]	[W (m K)$^{-1}$]		
sandy	dry	-0.53 ± 0.35	0.616 ± 0.096	0.5199 ± 0.0045	-1.14 ± 0.47	0.85	0.15
sandy	saturated	0.04 ± 0.14	0.504 ± 0.053	0.2394 ± 0.0024	1.07 ± 0.28	0.69	0.12
carbonaceous	dry	-2.82 ± 0.74	0.209 ± 0.231	0.3711 ± 0.0062	0.64 ± 1.06	0.92	0.13
carbonaceous	saturated	0.67 ± 0.22	1.056 ± 0.172	0.1001 ± 0.0046	-0.11 ± 0.83	0.41	0.13
all samples	dry	-1.19 ± 0.20	0.557 ± 0.053	0.4750 ± 0.0022	-0.74 ± 0.26	0.90	0.14
all samples	saturated	1.11 ± 0.13	0.913 ± 0.076	0.2428 ± 0.0020	-0.23 ± 0.39	0.50	0.17

given an appropriate data set for calibration. Correlation coefficients are largest for dry properties. This is due to the larger contrast in rock and pore volume properties for dry samples. Thus, porosity variations cause larger variations in the effective properties of the two-component system and therefore stronger correlations for dry samples. Correlation coefficients are particularly low for thermal conductivity and porosity due to the non-linear relationship between these properties. Grouping samples according to their lithology has a larger effect on the quality of the fit for saturated than for dry samples. In figure 3.9, in the cross-plots of thermal conductivity versus sonic velocity and bulk density, the two lithology groups yield the same general trend for dry samples but different trends for saturated samples. This again is an effect of the strong influence of porosity for dry samples which masks variations due to lithology. From our analysis it thus appears that dry measurements are most sensitive to porosity changes whereas saturated ones reflect both variations in lithology as well as porosity.

The question arises if a correlation using more than one petrophysical property improves the prediction of thermal conductivity. Table 3.4 shows the results of a multiple linear regression for thermal conductivity. The equation has the form:

$$\lambda = a_0 + a_1 v_p + a_2 \rho + a_3 \phi. \tag{3.26}$$

There is only slight improvement over the simple regressions. In practise, this improvement may be offset by the additional effort for performing the measurements. If the samples are considered to be composed of the three components sand, shale, and carbonate, the quality of the predicted thermal conductivity is directly related to the ability to differentiate the end members based on the measured properties. However, quartz and calcite differ in density and velocity by only 3 % and 13 %, respectively. Shales have a large variability in their physical properties, but usually they differ considerably from quartz and calcite [*Ellis*, 1987; *Crain*, 1986]. Therefore, any of the measurements will be more sensitive to variations in shale content and porosity than to changes in carbonate and sand content. Thus, a combination of sonic velocity and bulk density does not provide significantly more information than each of the measurements alone. This is demonstrated in a cross-plot of these two properties (Figure 3.9, lower left panel): Sandy and carbonaceous samples essentially plot on top of each other. The contrast in thermal conductivity

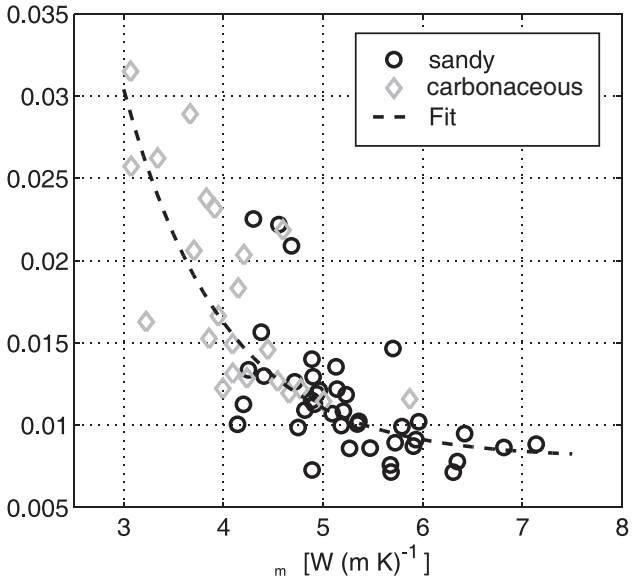

Figure 3.10: Variation of aspect ratio α with matrix thermal conductivity λ_m. Both properties are computed from equations 3.13 and 3.14. Dry and saturated thermal conductivity as well as porosity derived from bulk density were used as input to the model. The dashed line shows an exponential fit (equation 3.27) to the data with an R^2 value of 0.59.

between quartz and calcite is about 60 %, sufficiently large to separate them in a cross-plot (Figure 3.9, top left and right). This offers opportunities for characterising lithology, as conductivity can be determined rapidly and continuously along a core.

According to the discussion on mixing laws, it appears that it may be necessary to take the pore structure into account for the laboratory data. The model proposed in *Zimmerman* [1989] was therefore applied to the laboratory data set in order to determine the aspect ratio α. The model described by equations 3.13 to 3.17 consists of five parameters: effective, matrix, and pore fluid thermal conductivity, porosity, and aspect ratio. The measurements of saturated and dry thermal conductivity yield two equations of this type which differ only in the effective thermal conductivity λ and the pore fluid thermal conductivity λ_f. This yields seven parameters in total. Using the two thermal conductivity measurements, known values of water and air thermal conductivity, and an independent porosity measurement, two equations with two unknowns are obtained: Matrix thermal conductivity and pore aspect ratio.

This non-linear system of equations was solved by an iterative algorithm[6]. Figure 3.10 shows a cross-plot of the computed values of matrix thermal conductivity λ_m and aspect ratio α together with a least-squares fit

$$\alpha = 0.008 + 0.45 \cdot \mathrm{e}^{-\lambda_m}. \tag{3.27}$$

The R^2 value of the fit is 0.59. The median values of α are 0.011 and 0.016 for sandy and carbonaceous samples, respectively. This is about one magnitude less than the values reported

[6]The `LSQCURVEFIT` function of the Matlab™ package was used. It is based on the interior-reflective Newton method described in *Coleman and Li* [1996].

by *Horai* [1991]. However, those values were measured on igneous rocks and crack aspect ratios based on sonic or mechanical measurements generally range from 10^{-2} to 10^{-3} [*Cheng and Toksöz*, 1979; *Zimmerman*, 1984]. The median matrix thermal conductivity is 5.14 $\mathrm{W(m\,K)^{-1}}$ for sandy samples and 4.09 $\mathrm{W(m\,K)^{-1}}$ for carbonaceous samples. From figures 3.2 and 3.3 it is clear that this low aspect ratio puts the dependence of thermal conductivity on porosity close to the lower Hashin-Shtrikhman bound. Given the large separation between mixing laws for dry samples this shows that an analysis of laboratory data with dry samples should not be carried out without considering the structural parameters. For saturated samples, the geometric mixing law seems to be a valid approximation.

3.4 Analysis of wireline data

The following section discusses the derivation of thermal conductivity λ from wireline data in the same borehole where the core samples are available. It starts with a discussion of the data and the inversion method used for computing λ. This method is applied to obtain thermal conductivity profiles for two models of varying complexity. The resulting profiles are analysed and compared to the laboratory data to test their predictive power.

3.4.1 Description of methods and data

Wireline logs of natural γ-radiation (GR), neutron porosity (ϕ_n), and bulk density (ρ_b) were available for analysis in the depth range 570 m to 800 m. In the depth range from 600 m to 800 m caliper ($CALI$) and temperature (T) were logged during a pumping test (figure 3.4). The temperature log is strongly disturbed by water flowing from the sandstone formation with temperatures from 35 °C to 37 °C. Unfortunately, the disturbance makes it impossible to interpret temperatures quantitatively with regard to the conductive regime. The hole was drilled with 8.5 “ diameter and the caliper reads generally below 9 “. The larger diameter sections (630 m to 680 m) are consistent with lithological changes. The core lithology showed no signs of hydrocarbons and the drilled sequence is not known as a hydrocarbon reservoir. Thus, log data quality can be regarded as sufficient for a quantitative interpretation.

Several editing steps were required prior to the quantitative analysis of logging data [see *Ellis*, 1987; *Serra*, 1984; *Jun*, 2002]: Logging curves from different tool runs were corrected to common depth points, bad data eliminated, and environmental corrections applied. Core depths are shifted to match logging depths. Core data are smoothed before they are compared to log curves since these have a lower depth resolution. For this purpose an inverse distance algorithm was used that employs an Gaussian weighting function:

$$w_k = \sum_{i=1}^{N} \mathrm{e}^{-\left(\frac{z_k - z_i}{r_w}\right)^2}, \tag{3.28}$$

$$u_k = \frac{1}{w_k} \sum_{i=1}^{N} u_i \mathrm{e}^{-\left(\frac{z_k - z_i}{r_w}\right)^2}. \tag{3.29}$$

Here u_k are data values, z_i is the depth of the ith value, N is the number of samples, and w_k is the normalisation constant. The weighting distance r_w was 0.5 m.

Table 3.5: Physical properties for various common minerals. ρ: Density; Δt: Acoustic slowness; U: Volumetric photoelectric cross section; ϕ_n: Neutron porosity; GR: Natural γ-radiation; λ: Thermal conductivity. Thermal conductivity data after *Čermák and Rybach* [1982]; *Horai* [1971]; *Clauser and Huenges* [1995]; *Clauser* [2006], all other data after *Hearst et al.* [2000]; *Ellis* [1987]; *Serra* [1984].

Mineral	ρ	Δt	U	ϕ_n	GR	λ	λ range	
	[kg m^{-3}]	[µs m^{-1}]	[barn cm^{-3}]	[p.u.]	[API]	[W (m K)$^{-1}$]	[W (m K)$^{-1}$]	
Albite	2620	161	5.60	-1.0	8	2.17	2.0	2.34
Anhydrite	2960	164	14.95	-2.0	5	5.35	4.8	5.90
Ankerite	3050							
Biotite	3040	197	21.60	13.4	127	2.02	1.7	2.34
Calcite	2710	157	14.10	0.0	11	3.59	3.2	3.63
Dolomite	2870	143	91.00	1.8	8	4.90	4.3	5.50
Halite	2165	220	9.70	-3.0	0	5.55	4.5	6.57
Gypsum	2320	171	9.46	54.0	0	2.45	1.3	3.60
Glauconite	2650	295	16.50	41.0	150	1.63		
Illite	2770	295	9.90	35.2	150			
Kaolinite	2640	262	5.10	50.7	150			
Muscovite	2850	174	11.50	24.0	130	2.28	2.2	2.35
Orthoclase	2550	197	8.70	-1.0	170	2.31	2.10	2.52
Quartz	2650	182	5.00	-6.0	30	7.69	6.5	10.17

In general, the response R^j of a wireline tool j is determined by the volume fractions V_i of the rock components i and their theoretical log response T_i^j (table 3.5). The function relating these can be complex but often a simple linear relationship can be used:

$$R^j = \sum_i V_i T_i^j, \tag{3.30}$$

with the constraint that $\sum_i V_i = 1$ [*Doveton and Cable*, 1979; *Hoppie*, 1996]. Equation 3.30 corresponds to the weighted arithmetic average (equation 3.6). It is valid when the contributions of the constituents can be added, such as for bulk density or γ-radiation. For acoustic slowness equation 3.30 is Wyllie´s classical travel-time average [*Wyllie et al.*, 1956].

If the number of constituents equals the number of tool responses equation 3.30 has exactly one solution. If the number of equations is larger than the number of components, the system is over-determined and equation 3.30 can be solved in a least-squares sense. Thus, lithological composition can be computed from a sufficient number of logs. An effective thermal conductivity can be computed based on this composition and the known values of component thermal

Table 3.6: Summary of component petrophysical properties used in the log data analysis. Slowness Δt, natural γ-radiation GR, and neutron porosity ϕ_n are used in model 1. For model 2 ϕ_n is not used and Δt coefficients are determined from equation 3.31. The log-response of air is only needed for computing thermal conductivity of the dry rock.

		Δt [µs m^{-1}]	GR [API]	ϕ_n [p.u.]	λ [W(m K)$^{-1}$]
Model 1					
Sand	(quartz)	182	30	-6	7.69
Shale	(glauconite)	295	150	41	2.20
Carbonate	(calcite)	157	11	0	3.59
Model 2					
Sand	(quartz)	N/A	30	N/A	6.39
Shale	(glauconite)	N/A	150	N/A	1.96
Pore space properties					
Saturated rock	(water)	690	0	1	0.598
Dry rock	(air)	N/A	N/A	N/A	0.026

conductivities. The geometric average law is used to compute the effective thermal conductivity of the mineral mixture. This value will be used as the matrix thermal conductivity. The effective conductivity of dry and water-saturated rocks is then calculated from equation 3.13 using a median aspect ratio of $\alpha = 0.012$. This value was derived in the analysis of the laboratory data. No temperature correction is necessary at this stage because the results are compared to the laboratory data measured at ambient conditions.

3.4.2 Thermal conductivity predicted from wireline data

As discussed previously for laboratory data, different models with varying simplicity are explored to evaluate how well thermal conductivity can be described by logging data under different circumstances. Two models are of particular interest: (1) Model 1 consists of a mixture of sand, shale, and carbonate and uses the information of all logs available for the borehole; (2) Model 2 consists only of the two components sand and shale, ignores the carbonate fraction, and uses only wireline logs of slowness (Δt) and natural γ-radiation (GR). This model may be applied to older wells for which only these two logs are available. While these wells have not been logged with modern tools they comprise a large fraction of the available data set in the Molasse Basin.

The first model uses logs of γ-density (ρ_b), natural γ-radiation (GR), and slowness (Δt) as input. A commercial software package[7] was employed, specialised in deriving rock composition from wireline logs. The three components sand, shale, and carbonate were parametrised

[7]The analysis was done using ELANPlus™. This software is part of the Geoframe™ package, see *Anonymous* [1999].

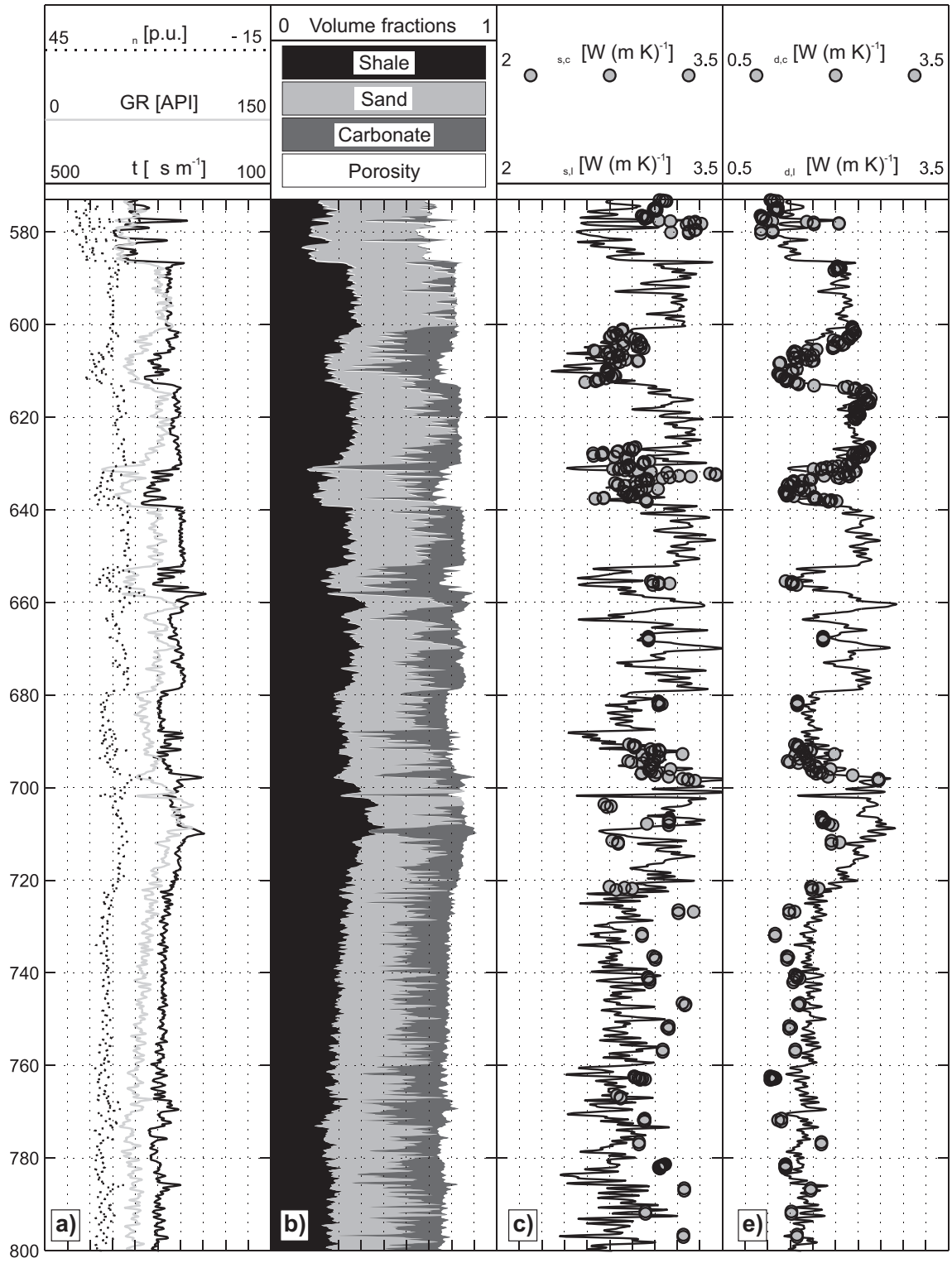

Figure 3.11: Model 1 (Sand-Shale-Carbonate) for the studied borehole. *a)* Input logs. *b)* Composition. *c)* Saturated thermal conductivity. *d)* Dry thermal conductivity. ϕ_n: Neutron porosity; GR: Natural γ-radiation; Δt: Acoustic slowness; λ: Thermal conductivity. Index l: From log data; Index c: Core data; Index s: Saturated rock; Index d: Dry rock.

Table 3.7: Coefficients a_0, a_1, a_2 in equation 3.31, given for various pressures P, after *Han et al.* [1986].

P [MPa]	a_0 [km s^{-1}]	a_1 [km s^{-1}]	a_2 [km s^{-1}]
400	5.59	6.93	2.18
300	5.55	9.96	2.18
200	5.49	6.94	2.17
100	5.39	7.08	2.13
50	5.26	7.08	2.02

in the inversion using the response values for the minerals quartz, glauconite, and calcite. The choice of the shale mineral glauconite, an iron-rich variety of illite, is based on the geological description of the cores and general information about the geology of the Upper Freshwater Molasse [*Geyer and Gwinner*, 1991]. It might not be the only shale mineral present, but the values for illite, another abundant shale mineral, are very similar to the ones used. Values for the logging responses and mineral thermal conductivities are summarised in Table 3.6. Thermal conductivity is 7.69 W(m K)$^{-1}$ for quartz and 3.59 W(m K)$^{-1}$ for calcite [*Clauser and Huenges*, 1995]. The choice for the shale fraction is more difficult. Glauconite was measured with a value of 1.6 W(m K)$^{-1}$ [*Horai*, 1971]. However, fitting this data set requires a higher value of 2.2 W(m K)$^{-1}$. This discrepancy can be explained easily by the variability of properties for shale minerals, but could also indicate that small amounts of other minerals are present which are not accounted for. Generally, there is a good agreement between computed and measured thermal conductivity (Figure 3.11). The RMS-error of the reconstruction is 0.27 W(m K)$^{-1}$ for saturated thermal conductivity and 0.28 W(m K)$^{-1}$ for dry thermal conductivity. The agreement between log and core values in figure 3.11 seems to be better for dry properties than for saturated conditions. However, the almost equal RMS-values suggest a similar prediction error for dry and saturated conditions. The reason is that the range of dry values is much larger because the large conductivity contrast between air and rock matrix enhances the variations in thermal conductivity.

The second predictive model employs simpler mineralogy consisting only of sand and shale. Additionally, an empirical relationship is used between sonic velocity v_p, shale content V_{sh}, and porosity ϕ, established for shaly sandstones and a pressure range from 5 MPa to 40 MPa [*Han et al.*, 1986].

$$v_p[\text{km s}^{-1}] = a_0 - a_1\phi - a_2 V_{sh}. \tag{3.31}$$

The coefficients of this equation (table 3.7) are slowly varying functions of pressure. For any given pressure they can be interpolated linearly. Using the mean bulk density of the laboratory measurements of ρ_b = 2330 kg m^{-3}, depth is converted into lithostatic pressure which is needed in equation 3.31. For the γ-ray log, the linear log-response equation 3.30 is used, assuming no contribution to the radiation by the fluid:

$$GR = GR_{sn}V_{sn} + GR_{sh}V_{sh}. \tag{3.32}$$

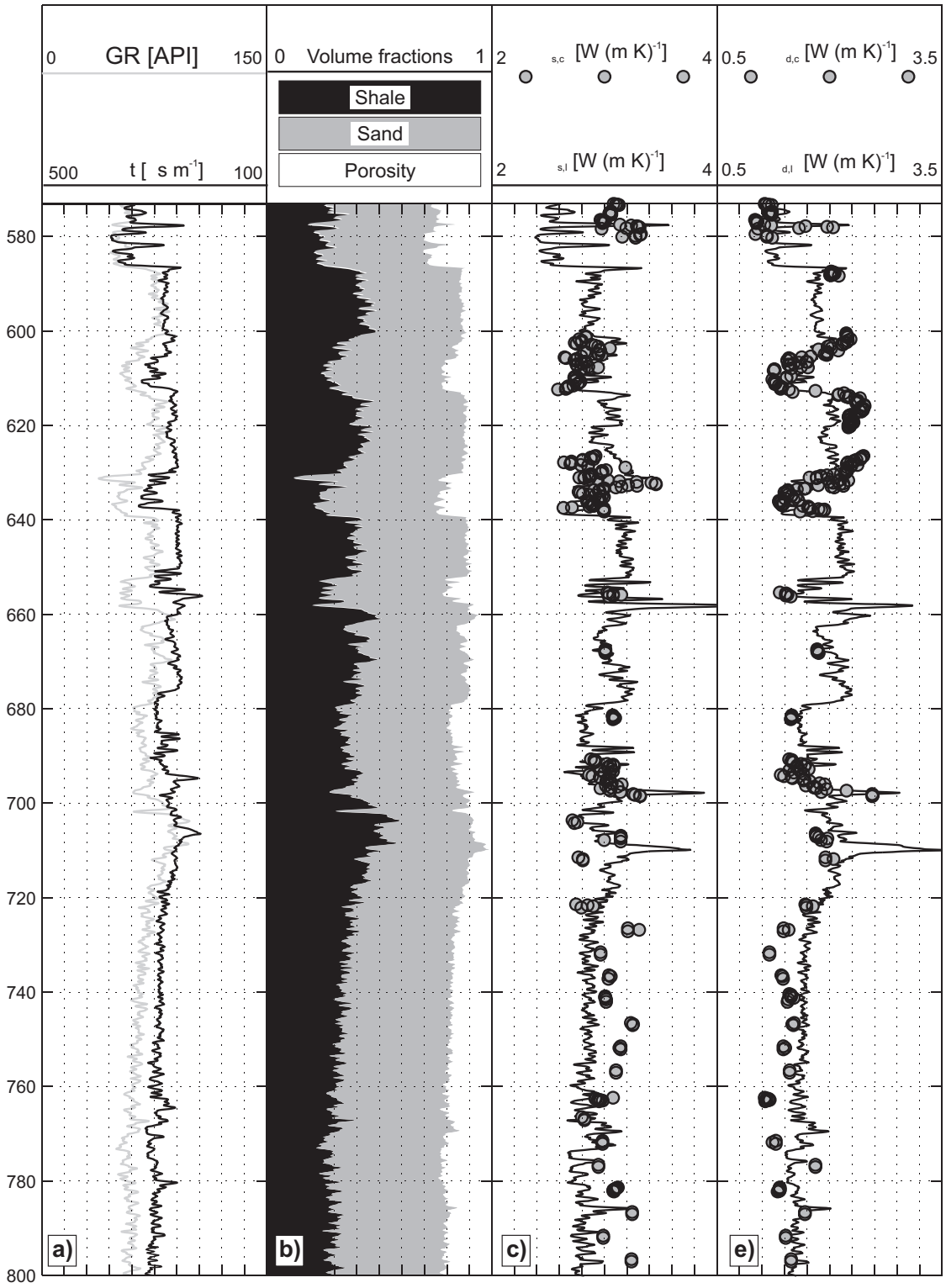

Figure 3.12: Model 2 (Sand-Shale) for the studied borehole. *a)* Input logs. *b)* Composition. *c)* Saturated thermal conductivity. *d)* Dry thermal conductivity. GR: Natural γ-radiation; Δt: Acoustic slowness; λ: Thermal conductivity. Index l: From log data; Index c: Core data; Index s: Saturated rock; Index d: Dry rock.

Here the subscripts sn and sh denote sand and shale, respectively. V_{sh} and V_{sn} are often expressed as fractions of the solid volume. Here they denote the fraction of the total volume. The rock properties used in the model are summarised in Table 3.6.

The resulting lithology profile is shown in figure 3.12. Again the model is tested for its suitability to predict thermal conductivities. For this purpose, the compositional log was sampled at the depths of the core measurements. Computed composition and measured values of thermal conductivity were then used in an inversion to find optimum mineral thermal conductivities of the constituents (Table 3.6) [8]. A synthetic log of thermal conductivity is then computed and compared to the measurements. The RMS-misfit of the two-component model 2 is 0.28 W(m K)$^{-1}$, essentially the same as for the three-component model 1.

When comparing the lithology logs for the two models it appears that they yield very similar shale volumes. The sand fraction of the two-component model also includes the missing carbonate fraction. This is also reflected in the lower mineral thermal conductivity of the sand/shale model. As a consequence, the model will be only successful when the ratio of sand and carbonates does not change too much. This can be seen when comparing figure 3.11 to figure 3.12 in the depth range from 615 m to 630 m: In contrast to model 1, the sand-shale model 2 cannot accurately reproduce the high thermal conductivities resulting from the large sand fraction.

Both models yield a better fit in the upper part of the profile than in the lower part below 700 m. This is most likely due to an overestimation of porosity for the cores analysed. Average core porosity in the depth range 750 m to 800 m is 20 % compared to only 17 % for log data. The difference may be attributed to the release of overburden pressure during coring [*Holt et al.*, 2003]. However, at this point, no porosity measurements under confining pressure could be performed to verify this effect. Depending on the geological setting and method to compute an overburden correction, correction factors of 0.85 to 0.95 have been reported [*Nieto et al.*, 1994]. It is to be expected that the samples studied respond strongly to the pressure relief due to their poor consolidation. In this situation, log derived porosities might be more accurate and reliable than core derived porosities highlighting the usefulness of log derived thermal conductivity.

3.5 Conclusions

Empirical relationships between thermal conductivity and other petrophysical properties depend on regional conditions, in particular the type of rock diagenesis. Core and log data from a borehole in the Molasse Basin were analysed in order to establish a set of equations. Empirical relationships from laboratory measurements of sonic velocity or bulk density allow to predict thermal conductivity to an accuracy of $\pm$ 0.2 W(m K)$^{-1}$, on average. Predicting thermal conductivity from logging data has a larger error of $\pm$ 0.3 W(m K)$^{-1}$. This is not surprising in view of the different spatial resolutions and the problems encountered in matching core and logging depths. However, this disadvantage is outweighed by the larger number of sampling points. An important restriction, common to all studies of this type, is that the results are valid only for the particular conditions in a specific regional setting.

[8] Again, the function `LSQCURVEFIT` of the Matlab™ package was used for this purpose. It is based on the interior-reflective Newton method described in *Coleman and Li* [1996].

An ideal combination of wireline logs for an optimum determination of lithology would comprise the full suite of nuclear measurements. In the case of the Molasse Basin, it is demonstrated that thermal conductivity can be derived even though the number of available logs is less than ideal. This is an important result, as for many old wells — drilled before the advent of modern logging tools — only natural γ-ray logs and sonic logs are available. The fact that thermal conductivities can be reconstructed based on this data alone makes these older wells attractive for such an analysis.

The discussion of laboratory data and of the two compositional models shows that this log combination is most useful in a setting dominated by sand and shale fractions. In contrast, a combination of sandstone and carbonate cannot be well characterised. The thermal conductivities of quartz and calcite differ by a large degree, providing a means to discriminate the two fractions. In the laboratory, rapid and accurate measurements of thermal conductivity can be obtained using the optical scanning technique [*Popov et al.*, 1999]. In the borehole, direct measurements of thermal conductivity are difficult. However, if a purely conductive regime can be assumed the temperature gradient is a proxy for the thermal resistivity. This makes the use of temperature data in the lithological inversion attractive, as it may help to distinguish between carbonate and quartz better than conventional wireline logs. An approach to this problem will be discussed in the next chapter where an inversion scheme is developed which includes temperature in the type of inverse analysis presented in this chapter.

Chapter 4

Joint inversion for thermal and petrophysical properties from wireline and temperature data

In petrophysical inversion from logging data, the tool response is modelled by a system of equations linking the volumetric composition of the rock to its physical properties. This technique has been successfully applied in reservoir evaluation using nuclear, sonic, and electrical log data. Temperature logging has played only a minor role in this scheme so far, mainly in the correction of temperature dependent properties, such as the electric conductivity of fluids. The difficulties to obtain undisturbed formation temperatures after drilling may explain this disregard. However, measurements of the undisturbed temperature gradient can help to constrain thermal conductivity and thus petrophysical properties of the rock. This can be particularly useful in geothermal applications requiring a consistent and joint interpretation of wireline and temperature data.

An inversion algorithm named LogInv will be presented that is able to invert simultaneously temperature logs and other wireline logs. The forward model incorporates variable layering and inclusion of shoulder effects for various tools. A Bayesian approach is used with a Tikhonov regularisation to solve the inverse problem. The algorithm is then tested against current algorithms. Applications of the model are presented in two case studies.

4.1 Forward model

The proposed algorithm has a modular structure. All forward models have the same interface and can be combined to yield composite log responses. New models can be easily added if they conform with the common interface and existing models can be modified to accommodate specific applications without the necessity to modify the inverse code.

A number of tool responses is already implemented in the project. Common to all tool equations is the model geometry (figure 4.1): The subsurface is divided into a number of horizontal model layers of variable thickness. The depth to the bottom of a layer l is given by z_l. A natural choice for the thickness is the sampling interval of the wireline logs, or a multiple of it for noise

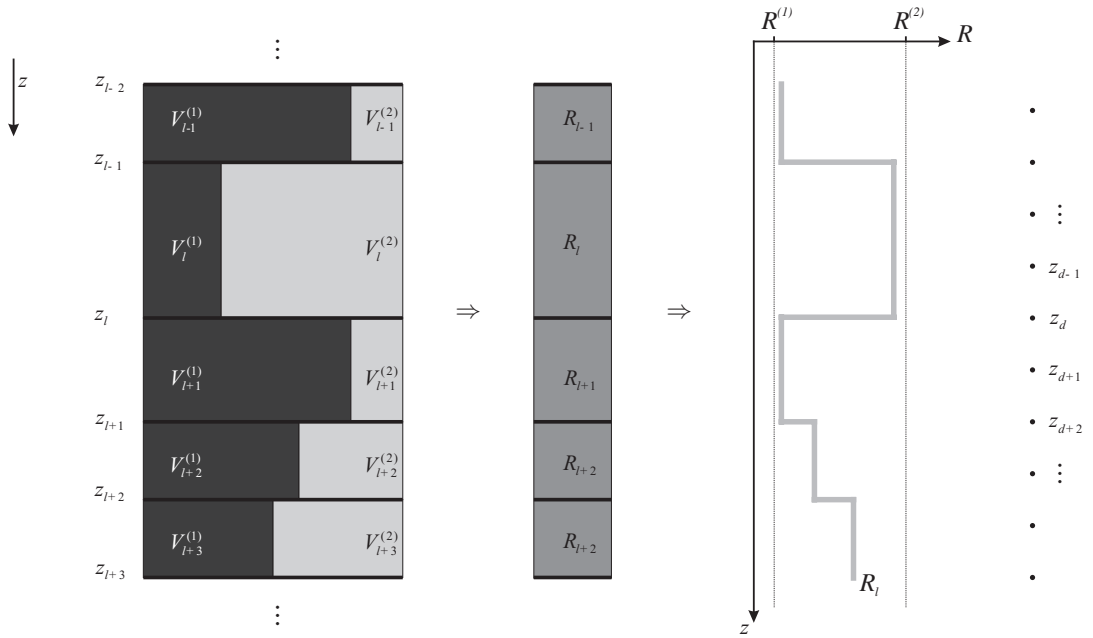

Figure 4.1: Geometry of the lithologic model. For each layer l an effective log response R_l is computed from the volumetric contents $V_l^{(n)}$ of the mineral or fluid component n.

suppression. For every layer, a number of components with fractional volumes $V_l^{(n)}$ is defined where the sum of the fractional volumes equals one. Additionally, the theoretical responses $R_l^{(n)}$ of the components are defined for each layer, for instance the density of the pore fluid and the rock matrix. Global parameters are used to define model parameters, such as surface heat flux density, or properties of the logging tools, for instance penetration depth for nuclear tools. They can be included in the inversion or excluded from it.

Based on this geometry the forward model is solved at the data depths z_d for all available measurements. The internals of this computation are entirely up to the forward model. However, in general the computation is a two-step procedure where the computation of an effective layer property or layer response is followed by spatial averaging to account for the finite resolution of the tool. The following sections present a number of examples for relevant tool equations.

4.1.1 Sonic tool

The first step in computing the sonic tool response consists in calculating the effective slowness Δt_l of the layer l. A number of relationships have been proposed for this purpose [*Mavko et al.*, 1998]. The most widely used one is the travel-time average [*Wyllie et al.*, 1956], equivalent to arithmetic averaging (equation 3.6). Here, the Raymer-Hunt-Gardner model [*Raymer et al.*, 1980] is used for porosity values less than 37 %:

$$\frac{1}{\Delta t} = \frac{\phi}{\Delta t_p} + \frac{(1-\phi)^2}{\Delta t_m}, \text{ for } \phi < 0.37. \tag{4.1}$$

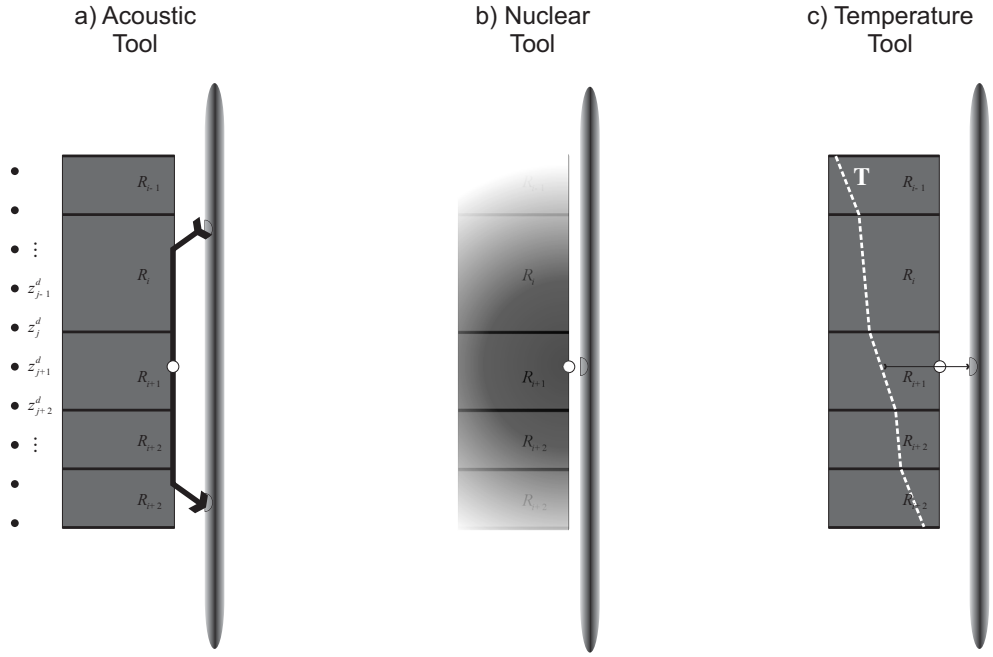

Figure 4.2: Schematics of the tool response geometry used in the forward model. a) sonic tool, b) density and γ-ray tools, c) temperature tool.

The indices p and m denote pore and matrix, respectively. In principle, the equation is valid only for a homogeneous rock matrix. As an approximation, the slowness of the solid is computed using the Wyllie time average [*Wyllie et al.*, 1956].

Once the effective layer slowness is calculated, the geometry of the tool needs to be considered (figure 4.2a). In principle, the arrival time difference of two or more receivers is measured and divided by their spacing. This value is assigned to the midpoint between the receivers. Borehole compensated (BHC) tools have a more complicated ray path but essentially they too have the receiver spacing d_r as a characteristic tool parameter. A simple approximation of the tool response can be computed as a weighted average of the slowness values of the layers that are probed by the tool:

$$\Delta t \quad = \quad \sum_l f_l \Delta t_l. \tag{4.2}$$

When computing Δt at data depth z_d, the sum is over all layers l that are at least partially within the interval $(z_d - d_r/2, z_d + d_r/2]$. The relative weight f_l of a layer is given by its thickness divided by the characteristic length d_r:

$$f_l = c\frac{z_l - z_{l-1}}{d_r}. \tag{4.3}$$

The correction factor c equals one for layers that are completely within the interval $(z_d - d_r/2, z_d + d_r/2]$. If a layer l is partially outside that interval, c corresponds to the ratio between

the part of the layer within $(z_d - d_r/2, z_d + d_r/2]$ and the total thickness of the layer:

$$c = \begin{cases} \dfrac{z_l - (z_d - d_r/2)}{z_l - z_{l-1}} & (z_l < z_d), \\ \dfrac{(z_d + d_r/2) - z_{l-1}}{z_l - z_{l-1}} & (z_l > z_d). \end{cases} \tag{4.4}$$

4.1.2 Density and natural gamma-ray tools

The same model is used for the passive γ-ray tool and the active $\gamma - \gamma$ density tool. The effective density and γ-ray value for each layer is computed as the weighted arithmetic average (equation 3.6) of the components.

The averaging process will be derived for the γ-ray tool. It is identical for the density tool. The unit impulse response $I(z)$ of a γ-ray tool to an infinitely thin radioactive layer with unit strength located at depth z' is modelled by an exponential decay function [*Hearst et al.*, 2000]:

$$I(z', z_d) = \frac{1}{2\alpha} \mathrm{e}^{-|z' - z_d|/\alpha} \tag{4.5}$$

In this equation, α is the characteristic length after which a unit impulse response has decayed to $1/\mathrm{e}$. It is a property of the formation, with typical values of about 30 cm for natural γ-ray tools [*Ellis*, 1987]. For example, 75 % of a monoenergetic source with an energy of 1.76 MeV derive from a vertical cylinder of 25 cm height and 14 cm radius around the borehole axis [*Hearst et al.*, 2000]. The total γ-ray value at a particular depth point $GR(z_d)$ is then given by the integral

$$GR(z_d) = \int_{-\infty}^{+\infty} GR_f(z') I(z', z_d) dz'. \tag{4.6}$$

$GR_f(z')$ is the continuous γ-ray value of the formation that varies with depth. In the layered case it is piecewise constant and equal to the effective layer GR_l computed in the first step. Thus, equation 4.6 becomes

$$GR(z_d) = \sum_l GR_l \int_{z_l - 1}^{z_l} I(z', z_d) dz'. \tag{4.7}$$

The solution of the sum of these integrals is given in Appendix A.2. In practise, only a finite number of layers is required for the computation. As a default, only the layers within $\pm 5\alpha$ of z_d are included which contribute 99 % to the expected signal. To ensure that the computed value corresponds to the complete infinite integral, a small correction factor $c(z_d)$ is applied:

$$c(z_d) = \frac{\int_{-\infty}^{+\infty} I(z', z_d) dz'}{\int_{z_t}^{z_b} I(z', z_d) dz'} = 2 \left(2 - \mathrm{e}^{-\frac{z_b - z_d}{\alpha}} - \mathrm{e}^{-\frac{z_d - z_t}{\alpha}} \right)^{-1}, \tag{4.8}$$

where z_b and z_t are the bottom depth and top depth of the actually used integration interval. The derivation is detailed in Appendix A.2.

4.1.3 Resistivity tool

Many rock-forming minerals are isolators. In this case the resistivity of rocks is due to the electrical properties of the pore fluid. This is generally expressed by Archie's equation [*Archie*, 1942]:

$$\frac{R_0}{R_w} = \phi^{-m}, \tag{4.9}$$

where m is the so-called cementation exponent, R_w is the brine resistivity, and R_0 is the resistivity of the brine-saturated rock. This equation was further modified into the relationship

$$\frac{R_0}{R_w} = a\phi^{-m}. \tag{4.10}$$

The coefficients a and m are empirical constants and depend on the rock type considered. For a discussion see for instance *Hearst et al.* [2000].

In addition to the properties of the pore fluid, electrical properties of shales are important for resistivity logging. Shales are fissile rocks of clay- to silt-sized particles. They contain large amounts of clay minerals that are responsible for the electrical properties. The effective electrical resistivity of the shale fraction depends on the amount and structure of the shale. Three types can be distinguished: (1) Laminar shale; (2) Structural shale; (3) Dispersed shale [*Anonymous*, 1989]. All three forms require slightly different petrophysical models. Often the simple "total shale relationship" can be used [*Anonymous*, 1989]:

$$\frac{1}{R_t} = \frac{\phi^m S_w^2}{aR_w(1 - V_{sh})} + \frac{V_{sh}S_w}{R_{sh}}. \tag{4.11}$$

Here, R_t is the resistivity of the rock saturated with hydrocarbon and water, S_w is the water saturation, V_{sh} is the shale volume fraction and R_{sh} is the shale resistivity. When no shale and hydrocarbon is present, equation 4.11 reduces to Archie's equation. In the case studied here, no hydrocarbon-bearing formations are examined, thus $S_w = 1$ and $R_t = R_0$ is the resistivity of the water saturated rock:

$$\frac{1}{R_0} = \frac{\phi^m}{aR_w(1 - V_{sh})} + \frac{V_{sh}}{R_{sh}}. \tag{4.12}$$

4.1.4 Temperature tool

The temperature tool differs from other tools because it records the state variable temperature, not the corresponding petrophysical property, thermal conductivity. A discussion of the appropriate mixing laws for thermal conductivity was presented in section 3.2. As long as experimental data do not suggest differently, it is most appropriate to use the geometric mixing model (equation 3.10) generalised to N components with volume fraction V_n. The effective thermal conductivity of the layer l, λ_l is then given by

$$\lambda_l = \prod_{n=1}^{N} \lambda_n^{V_n}. \tag{4.13}$$

The second petrophysical parameter is the heat production rate A. Depending on the available logging data, this parameter can be computed using the concentrations of Uranium, Thorium, and Potassium from the spectral γ-ray log SGR [*Rybach*, 1988] or from the total γ-ray log GR [*Bücker and Rybach*, 1996].

$$A(SGR) = 10^{-5}\rho_b(9.52c_U + 2.56c_{Th} + 3.48c_K) \quad [\mu\mathrm{W\,m^{-3}}], \tag{4.14}$$

$$A(GR) = 0.0158(GR - 0.8) \quad [\mu\mathrm{W\,m^{-3}}]. \tag{4.15}$$

The γ-ray log GR or SGR is computed in the forward model by calling the already described nuclear functions that will convert the volume fractions and mineral properties into an effective γ-ray value.

Neglecting advective heat transport and assuming a 1D problem the heat transport equation can be solved for a homogeneous half space (2.1) or a horizontally stratified earth where l is the layer index:

$$T(z) = T_0 + q_0 \sum_l \frac{\Delta z_l}{\lambda_l} + \frac{1}{2}\sum_l \frac{A_l \Delta z_l^2}{\lambda_l} + T_t(z). \tag{4.16}$$

The notation is the same as in equation 2.1. The representation and the extension to the stratified case is straightforward for the conduction and heat production terms. The transient part $T(t)$, however, requires further consideration: An analytic expression for the case of a series of step changes in ground surface temperature was given by *Nielsen and Balling* [1985] but the model has restrictions regarding the layer width. Solving the problem using a finite difference algorithm is straightforward [*Rath and Mottaghy*, 2007]. However, this can be time-consuming as the temperature-depth profile needs to be computed for every time step with high spatial resolution. Based on the results presented in chapter 2 a solution can be obtained under the assumption of a homogeneous subsurface for the transient term, i.e. by using the effective average diffusivity over the depth profile. Both methods are available and the decision which one to use should be based on the desired accuracy and the complexity of the geological profile.

It should be noted that equation 4.16 does not include a shoulder effect for the temperature as it is a point measurement (see also figure 4.2), implying a very high vertical resolution. In reality, temperature readings are affected by several processes which may decrease the spatial resolution. *Gretener* [1967] states that "most oil wells must be thermally unstable". He observed fluctuations on the order of 10^{-2} K on continuous temperature recordings taken at one depth. Another problem is that the logging speed of the probe and the response time of the sensor result in a depth lag of the temperature readings [*Reiter et al.*, 1980]. This lag can be computed roughly as the product of logging speed and response time. Standard wireline speed is about 10 m min^{-1}. Assuming a speed of 5 m min^{-1} and a response time of 2 s produces a lag of 17 cm, roughly the sampling interval of wireline logs. Because this error is on the same order as the random fluctuations, it is not necessary to include it in the forward model. However, very high resolution measurements need to take this effect into account.

4.2 Bayesian Inversion procedure

After defining the forward model in the preceding section, the inverse problem can now be solved. It can be written as [*Tarantola*, 2005]

$$\mathbf{g}(\mathbf{x}) = \mathbf{d}, \tag{4.17}$$

that is, the forward operator $\mathbf{g}$ maps a model $\mathbf{x}$ onto the data $\mathbf{d}$. Inverting this equation means to find an generalised inverse operator $\mathbf{g}^{-i}$ so that

$$\mathbf{x} = \mathbf{g}^{-i}(\mathbf{d}). \tag{4.18}$$

Generally, this problem cannot be solved exactly. Rather, a solution $\mathbf{x}$ must be sought that is in some sense optimal. This is usually accomplished by a least-squares fit, i.e. by finding the model $\mathbf{x}$ that minimises the quadratic misfit between model prediction and data

$$\phi_{LS}(\mathbf{x}) = ||\mathbf{g}(\mathbf{x}) - \mathbf{d}||_2.$$

This equation has to be modified to take into account variable data errors and correlations by introducing the data covariance matrix $\mathbf{C_d}$. Another modification is introduced by using prior information about the model. In the Bayesian framework, this is done by using an a-priori parameter vector $\mathbf{x_p}$ and its associated covariance matrix $\mathbf{C_p}$. These two modifications lead to the general formulation of the nonlinear Bayesian functional [*Tarantola*, 2005]

$$\phi_B(\mathbf{x}) = [\mathbf{d} - \mathbf{g}(\mathbf{x})]^T \mathbf{C_d}^{-1} [\mathbf{d} - \mathbf{g}(\mathbf{x})] + \epsilon(\mathbf{x} - \mathbf{x_p})^T \mathbf{C_p}^{-1} (\mathbf{x} - \mathbf{x_p}), \tag{4.19}$$

where ϵ is a regularisation weight. Minimising this functional yields a solution to the inverse problem posed in equation 4.18.

For the problem of inverting wireline logs, the forward operator $\mathbf{g}$ is given by the equations relating lithology to a tool response. The model itself consists of the volume fractions and properties of the components at each depth level and possibly global parameters. Here, "global" means that the parameter is not related to a particular depth but to all data, such as structural parameters or heat flux density. The solution will then be a model that minimises the misfit between recorded and modelled wireline data constrained by a-priori information. For instance, this may comprise laboratory measurements of mineral properties or porosity. Each particular application may make use only of a subset of the possibilities offered by this approach. For instance, an inversion for volumetric composition only, as is often done in the hydrocarbon industry, would require no global inversion parameters. In contrast, an inversion for paleoclimate does require them.

The non-linear equation 4.19 will be solved iteratively by an Quasi-Newton scheme described in the following section. For this scheme, the Jacobian matrix needs to be calculated, i.e. the derivative of the data with respect to the model. Because it is of paramount importance to compute the Jacobian efficiently and accurately, a separate section (4.2.2) is devoted to this problem where the technique of automatic differentiation is introduced.

4.2.1 Implementation of the minimising scheme

An iterative algorithm must be used to find the minimum of the non-linear equation 4.19. Here, the standard technique of Quasi-Newton iteration [*Tarantola and Valette*, 1982; *Tarantola*, 2005] is used:

$$\mathbf{x}^{k+1} = \mathbf{x}^k + \gamma^k \Delta\mathbf{x}^k. \tag{4.20}$$

Starting with an initial guess $\mathbf{x}^0$, the model $\mathbf{x}^{k+1}$ at iteration $k+1$ is updated from the model at the previous iteration k using the vector $\Delta\mathbf{x}^k$, given by

$$\Delta\mathbf{x}^k = \left(\mathbf{J}^T {\mathbf{C_d}}^{-1}\mathbf{J} + {\mathbf{C_p}}^{-1}\right)^{-1}\left(\mathbf{J}^T {\mathbf{C_d}}^{-1}[\mathbf{d} - \mathbf{g}(\mathbf{x}^k)] - {\mathbf{C_p}}^{-1}[\mathbf{x}^k - \mathbf{x_p}]\right). \tag{4.21}$$

Here, $\mathbf{J}$ is the Jacobian matrix, containing the partial derivatives of the forward model output with respect to the model parameters. The normalised RMS-error e of the model is computed after each iteration k:

$$e = \left(\frac{1}{N}\sum_i^N \frac{(d_i - g_i(\mathbf{x}))^2}{\sigma_d^2}\right)^{\frac{1}{2}}. \tag{4.22}$$

If the model can be fitted consistently to the data, the normalised RMS error of the final model should be close to one. The iteration is terminated if the change in RMS-error falls below a predefined threshold or if the change in RMS-error is small.

The multiplier γ^k is part of a simplified line search scheme following each iteration k to ensure a monotonically decreasing RMS-error e^k. If

$$e^{k+1} < e^k \quad \Rightarrow \quad \gamma^k = 1.$$

If this condition is violated, a new trial value γ_t^k is computed:

$$e^{k+1} \geq e^k \quad \Rightarrow \quad \gamma_t^k = 0.5 \cdot \gamma^k.$$

The multiplier γ_t^k is then repeatedly halved until either $e^{k+1} < e^k$ or a predefined maximum number of iterations is reached. This line search is necessary because, in the case of non-linearity, the vector $\Delta\mathbf{x}^k$ might point into the right direction, but possibly with a wrong magnitude.

The parameter vector $\mathbf{x}$ always contains the volume fractions V_i of the components i. These parameters are constrained by

$$V_i \in [0,1], \tag{4.23}$$

$$\sum_i V_i = 1. \tag{4.24}$$

Two methods have been tested to deal with this issue. The first one involves transforming the corresponding parameters. The summation constraint is turned into an implicit constraint by internally reducing the number of V_i's per depth level by one. I.e., for N components, only V_i ($i = 1, ..., N-1$) components will be independent and $V_N = 1 - \sum_1^{N-1} V_i$. These are then mapped from the interval $(0,1)$ to the interval $(-\infty, \infty)$ using the logarithmic transform

$$V_i' = \log_{10}\frac{V_i}{1 - V_i}. \tag{4.25}$$

However, this solution does not produce good results because 0 and 1 are not within the mapped interval. Components with zero volume, or for practical purposes with very low volume, cannot be modelled accurately. The second method implements the summation constraint as an additional equation for the volume fractions. This equation is given a large weight (on the order 10^2) to enforce the constraint. It is checked after each iteration if any volume fraction is outside its bounds $[0, 1]$. Values outside the bounds are adjusted to 0 or 1.

An a-posteriori covariance matrix can be computed from

$$\mathbf{C}_p^{apo} = \left(\mathbf{J}^T \mathbf{C}_d^{-1} \mathbf{J} + \mathbf{C}_p^{-1}\right)^{-1}, \tag{4.26}$$

which allows to assess the parameter uncertainties. This equation is correct in the strict sense only for linear inverse problems but may be used for non-linear problems if it can be approximated linearly in the vicinity of the solution [*Menke*, 1989].

4.2.2 Computing the Jacobian

Equation 4.21 requires computing the Jacobian matrix $\mathbf{J}$. This matrix contains the derivatives of all model responses R_i with respect to all model parameters x_j.

In the algorithm used here, two alternative methods are available for computing $\mathbf{J}$: Finite differences (FD) and automatic differentiation (AD). With regard to finite differences, a one-sided representation is written as follows:

$$\frac{\partial R_i}{\partial x_j} = \frac{R_i(\mathbf{x}') - R_i(\mathbf{x})}{h}. \tag{4.27}$$

$\mathbf{x}'$ is the modified parameter vector where the j-th entry is modified by the finite step h:

$$x'_k = \begin{cases} x_k & \text{for } k \neq j \\ x_k(1+h) & \text{for } k = j \end{cases} \tag{4.28}$$

In addition to this conventional method, automatic differentiation (AD) [*Rall and Corliss*, 1996; *Griewank*, 2000] was implemented in the inversion algorithm. The functionality of AD is implemented in a compiler that takes one or more functions as input and creates the corresponding functions for the computation of the derivative. The compiler needs to be designed specifically for the programming language used. For MATLAB™, such a compiler is provided by the software package ADiMat[9] [*Bischof et al.*, 2002, 2003].

The basic idea of automatic differentiation is the application of the well known rules of differentiation to the statements of a computer program. Consider, for example, the computation of the following statement [after *Griewank*, 2000]:

$$z = (\sin(y_1/y_2) + y_1/y_2)^2. \tag{4.29}$$

[9] ADiMat Homepage: `http://www.sc.rwth-aachen.de/vehreschild/adimat/index.html`. Implementation of ADiMat in the code used here was performed in cooperation with the Institute for High-Performance Computing at RWTH Aachen University.

Table 4.1: Evaluation trace for equation 4.29 as it may be implemented in a computer code. *Left:* Evaluation trace for the original code. *Right:* Evaluation trace for the derived code.

Original code			Derived code		
s_{-1}	$=$	y_1	s'_{-1}	$=$	y'_1
s_0	$=$	y_2	s'_0	$=$	y'_2
s_1	$=$	s_{-1}/s_0	s'_1	$=$	$1/s_0 s'_{-1} - s_{-1}/s_0^2 s'_0$
s_2	$=$	$\sin s_1$	s'_2	$=$	$s'_1 \cos s_1$
s_3	$=$	$s_1 + s_2$	s'_3	$=$	$s'_1 + s'_2$
s_4	$=$	s_3^2	s'_4	$=$	$2 s_3 s'_3$
z	$=$	s_4	z'	$=$	s'_4

In a computer program this computation is represented by a specific *evaluation trace*, shown in table 4.1 (left). The computation is subdivided into smaller computations with inputs s_{-1}, s_0 and intermediate variables s_i, $i > 0$. In the forward mode of automatic differentiation, the evaluation trace is modified by "augmenting" the original statements with their corresponding derivative statements (table 4.1, right). The augmented code can compute simultaneously a function value z and its derivative z'. This way, a derivative with respect to a variable is obtained at the expense of little additional computing time.

Figure 4.3 shows the sorting of the entries in a Jacobian matrix as implemented in the algorithm used here. Only the part relevant for the computation of volumes is shown, but for the mineral properties a similar structure would arise. Most of the entries of the matrix **J** are zero because of the localised nature of the forward functions: The tool response at a depth level i will only depend on the parameters of layer n if the depths are close together. Thus, the sorting results in a banded structure of the matrix. Consider a typical problem: Three types of measurements with a vertical resolution of 0.1 m over an interval of 200 m are used, resulting in 6000 data values. The lithologic model consists of three components and is discretised at 0.5 m interval, yielding 1203 parameters. The full Jacobian matrix, containing all partial derivatives, thus has a dimension of 6000×1203. If the response of a particular tool is influenced by a rock volume within 3 m of its sensor midpoint, only 5 to 6 layers will contribute to the tool reading at a given tool depth. This results in about $6000 \times 3 \times 5$ non-zero partial derivatives. The density of a sparse matrix is defined as the ratio of non-zero elements to the total number of elements. Thus, the resulting sparse matrix (figure 4.4) has 95760 non-zero elements, corresponding to a density of 0.013.

Two problems arise from this configuration: (1) It requires a large amount of memory for storage and computation; (2) Most of the CPU time is spent to compute the zero elements of **J**. The first problem is solved by representing **J** and all other matrices in equation 4.21 as sparse matrices [*Gilbert et al.*, 1992]. Routines for handling sparse matrices are readily available within MATLAB™, reducing considerably the memory requirements. The second problem is solved by optimising the number of derivatives to be computed using the Curtis-Powell-Reid (CPR)

$$\mathbf{x} = \left[\begin{pmatrix} V_1^1 & \cdots & V_1^M \end{pmatrix} \begin{pmatrix} V_2^1 & \cdots & V_2^M \end{pmatrix} \cdots \begin{pmatrix} V_L^1 & \cdots & V_L^M \end{pmatrix} \right]^T$$

$$\mathbf{d} = \left[\begin{pmatrix} R_1^1 & \cdots & R_1^N \end{pmatrix} \begin{pmatrix} R_2^1 & \cdots & R_2^N \end{pmatrix} \cdots \begin{pmatrix} R_D^1 & \cdots & R_D^N \end{pmatrix} \right]^T$$

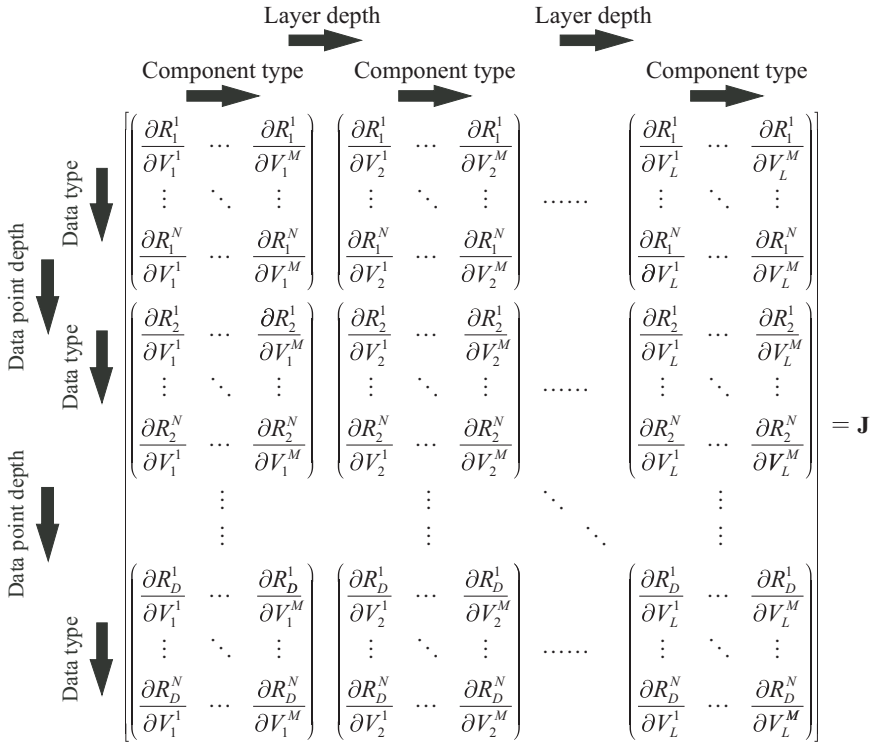

Figure 4.3: Structure of the Jacobian matrix **J** used for the inversion of volumetric composition from wireline data. V_l^m: Volume fraction of component m in layer l; R_d^n: Response of tool n at depth level d; M: Number of components; L: Number of layers; D: Number of data depth points; N: Number of tools.

approach [*Curtis et al.*, 1974]. In this approach a *seed matrix* is used that maps the $P \times Q$ Jacobian matrix into a compressed matrix of size $P \times T$, effectively reducing the number of columns and thus the number of function evaluations. This is demonstrated for an example matrix **J** with the structure:

$$\begin{array}{cc} \text{in} & \begin{array}{ccccc} 1 & 2 & 3 & 4 & 5 \end{array} \\ \mathbf{J} = & \begin{bmatrix} 0 & 0 & a & 0 & b \\ c & d & 0 & 0 & 0 \\ e & 0 & 0 & f & 0 \\ 0 & 0 & 0 & g & 0 \\ 0 & 0 & h & 0 & 0 \end{bmatrix} \begin{array}{c} 1 \\ 2 \\ 3 \\ 4 \\ 5 \end{array} \end{array} \quad \text{out}$$

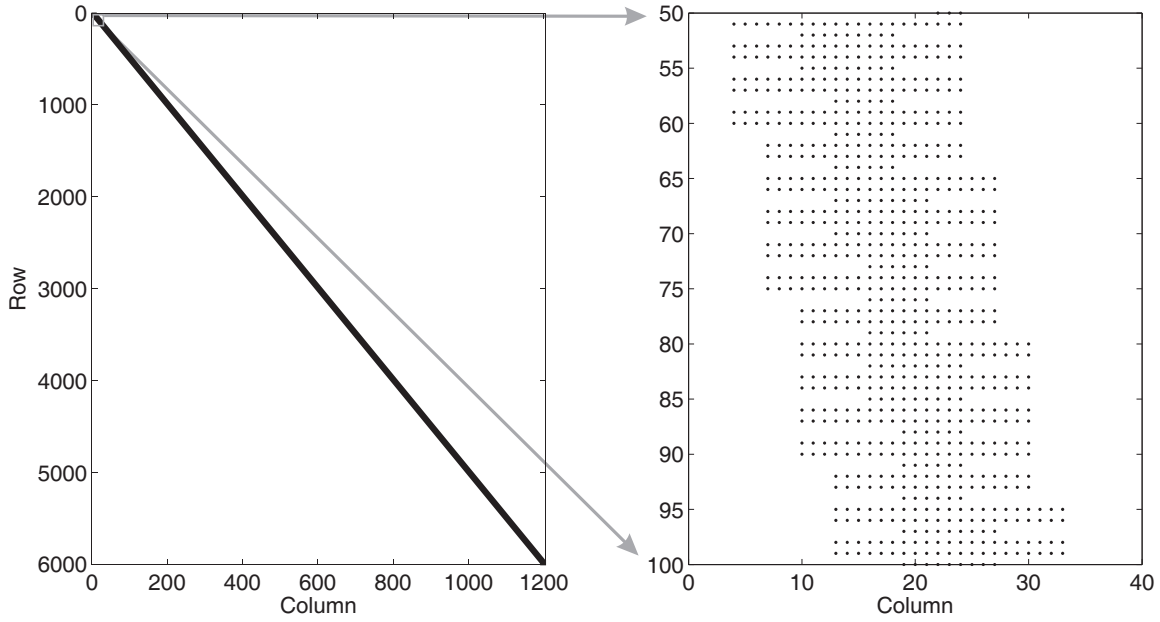

Figure 4.4: Structure of the Jacobian for a problem size of 6000×1203 and an overall density of 0.013. The plots show the non-zero elements. *Left:* Overview of the structure. *Right:* Zoom of the matrix diagonal. The sorting corresponds to figure 4.3. Each row contains a tool response for one data depth point. Here, three components are used, leading to $3N$ non-zero elements with N contributing layers. In this case $N = 7$ and $N = 3$. In general, N varies for tools with different sensitive volumes.

The non-zero elements of $\mathbf{J}$ are ordered alphabetically to distinguish them from each other. Each column lists the output variables that depend on the corresponding input variable. For instance, input parameter 1 (column 1) influences output variables 2 and 3 (rows 2 and 3). Since output 2 also depends on input 2, the derivative with respect to input parameters 1 and 2 cannot be computed simultaneously. However, inputs 1 and 3 influence only mutually exclusive outputs and can be computed simultaneously. Further analysing the matrix yields the seed matrix $\mathbf{S}$ and the compressed Jacobian $\mathbf{J}_c$

$$\mathbf{J}_c = \begin{bmatrix} b & a \\ c & d \\ e & f \\ 0 & g \\ 0 & h \end{bmatrix}, \quad \mathbf{S} = \begin{bmatrix} 1 & 0 \\ 0 & 1 \\ 0 & 1 \\ 0 & 1 \\ 1 & 0 \end{bmatrix},$$

related to the full matrix $\mathbf{J}$ via the relationship

$$\mathbf{J}_c = \mathbf{J}\mathbf{S}.$$

This compressed Jacobian can be evaluated using just two instead of five forward calculations. Every derivative can be uniquely identified within the compressed matrix and the full Jacobian $\mathbf{J}$

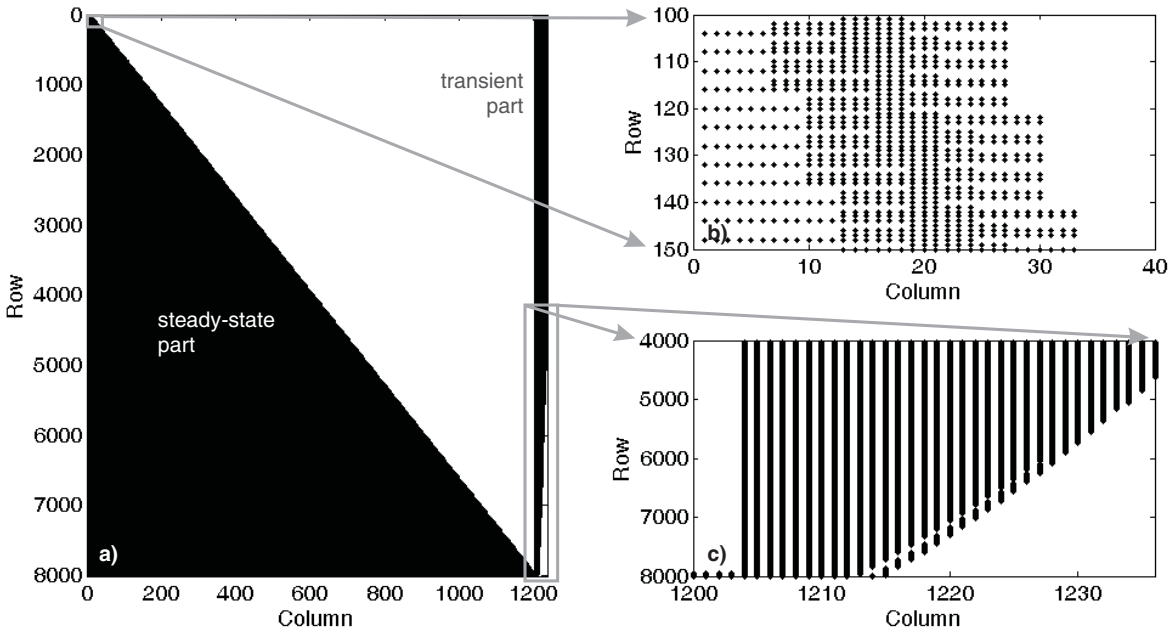

Figure 4.5: Structure of the Jacobian for a problem size of 8004×1236 and an overall density of 0.14. The matrix contains derivatives with respect to temperature, heat flux density, and GSTH. The plots show the non-zero elements. *a)* Overview. *b)* Main diagonal, every fourth row holds the temperature derivatives. These are sensitive to all volumes above (i.e. left) of the reading. *c)* Zoom into the transient part, time before present increases to the left, thus influencing the deeper parts of the temperature profile.

can be obtained afterwards by re-indexing of the elements of $\mathbf{J}_c$. The main task involved in the compression is to find an appropriate seed matrix with as little a number of columns as possible. This is equivalent to finding the *chromatic number* in graph theory. Heuristic methods can be used that achieve an almost optimal compression [*Griewank*, 2000][10].

The compression ratio of the example above is not very large. In reality, compression can be much more efficient. For the first example given (figure 4.4), compression reduces the problem from 1203 columns to only 21 columns. The density of the matrix increases from 0.013 to 0.76 and the number of function evaluations reduces by a factor of 60.

The effectiveness of the scheme varies considerably with the structure of the matrix. In the second example (figure 4.5), the 8004×1236 matrix is reduced to 1213 columns, resulting in a negligible performance increase. It is known [*Griewank*, 2000] that, depending on the matrix structure, other methods of compression may yield better results than CPR seeding. However, in this case, due to the dense lower triangle of the matrix these will also fail. One way to improve performance for this particular problem is to cast the heat conduction equation in terms of temperature gradient rather than temperature. If the heat production rate is assumed to be known, for instance from equation 4.14, the temperature gradient at a specific depth depends only on the local value of λ and the global parameter q_0 (see equation 4.16 for comparison). This would set

[10]Here, a modified version of the MATLAB™-function `COLOR` is used.

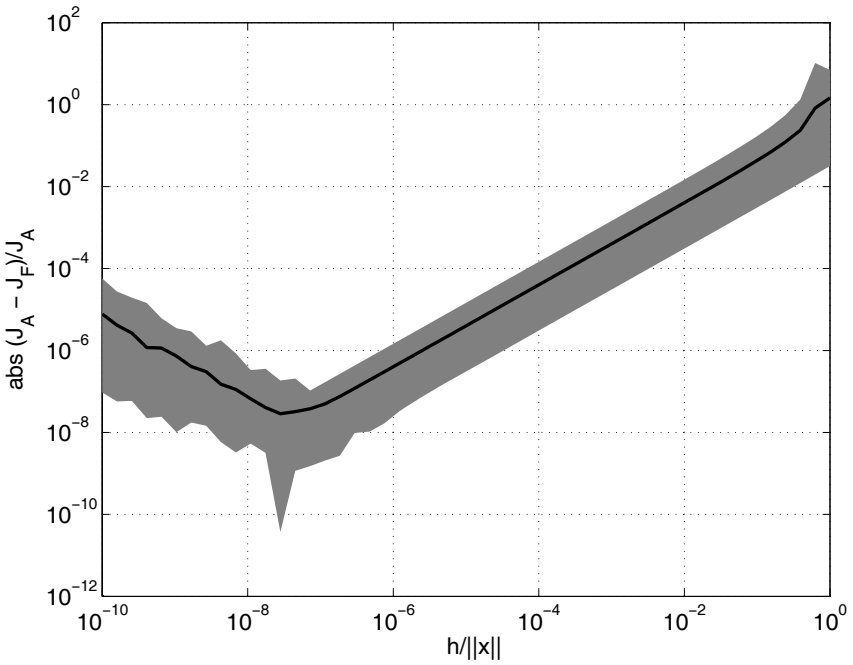

Figure 4.6: Comparison of resulting Jacobians for finite differences $\mathbf{J}_F$ and automatic differentiation $\mathbf{J}_A$. Results are shown for the derivative of the sonic tool function with respect to the volume fractions. The relative difference between both methods is plotted versus the relative step size $h/||\mathbf{x}||$ of the finite difference algorithm. The black line shows the mean, the shaded area denotes the minimum-maximum range.

most of the off-diagonal elements in figure 4.5 to zero. In terms of performance it is therefore important to consider the most efficient way to represent a particular forward function.

4.3 Analysis of the algorithm

The proposed algorithm is subjected to a number of tests to secure its proper function. First, a comparison of the AD and FD method will be given, followed by an error analysis for a problem using temperature data. This will be supplemented by a synthetic example. The code is then verified against two established programs, both providing a subset of the functionality presented here. Correct functioning of the conventional forward functions for the wireline tools is tested against the output of the commercial inversion program ELANPlus™ [*Anonymous*, 1999]. Inversion results of the transient temperature function are tested using the algorithm “Joint”, already introduced in chapter 2.

4.3.1 Comparison of automatic differentiation and finite differences

In general, both methods for computing derivatives lead to similar results. This is shown in figure 4.6, where the difference between the two methods is plotted versus the relative step size

$h/||x||$ of the finite difference algorithm (equation 4.27). The sonic tool response (section 4.1.1), differentiated with respect to the volume fractions has been used here as an example. As expected, the differences between the two methods become smaller until the relative step size is decreased to about 10^{-7}. Below this value, numerical limitations in computing the small finite differences become more and more important and the error increases again. Assuming the correctness of the AD method, the minimum value of the resulting curve would be the optimum step size to use for the finite difference method. In the proposed algorithm the the FD method can be used with a predefined value, with the default being set to 10^{-7}. It is one advantage of the AD method, that it does not require such a choice as the results are exact to machine precision.

4.3.2 A-posteriori variance using temperature data

Using a particular model, an a-priori model covariance matrix, and a data covariance matrix, the a-posteriori covariance matrix can be computed. It needs to be stressed that the uncertainties computed in the following are only applicable to the model studied here. Because any permutation of data types and volume types is possible, the uncertainties for an arbitrary model are difficult to specify.

The model used in this section consists of quartz, illite, calcite, and water, all with known properties. Logging data used for computing the volume fractions comprises γ-ray, bulk density, and sonic slowness. In addition, one of the following logs is used: Temperature, photoelectric effect, or neutron porosity. This way, the resolving power of temperature relative to other log types can be evaluated. Layer thickness Δz_l and data sampling interval Δz_d are equidistant, with the former being a multiple of the latter. This "oversampling ratio" $r_o = \frac{\Delta z_l}{\Delta z_d}$ can be used for noise suppression. For a given set of input data (i.e. constant Δz_d), r_o is increased by making Δz_l larger. A higher value will improve the a-posteriori variance but also decrease the vertical resolution of the inverted volume fractions.

The results (figure 4.7) indicate that the use of a temperature log for computing volumes is of similar value as the use of a neutron porosity log. Even better results can be obtained using data of a photoelectric logging tool because of the vastly different PE responses of calcite and quartz. It is also apparent that the variance of the result is unacceptably high for quartz and calcite if temperature or neutron porosity are considered as the fourth data source. This can be partly remedied by increasing the layer spacing. However, best results are obtained with a selection of data that is most appropriate to discriminate the expected volume fractions.

With the same model, reproducibility was tested by repeated inversion using a randomised initial guess (50 times) and increasing the regularisation weight ϵ. Table 4.2 shows that the uncertainty is small compared to other sources of error and that regularisation has no significant influence on the results.

4.3.3 Synthetic example

As an example for a synthetic data set, a model is considered that consists of sand (quartz), shale (illite), and carbonate (calcite). The model consists mainly of shale, with sandy and carbonaceous layers. Data types are sonic log, bulk density, and γ-ray. The forward model (shown in figure 4.8,

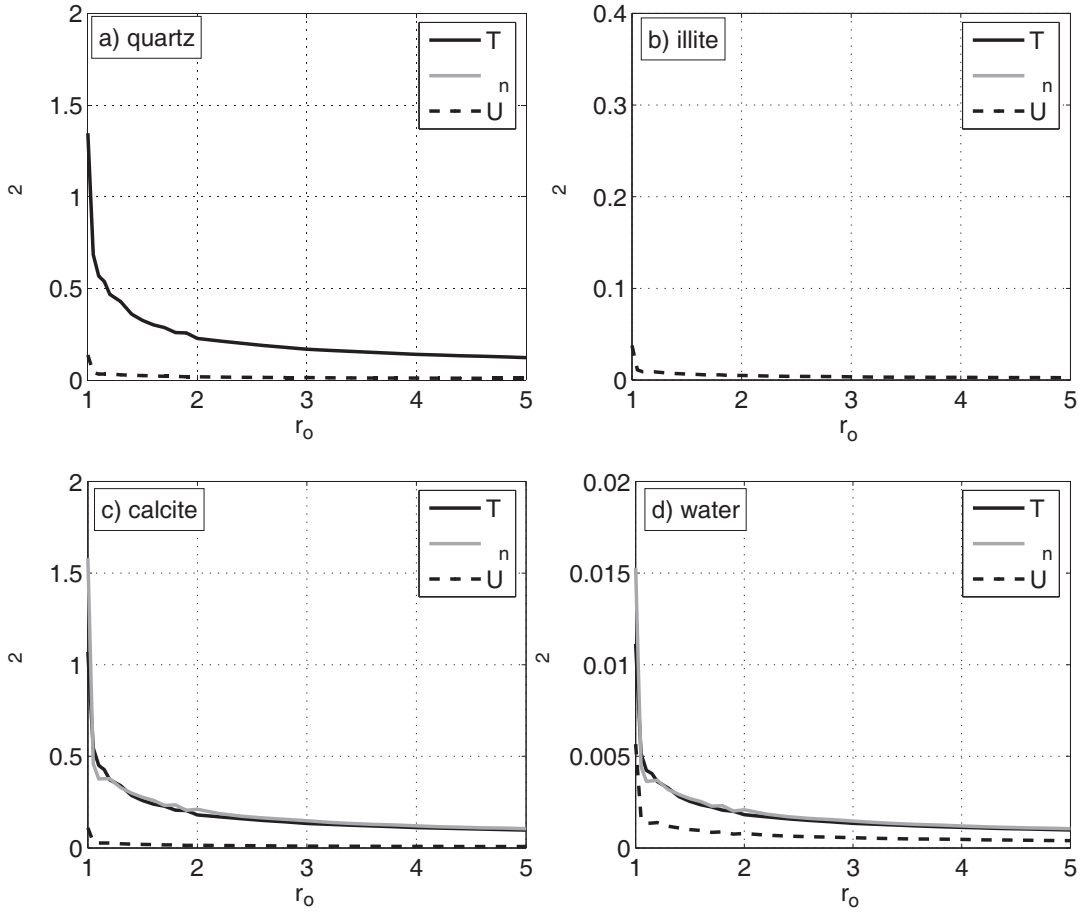

Figure 4.7: A-posteriori variance σ^2 for model volume fractions using different log types and varying values of oversampling ratio r_o. T: Temperature; ϕ_n: Neutron porosity; U: Photoelectric effect.

Table 4.2: Reproducibility of the algorithm. Numbers represent the standard deviation σ of all solutions. ϵ: Regularisation weight (equation 4.19); Δt: Acoustic slowness; GR: γ-radiation; ρ_b: Bulk density.

ϵ	$\sigma(\Delta t)$ [%]	$\sigma(GR)$ [%]	$\sigma(\rho_b)$ [%]
10^0	0.29	0.20	0.016
10^1	0.02	0.08	0.006
10^2	0.01	0.03	0.002

track a) is used to compute a synthetic data set for a section of 100 m length, using the theoretical log responses of table 3.5. Normal noise is then added to the data, with increasing noise level from top to bottom. Thus, the top part represents high quality data while the bottom part stands for poor data quality. Noise parameters are summarised in table 4.3. The ratio of layer thickness

Table 4.3: Range of normal noise added to the data of figure 4.8. The value increases linearly with depth between the two end values.

Log		Error		
GR	[API]	7.5	-	60
Δt	[μs m^{-1}]	5	-	40
ρ_b	[kg m^{-3}]	25	-	200

to data spacing equals two.

The noisy data is then fed into the inversion scheme to compute a volumetric composition. The comparison between model and inverted data set is shown in figure 4.8. The general features of the model are reproduced well for all noise levels, but the number of outliers in the inverted model increases strongly with noise magnitude. Data are smoothed out by the lower sampling of the layers and thus reproduce rather the noiseless original data than the noisy data input to the inversion. The computed standard deviations for this particular example are below 5 volume percent. As discussed in the previous section, a reduction of the model error can be achieved by reducing the vertical resolution, i.e. increasing the layer thickness. The increasing data noise is mainly reflected in the model error for the shale fraction. The shale fraction is almost entirely determined by the single GR-equation, leading to a direct correlation between model and data error. This effect is somewhat subdued for the other volume fractions.

4.3.4 Comparison with "Joint"

To verify the transient temperature equations implemented in the inversion code LogInv it is compared to the results of the "Joint" algorithm [*Mareschal and Beltrami*, 1992]. A 500 m deep synthetic temperature log sampled at 5 m interval is used. Steady-state surface heat flux density is 0.06 W m^{-2}, thermal conductivity is 2.5 W(m K)$^{-1}$, and volumetric specific heat capacity is 2.3 MJ m^{-3} K^{-1}. The transient signal corresponds to a step increase in ground surface temperature 20 years before present. The inversion for composition is switched off for this experiment.

The two approaches differ with respect to regularisation. The code used here is based on a Bayesian approach using both data and a-priori model covariance. This is somewhat different from the approach used in "Joint" where an ad-hoc regularisation parameter ϵ in a dampened least-squares procedure is implemented. To compare both algorithms, a special form of the covariance matrices must be found that is equivalent to the dampened least-squares solution. This is possible if the data and parameter covariance matrices can be written as $\mathbf{C_d} = \sigma_d^2\mathbf{I}$ and $\mathbf{C_p} = \sigma_x^2\mathbf{I}$. The functional 4.19 can then be written as [*Aster et al.*, 2004]

$$\phi(\mathbf{x}) = \frac{1}{\sigma_d^2}||\mathbf{G}(\mathbf{x}) - \mathbf{d}|| + \frac{1}{\sigma_x^2}||\mathbf{x} - \mathbf{x_p}||. \tag{4.30}$$

$\phi(\mathbf{x})$ has obviously the same minimal $\mathbf{x}$ as the functional $\phi'(\mathbf{x})$, given by

$$\phi'(\mathbf{x}) = ||\mathbf{G}(\mathbf{x}) - \mathbf{d}|| + \frac{\sigma_d^2}{\sigma_x^2}||\mathbf{x} - \mathbf{x_p}||. \tag{4.31}$$

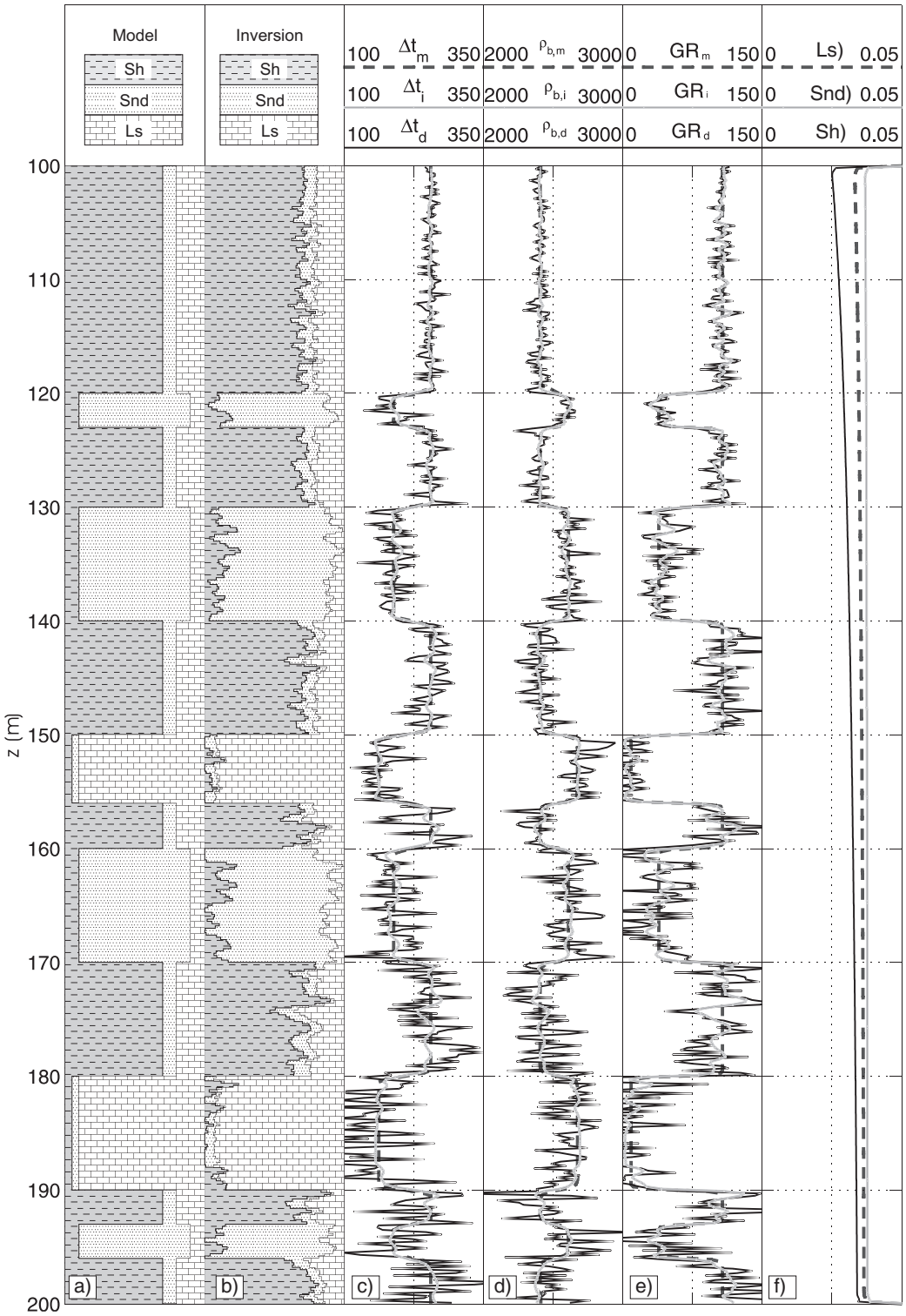

Figure 4.8: Synthetic lithological model and inversion results. *a)* Input model. Snd: Sand; Sh: Shale; Ls: Limestone. *b)* Inverted model. *c) – e)* Synthetic data computed from input model (Dashed line, index m); Synthetic data with noise added (Black line, index d); Data computed from inverted composition (Grey line, index i). *GR*: γ-ray; Δt: Acoustic slowness; T: Temperature. *f)* Computed standard deviation σ for the volumetric components of the inverted model.

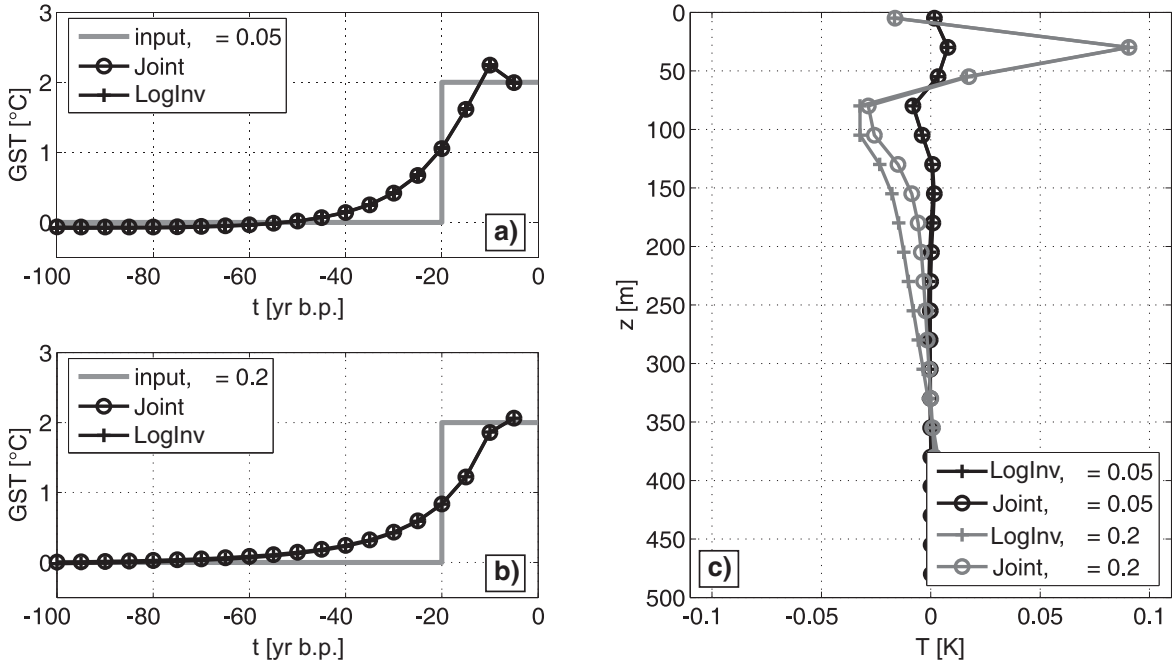

Figure 4.9: Comparison of Bayesian inversion of "LogInv" and a dampened least-squares solution of "Joint" [*Mareschal and Beltrami*, 1992] for different values of the damping parameter ϵ. *a)* Input GSTH and inverted GSTH for $\epsilon = 0.05$. *b)* Input GSTH and inverted GSTH for $\epsilon = 0.2$. *c)* Data misfit for LogInv and "Joint", for both values of ϵ.

By identifying this equation with equation 2.4 and setting $\mathbf{x_p} = 0$ we obtain the relation between the damping parameter and the variances

$$\epsilon^2 = \frac{\sigma_d^2}{\sigma_x^2}. \tag{4.32}$$

Thus, assuming uncorrelated and constant data and model variances the value of ϵ can be calculated. In the example a standard deviation $\sigma_d = 0.1$ K is assumed for the temperature data. Two different values are used for the a-priori standard deviation of the GSTH: $\sigma_x = 0.5$ K and $\sigma_x = 2$ K, corresponding to $\epsilon = 0.2$ and $\epsilon = 0.05$, respectively. Both algorithms yield essentially the same solution (figure 4.9). Slight differences in the data misfit are apparent for the larger value of ϵ. The reason is that in "LogInv" the Bayes criterion (equation 4.19) regularises only the amplitude of the ground surface temperature changes. Steady-state heat flux density and ground surface temperature are not regularised, in contrast to "Joint", where the dampening is applied to all parameters. This causes small differences in the solution for stronger regularisation.

In this particular case the results obtained from the two algorithms are similar. In general, this will not be the case. The most striking differences can be seen, when the underlying assumptions of "Joint" are violated, namely the homogeneous half-space assumption. Figure 4.10 demonstrates this for the case of layer of $\lambda = 2.5$ W(m K)$^{-1}$ between 200 m and 400 m depth, embedded in an otherwise more conducting medium of $\lambda = 3.3$ W(m K)$^{-1}$. The other parameters remain unchanged with respect to the previous experiment. It can be seen that the misfit of

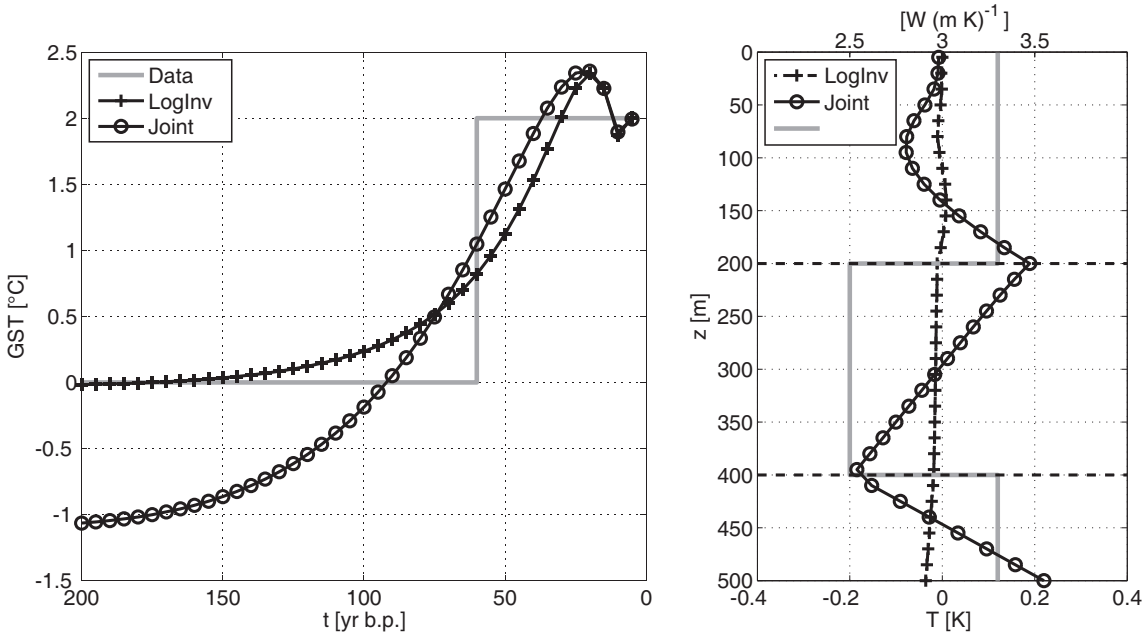

Figure 4.10: Comparison of "Joint" and "LogInv" when a layered medium is used to compute the steady-state temperature. *Left:* Input GSTH and inverted GSTH. *Right:* Data misfit of the two algorithms and thermal conductivity structure of the model.

"Joint" degrades since the anomalous conductivity section cannot be fitted. The inverted GSTH does not reproduce the temperature at early times correctly and the increase occurs too late.

4.3.5 Comparison with "ELANPlus™"

In the special case when no regularisation and no temperature data are used the algorithm should yield results similar to those from commercially available software. The program ELANPlus™ [*Anonymous*, 1999] is used for this purpose[11]. The test data set is from a borehole in the Molasse Basin in Southern Germany and consists of a 20 m long section from the Baustein beds. This is a tertiary sandstone layer with interspersed bands of marlstones. Available wireline data comprises acoustic slowness, bulk density, and spectral γ-ray. From the spectral γ-ray, the summed γ-ray and the potassium concentration are used. Data are assumed to be uncorrelated with variances of 5 $(\mu s\,m^{-1})^2$ for acoustic slowness, 0.001 $(kg\,m^{-3})^2$ for density, 5 $(API)^2$ for total γ-radiation, and 0.01 $(\%)^2$ for potassium concentration. The lithologic model comprises quartz, calcite, illite, and water. The mineral log responses are taken from table 3.5. For water, a density of 1000 $kg\,m^{-3}$, a slowness of 620 $\mu s\,m^{-1}$, and zero values for γ-radiation and potassium concentration were used.

Both algorithms compare well and yield generally the same volumetrics for this test case (figure 4.11). The discrepancies between the synthetic data of the two algorithms and the measured data is due to data errors that cannot be modelled. A particular inconsistency is seen at a depth of $x = 16$ m, where no model can be found that is able to satisfy the data. The way this and other

[11] See also section 3.4.2 for an application of this program.

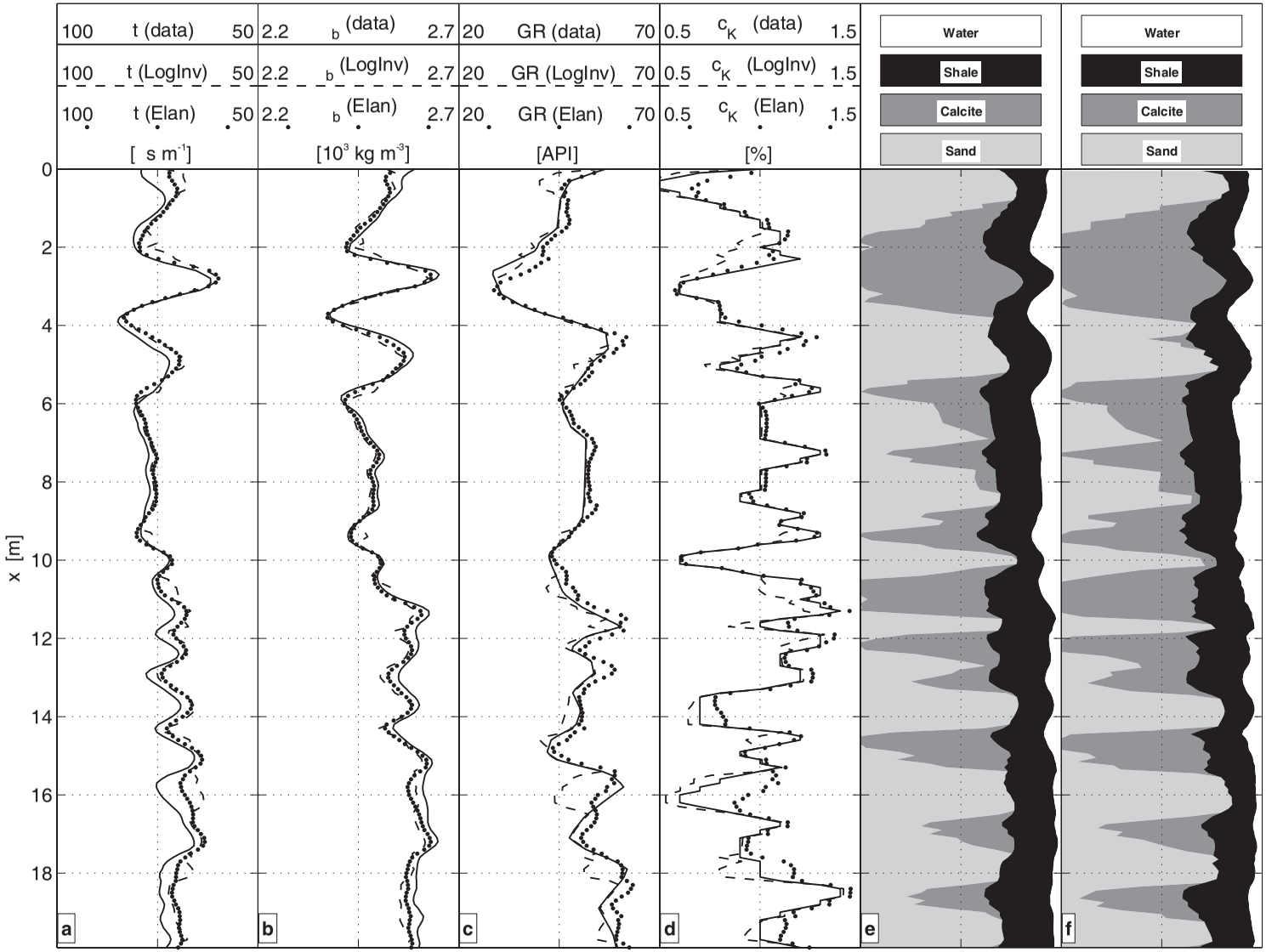

Figure 4.11: Comparison of LogInv with ELANPlus™. *a) – d)* Data (Solid line); ELANPlus™ solution (Dotted line); LogInv solution (Dashed line). *e)* Volumetric composition, ELANPlus™. *f)* Volumetric composition, LogInv. Δt: Acoustic slowness; ρ_b: Bulk density; GR: total γ-radiation; c_K: Potassium concentration.

Table 4.4: Zoning of geological units used in the inversion. TD is the total depth of the borehole. Also given is the number of measured data points per geological zone, using 10 m vertical resolution.

Layer Number	Layer Name	Number of data points	Top [m]	Base [m]
1	Upper Freshwater Molasse	34	0	450
2	Upper Marine Molasse	25	450	700
3	Lower Freshwater Molasse	40	700	1103
4	Lower Freshwater Molasse (salty)	43	1103	1525
5	Upper Jurassic	41	1525	1943
6	Middle Jurassic	1	1943	2100 TD

inconsistencies are handled by the two algorithms is different due to different ways of accounting for noise: ELANPlus™ uses empirical weighting factors for assigning relative importance in the inversion. These would have to be adjusted to obtain the best possible agreement between the two algorithms. The inconsistencies might be due to measurement noise or problems of the wireline tool, but also due to unidentified and thus unaccounted volume fractions.

4.4 Case studies

4.4.1 Inversion of borehole data from the Molasse Basin

The algorithm is tested on a data set from the western part of the German Molasse Basin in Southern Germany (see figures C.1 and C.2 for location details). This hydrocarbon exploration well has a total depth of 2000 m and was drilled through a Tertiary Flysch sequence of about 1500 m, followed by about 450 m of Upper Jurassic limestones and 50 m of Middle Jurassic shales (figure 4.12). In addition to the conventional wireline logging (sonic, γ-ray, spontaneous potential (SP), and Dual-Laterolog resistivity), a high resolution temperature log was recorded by the Leibniz Institute for Applied Geoscience, Hannover, in 1989. The log was recorded several years after shut in of the well. The useful part starts from below the water level at 100 m in the Tertiary down to 1956 m in the Middle Jurassic. These values determine the depth range of the inversion procedure. The used model has the following features:

- Six zones are defined to capture the varying petrophysical properties (table 4.4). Mostly, the zones coincide with geological boundaries; an exception being the subdivision of the Lower Freshwater Molasse for reasons discussed later in the text.

- The shallow Tertiary sequence is unconsolidated, thus reducing data quality and partly invalidating the empirical relationships. This affects primarily the sonic log. Usually a constant empirical correction is applied to the slowness derived by Wyllie's law [e.g. *Anonymous*, 1989]. Here, the correction 3.22 is used, with the overburden pressure estimated from slowness values [*Bellotti et al.*, 1979].

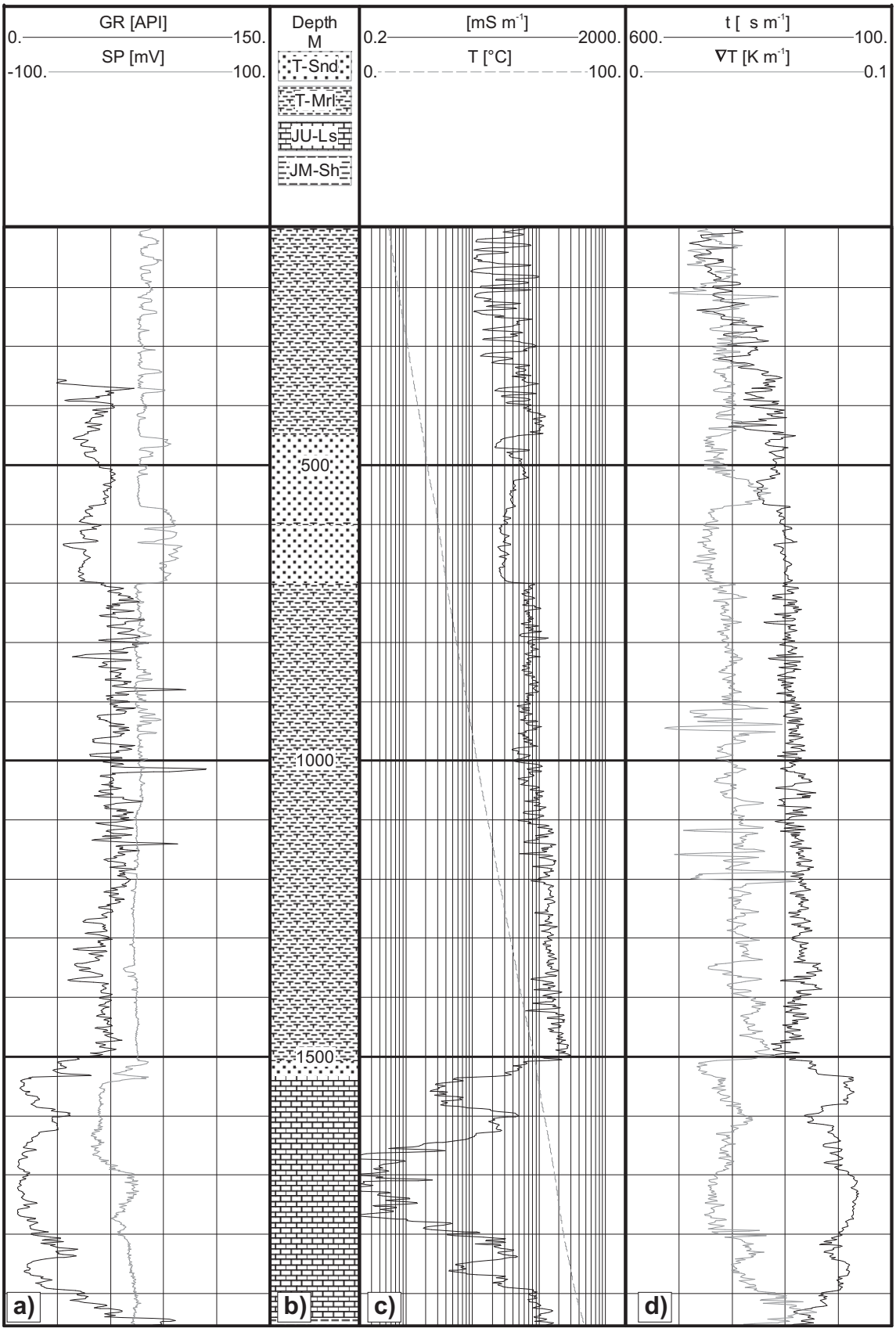

Figure 4.12: Composite log, 100 m to 1960 m, scale 1:10 000. *a) GR*: Natural γ-radiation; SP: Spontaneous potential. *b)* Composition; T-Snd: Tertiary Sandstone; T-Mrl: Tertiary Marl; JU-Ls: Upper Jurassic Limestone; JM-Sh: Middle Jurassic Shale. *c)* T: Temperature; σ: Conductivity. *d)* Δt: Acoustic slowness; ∇T: Vertical temperature gradient.

- Thermal conductivity of shale is not well constrained. As a rule of thumb, a value of 2 W(m K)$^{-1}$ is often assigned to shales. However, in many cases this approximation does not hold. For instance, a study of clay thermal conductivities in Denmark found a systematic increase of anisotropy with depth [*Waples and Tirsgaard*, 2002]. This was interpreted as a progressing orientation of clay minerals with increasing overburden pressure. Whereas shallow samples had values of thermal conductivity and anisotropy of about 2.5 W(m K)$^{-1}$ and 1, respectively, samples at depth had vertical thermal conductivities of about 1 W(m K)$^{-1}$ with anisotropy factors of around 2. The Opalinus clay, a clay sequence in the Middle Jurassic of Southern Germany and Switzerland was characterised by *Mügler et al.* [2006] using numerical modelling. They found thermal conductivity values of 1.1 W(m K)$^{-1}$ perpendicular and 1.9 W(m K)$^{-1}$ parallel to the bedding, consistent with the results of *Waples and Tirsgaard* [2002]. In the case studied here, layering is nearly horizontal, making the vertical component of λ most important. For the Tertiary shales, one has to expect much higher values for λ than for the Mesozoic ones. For this reason, shale thermal conductivity is inverted for, with a-priori values based on those quoted above.

- Similar uncertainties are associated with conductivity and sonic velocity of shale. These are also inverted for, using an a-priori variance reflecting the available information about these parameters.

- For resistivity interpretation, only the deep and shallow laterolog LLD and LLS are available. Most of the profile shows negligible separation between the two curves, indicating very little invasion. Thus LLD is assumed to be equal to the true formation resistivity.

- Formation water resistivity R_w is taken to be similar to fresh water down to 1103 m. Below this depth brine is assumed (see table 4.4). This is in accordance with findings of a well known freshwater/brine boundary within the Lower Freshwater Molasse [*Lemcke and Tunn*, 1956]. This transition can also be observed in the studied well. At approximately 1100 m depth (figure 4.12) the spontaneous potential curve deviates from the base line in the opposite direction than above that depth, indicating that R_w is smaller than borehole mud resistivity R_m below this depth [e.g. *Hearst et al.*, 2000]. Thus, water resistivity is used as an inverse parameter. Water saturation is assumed to be equal to one everywhere because the hydrocarbon bearing zone is only about 20 m thick.

- Data are reduced to 10 m sampling rate to reduce noise and improve computational efficiency.

In total, three different runs are discussed with a summary of a-posteriori parameters and variances given in table 4.5. The petrophysical a-priori parameters are the same for all models, only the prior values and variances for the GSTH are varied. The first run keeps the GSTH constant, i.e. no change relative to today. The second run identifies the GSTH with the curve derived from the analysis of the KTB temperature log (see section 4.4). These inversions serve to study the influence of transient temperature on the petrophysical inversion. For a third model, the GSTH is also inverted using a constant zero °C prior value and a standard deviation of 10 K.

Table 4.5: Summary of inversion results for the three models discussed in the text. Zone numbering corresponds to the definition given in table 4.4. *std* denotes a-posteriori standard deviation of the model parameters.

Name		Model 1 Null GTH						Model 2 KTB GTH						Model 3 GTH INV					
normalised *RMS* error		1.21						1.16						1.08					
heat flux density		(116 ± 5.7) mW m^{-2}						(120 ± 5.7) mW m^{-2}						(115 ± 5.8) mW m^{-2}					
Ground surface temperature		(7.1 ± 1.0) °C						(7.1 ± 1.1) °C						(6.2 ± 1.1) °C					
Zones		1	2	3	4	5	6	1	2	3	4	5	6	1	2	3	4	5	6
Zoned inversion parameters																			
λ_{shale}	[W (m K)$^{-1}$]	2.38	2.24	2.32	2.09	0.33	1.45	2.33	2.22	2.24	2.08	0.39	1.41	2.35	2.23	2.29	2.09	0.34	1.43
std		0.09	0.1	0.08	0.08	0.04	0.47	0.09	0.1	0.08	0.08	0.05	0.47	0.1	0.1	0.08	0.08	0.05	0.47
$v_{p,shale}$	[m s^{-1}]	2061	2697	2669	3081	2853	3361	2149	2798	2772	3102	2852	3365	2098	2743	2710	3095	2855	3363
std		69	155	71	93	149	228	73	160	76	95	149	228	74	159	75	95	149	228
σ_{shale}	[mS m^{-1}]	75	97	135	228	189	174	70	93	134	225	190	174	71	95	134	226	190	174
std		1.1	1.1	1.0	1.0	1.1	1.3	1.1	1.1	1.0	1.0	1.1	1.3	1.07	1.05	1.03	1	1.06	1.26
σ_{water}	[mS m^{-1}]	15	71	84	2854	329	2003	14	70	85	2874	345	2003	62	71	84	2910	314	2003
std		1.5	1.6	1.6	1.3	1.4	1.6	1.5	1.6	1.6	1.3	1.4	1.6	1.58	1.58	1.58	1.27	1.4	1.58
Average volumes per zone																			
Shale	[%]	43.5	34.3	52.3	46.5	8.1	25.0	45.6	35.8	52.7	46.5	8.1	25.0	44.0	35.0	52.5	46.5	8.1	25.0
std		8.7	8.4	6.1	7.7	9.6	25.7	9.3	8.0	6.3	7.7	9.6	25.7	10.1	8.2	6.2	7.7	9.6	25.7
Calcite	[%]	30.3	14.1	37.7	40.9	85.7	25.0	35.2	20.4	37.1	40.8	85.6	25.0	34.6	17.0	37.5	40.8	85.6	25.0
std		15.7	10.2	6.0	6.3	12.2	25.7	14.2	10.1	5.7	6.1	12.1	25.7	13.1	10.1	5.8	6.3	12.2	25.7
Quartz	[%]	20.3	39.7	8.3	6.8	2.6	25.0	12.8	31.2	7.4	6.7	2.6	25.0	14.9	35.9	7.9	6.8	2.6	25.0
std		15.4	17.1	3.5	4.1	4.5	25.7	13.7	16.0	2.9	4.0	4.4	25.7	13.0	16.8	3.1	4.1	4.5	25.7
Water	[%]	5.9	11.9	1.8	5.8	3.6	25.0	6.3	12.6	2.8	6.0	3.6	25.0	6.4	12.2	2.1	5.9	3.6	25.0
std		5.7	2.0	2.1	3.1	2.8	25.7	5.6	2.0	2.3	3.0	2.8	25.7	6.5	2.0	2.2	3.0	2.8	25.7

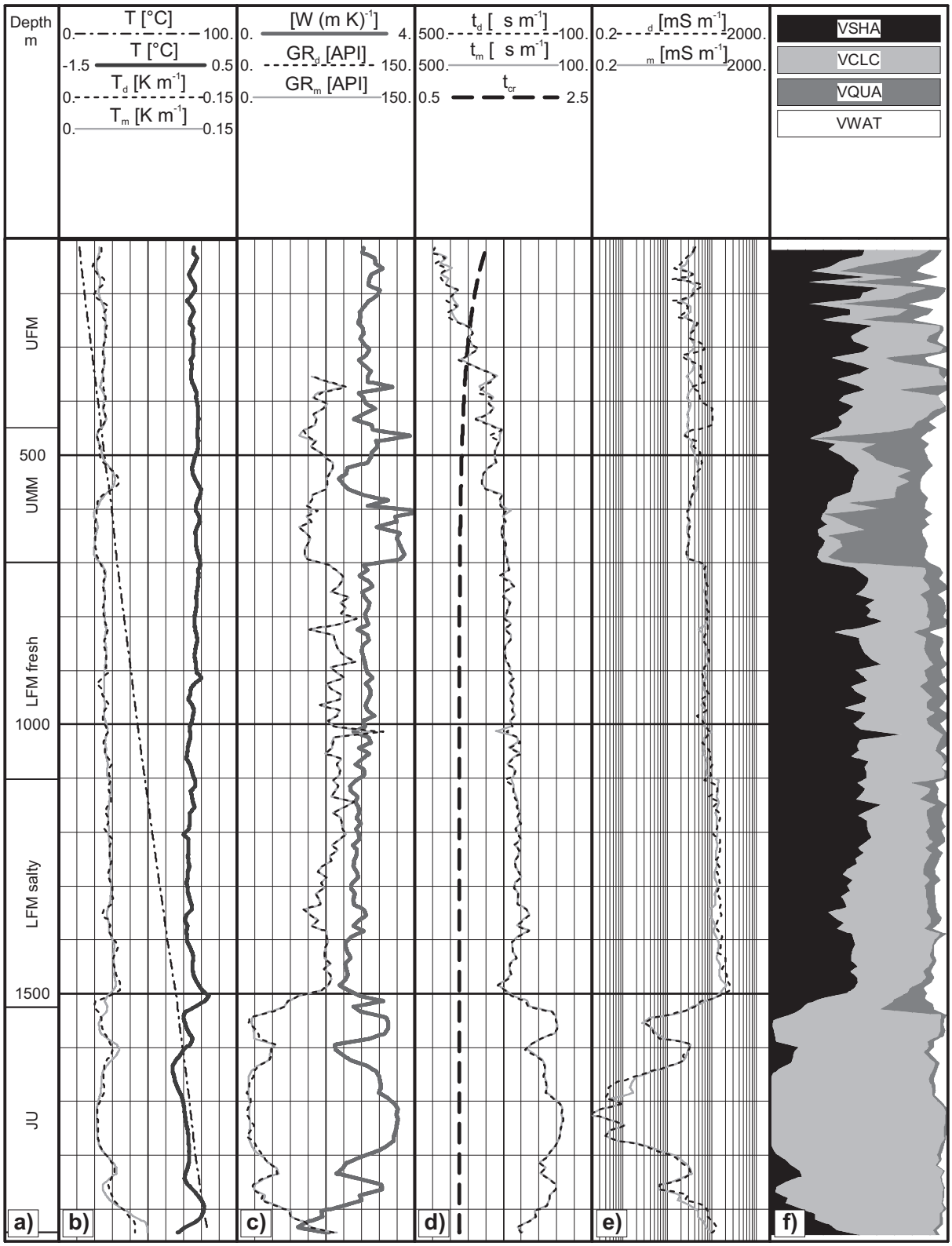

Figure 4.13: Inversion results for model 3. Indices d and m denote data and model, respectively. *a)* Zones according to table 4.4. *b)* T: Temperature; ΔT: Temperature difference between model and data; ∇T: Temperature gradient. *c)* λ: Thermal conductivity; GR: γ-ray. *d)* Δt: Slowness; Δt_{cr}: Overburden pressure correction factor for Δt. *e)* σ: Conductivity. *f)* Inverted volume fractions for shale (VSHA), calcite (VCLC), quartz (VQUA), and water (VWAT).

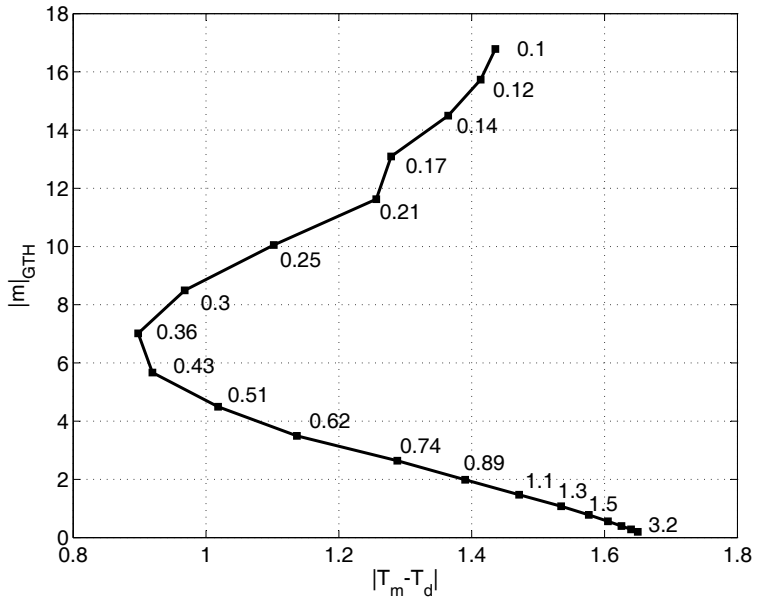

Figure 4.14: L-Curve (c.f. figure 2.2) for the inversion of the data set in figure 4.13.

An inspection of the a-posteriori petrophysical properties for all models in table 4.5 shows that the influence of the transient part of the temperature on the petrophysics is negligible. Compositional differences between the two models are generally below 10 %. This indicates that consideration of the transient part of the temperature profile is unnecessary if one is interested only in the inversion of petrophysical properties. However, this also depends on the depth range and on the strength of the paleoclimatic signal. Figure 4.13 shows data and model prediction for model 3. In general, there is good agreement, with some minor exceptions in zones 3 to 6. Zone 1 has a degraded fit and also shows unrealistic variations in the lithology column. This is a result of the lack of a Gamma-Ray log for the shallow part and some large fluctuations of the resistivity-curve. Hence, data quality is poor and results are partly inconsistent and unreliable for shallow depths. The temperature misfit is generally below 0.1 K. This is better than what could be obtained with an assumption of a homogeneous subsurface. See for instance *Hartmann et al.* [2001] and *Clauser et al.* [2002] for such an analysis in the Molasse Basin. It is also apparent that even small-scale variations in the logs are mostly reflected in the temperature gradient data, thus providing further confidence in the use of this approach.

Model 3 requires selecting an appropriate regularisation parameter for the GSTH. An L-curve is computed as described in section 2 (figure 4.14), resulting in an unexpected shape. For small values of the regularisation parameter the data misfit increases again. The reason for this behaviour is not entirely clear, but it can be assumed that it is due to stability problems of the nonlinear inversion when ϵ is small. This behaviour was also observed by other researchers working on nonlinear inversion of GSTH from temperature data[12]. Nevertheless, the lower part

[12]personal communication by Dr. V. Rath, RWTH Aachen.

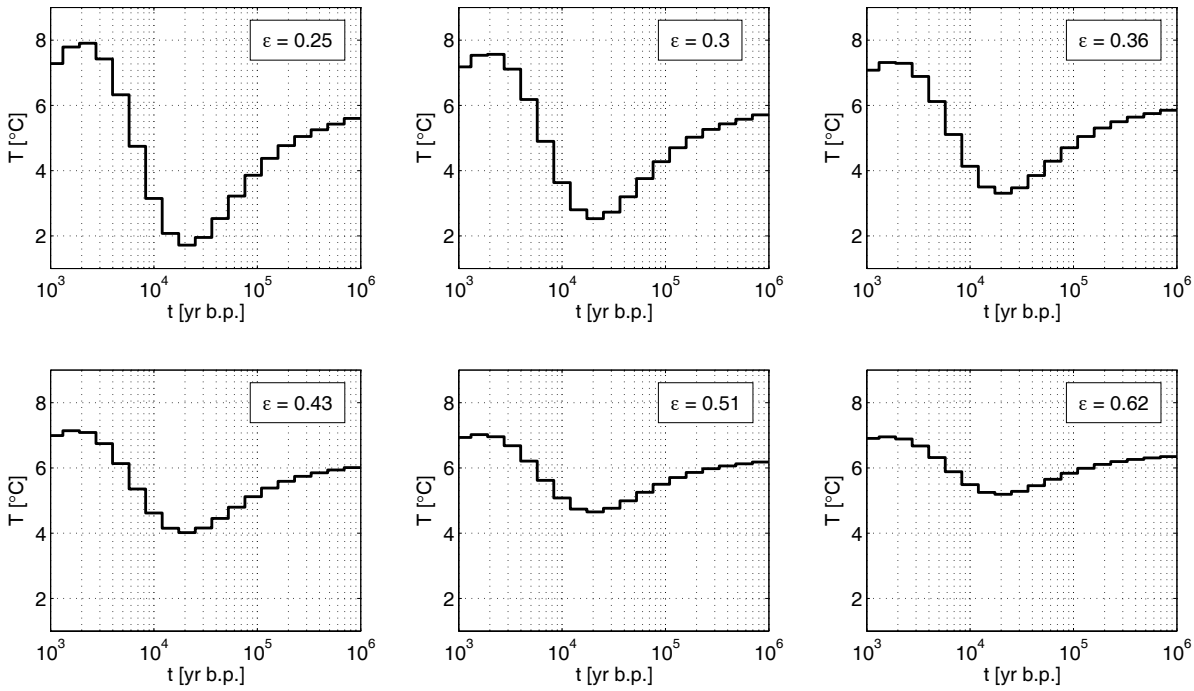

Figure 4.15: GST histories inverted from the data set in figure 4.13 for different values of the regularisation parameter ϵ. (Optimum: $\epsilon \approx 0.4$.)

of the L-curve appears to be useful and suggests an optimum value of about 0.4.

Ground surface temperature histories corresponding to different values of ϵ are shown in figure 4.15 and can be compared to those from the KTB (figure 2.18). The main feature to note is that the GSTH during the last ice-age for the Molasse log depends strongly on the regularisation, in contrast to the GSTH derived from the KTB temperature log. It needs to be remembered that the Molasse log has a depth of less than 2000 m and thus the discussion on insufficient log depth in section 2.4.1 applies. The modelled paleoclimatic variation has to be appreciated against this background. A temperature decrease of about 3 °C for the last glacial can be inferred from the data. This can be considered a minimum estimate of the actual temperature variation. Consistent with this consideration is also the observation that the maximum GST following the glacial is reached only at 2000 years before present. This shift is also observed on the synthetic data sets discussed in chapter 2.

In the Molasse region the task of paleoclimatic reconstruction is further complicated by the fact that part of the area was glaciated in the last ice-age. It is known that the temperature at the base of glaciers often is around 0 °C. Thus the subsurface is insulated from the air temperature and does not record the full temperature variation. It would be highly desirable to record a temperature log in the Molasse area sufficiently deep to obtain a robust estimate of the surface temperature during the last glaciation. However, up to now no such data exists.

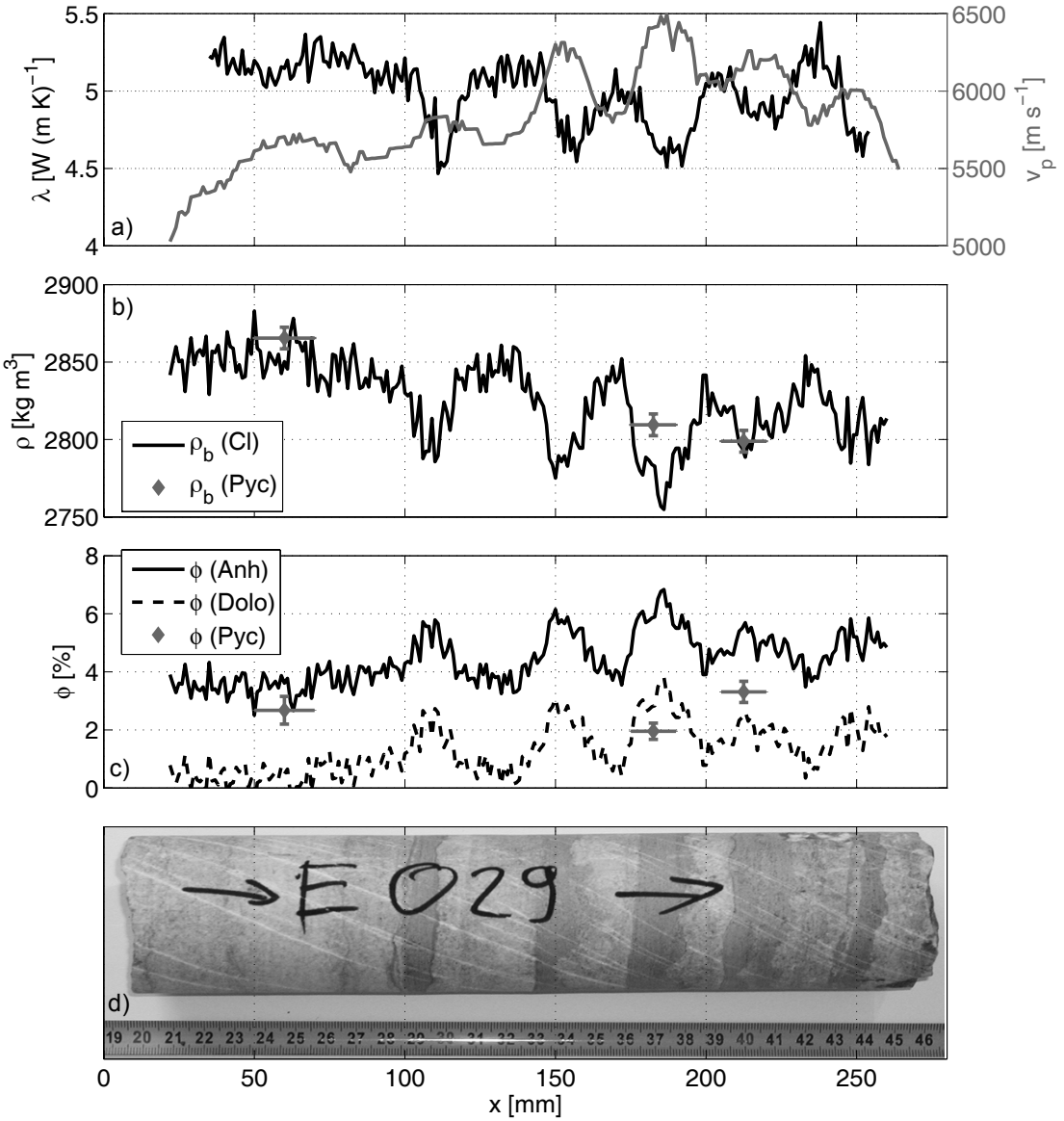

Figure 4.16: Measurements taken on a layered anhydrite/dolomite sample. *a)* Thermal conductivity (black) and sonic velocity (grey). *b)* bulk density from core-logger (Cl) measurements of γ absorption (black) and measured by a powder pycnometer (Pyc, grey); Error bars of the pycnometer measurements show standard deviations and positional uncertainty of the plugs. *c)* γ porosity assuming anhydrite (solid black) and dolomite (dashed black) as the matrix compared to pycnometer derived porosity. *d)* Core photograph showing the layering. Bright bands consist mainly of anhydrite, dark bands are composed mainly of dolomite. Arrows denote downward direction in the borehole.

4.4.2 Characterising laboratory samples by high resolution core scanning

The following will illustrate the use of the algorithm by considering the analysis of laboratory measurements taken on a core sample that shows clearly visible variations of physical properties.

Table 4.6: Results of the mineralogical analysis and pycnometer measurements on samples taken from the core. Position X of the plugs along the axis in figure 4.16, volume fractions of various minerals, matrix density $\rho_{m,c}$ computed from the mineral composition and density values in table 3.5, Matrix density ρ_m and porosity ϕ from pycnometer measurements.

	X [mm]	Quartz [wt %]	Anhydrite [wt %]	Dolomite [wt %]	Kaolinite [wt %]	Ankerite [wt %]	$\rho_{m,c}$ [kg m^{-3}]	ρ_m [kg m^{-3}]	ϕ [%]
Plug 1	60	0.52	89.84	2.44	5.62	1.58	2942	2944	2.7
Plug 2	175							2866	2.0
Plug 3	215	3.09	43.92	48.83	4.16		2896	2895	3.3

The core serves as a good example to illustrate the application of the algorithm because control over the quality of measurements is very good and detailed analyses are easy to perform and can be compared to the actual geology of the rock.

The core (figure 4.16, d) was drilled in a borehole in the Southern German Molasse Basin and originates from the middle Triassic period just above the boundary to the lower Triassic, encountered in this borehole at about 1300 m depth. The lowermost part of the middle Triassic in Southern Germany is characterised by massive anhydrite or gypsum with a thicknesses of up to 5 m. Thin layers of shaly dolomites are spread throughout this sequence. The structure corresponds to a successive evaporation sequence with temporary decrease of the salt concentration concurrent with enhanced wave action [*Geyer and Gwinner*, 1991]. This structure is reflected in the sample with its dark bands of dolomite embedded in the brighter anhydrite.

To analyse the sample, thermal conductivity, sonic velocity, and bulk density were measured on the dry sample along the core axis (figure 4.16, a-b). In addition, matrix density and bulk density were determined on three plugs using a pycnometer (figure 4.16, b,c). The porosity is computed along the core from the γ-density measurement using the arithmetic mean (equation 3.6). Pure dolomite (ρ_e = 2870 kg m^{-3}) and pure anhydrite (ρ_e = 2960 kg m^{-3}) are assumed as matrix material. These profiles can be compared to the pycnometer derived porosity (figure 4.16, c). The discrepancy implies that a mixture of the minerals occurs in the sample. This is confirmed by a mineralogical analysis of two plugs (table 4.6). The bright bands are composed mainly of anhydrite whereas the dark bands contain a mixture of both dolomite and anhydrite.

The mineralogical analysis yields valuable information about the occurrence of the minerals. Using the information on the occurring minerals, a modified M-N plot [*Burke et al.*, 1969] can be constructed. The original method uses sonic, neutron porosity, and density logs to compute two parameters M and N that are independent of porosity and can be used to identify the occurring minerals. Because neutron porosity is not available for the sample, a parameter O is defined instead that uses the logarithm of the thermal conductivity in the same manner. In metric units

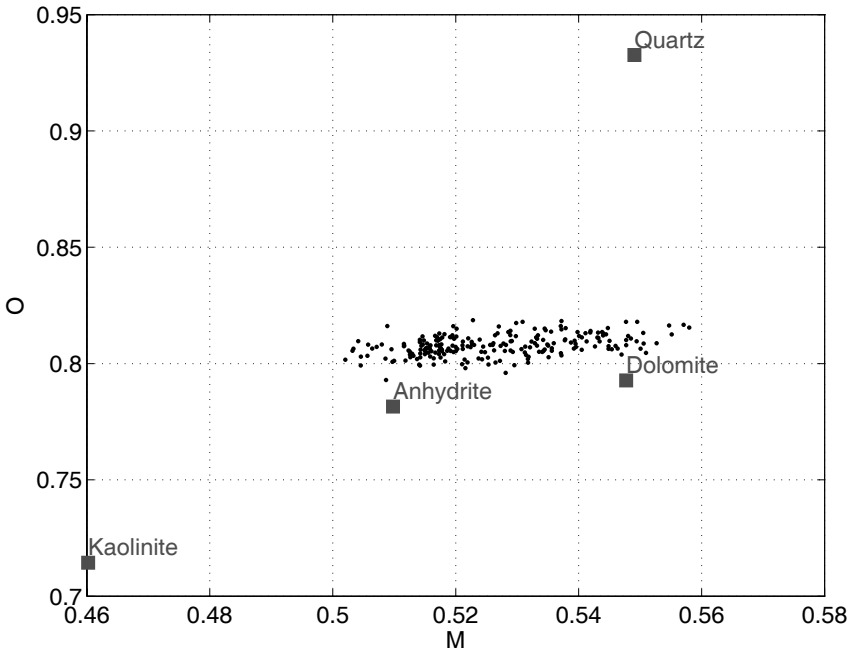

Figure 4.17: M-O plot of the analysed sample. Black dots denote data computed from the measurements on the sample. Gray squares mark expected points for pure minerals. All mineral properties required to compute M and O are taken from table 3.5 except for Kaolinite, where a thermal conductivity of 2 W(m K)$^{-1}$ was assumed.

(µs m^{-1}, kg m^{-3}, W(m K)$^{-1}$) the equations are given by

$$M = 3.28 \cdot \frac{\Delta t_f - \Delta t}{\rho_b - \rho_{b,f}}, \tag{4.33}$$

$$N = \frac{\phi_{n,f} - \phi_n}{\rho_b - \rho_{b,f}}, \tag{4.34}$$

$$O = \frac{\log_{10}\lambda - \log_{10}\lambda_f}{\rho_b - \rho_{b,f}}, \tag{4.35}$$

where Δt, ρ_b, ϕ_n, and λ are measured values of acoustic slowness, bulk density, neutron porosity, and thermal conductivity, respectively. The subscript f denotes the corresponding fluid properties. The parameter O is plotted versus M for the sample in figure 4.17 together with the expected (M, O)-pairs for the minerals given in table 4.6. Data for the mineral ankerite is sparse. It is a mineral chemically and structurally similar to dolomite in which Magnesium is replaced largely by iron causing a higher density of 3000 kg m^{-3} to 3100 kg m^{-3}. In the following analysis ankerite will be added to the volume fraction of dolomite because of its small volume fraction and similarity to dolomite. The physical properties of the other minerals are taken from table 3.5. The value of thermal conductivity of Kaolinite is assumed to be 2.0 W(m K)$^{-1}$, an assumption commonly made for clay minerals [*Brigaud and Vasseur*, 1989]. However, one has to keep in mind the considerable uncertainty of this value that was already discussed in the previous section. The plot shows that the measurements are consistent in a qualitative manner with a mixture

composed primarily of anhydrite and dolomite. However, the M-O plot suggests large amounts of dolomite for some measurements, whereas the mineralogical results imply that the grey bands contain only about 50 % dolomite. Further, for the position of the first plug (50 mm to 70 mm) in figure 4.16 the mean thermal conductivity is about 5.2 $\mathrm{W(m\,K)^{-1}}$. Given a matrix value of about 5.1 $\mathrm{W(m\,K)^{-1}}$ estimated from the mineralogical results and a porosity of 3 % one would expect a much lower thermal conductivity of about 4.4 $\mathrm{W(m\,K)^{-1}}$ for the dry sample. There are two possible reasons for these discrepancies: (1) Equations 4.33 to 4.35 imply particular mixing laws for sonic velocity and thermal conductivity, the arithmetic travel time average (equation 3.6) and the geometric mean (3.10). These might not hold true for low porosity chemical sediments. (2) The value used for the mineral thermal conductivity might be too low. For instance, *Brigaud and Vasseur* [1989] found considerably higher values than those given in table 3.5.

Both effects act to increase the uncertainty about the mineral points in figure 4.17. To address these two issues, the inverse method presented here can be used. (1) Uncertainty about the mixing law can be incorporated by using a general mixing law for thermal conductivity that accounts for structural effects. The model of *Korvin* [1978], already presented in section 3.2, is used. The model can be applied to both, thermal conductivity and sonic velocity. Special cases can be compared to empirical relationships. (2) Uncertainty about mineral properties is incorporated by including them as inversion parameters and assigning them a-priori variances. It is assumed in the model that the mineral properties are constant along the core.

The inverse model was set up as follows: It comprises five volume fractions with a-priori values and standard deviations derived from their variability in the chemical analysis: Quartz (0.02 ± 0.01), anhydrite (0.5 ± 1.0), dolomite (0.5 ± 1.0), kaolinite (0.05 ± 0.01), and air filling the pore space (0.026 ± 0.02). As stated before, the mineral ankerite is added to the dolomite fraction. Values for mineral physical properties are taken from table 3.5. The data are assumed to be uncorrelated with standard deviations of the measurements of 0.05 $\mathrm{W(m\,K)^{-1}}$ for thermal conductivity, 50 $\mathrm{m\,s^{-1}}$ for sonic velocity, and 5 $\mathrm{kg\,m^{-3}}$ for density.

A set of different models where used to test several hypotheses. Results are summarised in table 4.7 and figure 4.18. The simplest model (number 1, figure 4.18 top) employs the geometric mixing law for thermal conductivity and the time-average formula for sonic velocity. It can be considered a benchmark as it is close to the conventional analysis shown in the M-O plot. It yields an unsatisfactory fit with an RMS-error of about 2.3. This result confirms the impression from the M-O plot that the model is inconsistent with the data. No single volumetric composition within this model can fit all measurements: Figure 4.18 (top) shows a large misfit for density and thermal conductivity, particularly for the high anhydrite contents.

To refine the model, the t$^{\text{th}}$-order mean model is introduced with $t = (0 \pm 0.1)$ for thermal conductivity and $t = (-1 \pm 0.1)$ for sonic velocity as a-priori values. This corresponds to the geometric mixing law ($t = 0$) and the travel time average ($t = -1$)[13]. To test whether a single parameter t can be used to explain the data, two models are designed, one with a single t and one with two independent t-values for thermal conductivity and sonic velocity.

The best fit values for t are in the range of 0.8 to 1.0 if the mineral properties are fixed at their

[13]Wyllie's travel time average is the arithmetic mean for slowness ($t = 1$), in terms of velocity it is the harmonic mean ($t = -1$).

Table 4.7: Summary of the results and parameters for the inversion runs for the sample. The data column presents measured values. These are compared to inverted parameters for models 1 to 6. See text for a more detailed discussion of the results.

		Data	Model 1	Model 2	Model 3	Model 4	Model 5	Model 6
v_p model			Wyllie	joint tth order mean	single tth order mean	Wyllie	joint tth order mean	single tth order mean
λ model			geometric		single tth order mean	geometric		single tth order mean
normalised *RMS* error			2.29	1.96	1.95	1.62	0.85	0.86
t_λ			N/A	0.99 ± 0.38	0.97 ± 0.38	N/A	0.90 ± 0.37	0.62 ± 0.36
t_{vp}					0.80 ± 0.36			0.89 ± 0.38
Plug 1 volumes [%]	$V_{\text{anhydrite}}$	89.8	86.3	88.5	88.5	85.9	87.2	87.1
	V_{dolomite}	4.0	7.1	4.5	4.7	6.7	3.8	3.8
	$V_{\text{kaolinite}}$	5.6	4.6	2.8	2.8	5.4	4.8	4.9
	ϕ	2.7	0.3	2.4	2.4	0.3	2.6	2.6
Plug 3 volumes [%]	$V_{\text{anhydrite}}$	43.9	43.8	44.1	44.0	42.9	43.0	43.1
	V_{dolomite}	48.8	48.8	48.7	48.8	48.3	48.2	48.1
	$V_{\text{kaolinite}}$	4.2	5.6	2.8	2.8	7.0	4.4	4.4
	ϕ	3.3	0.1	2.7	2.7	0.1	2.8	2.8
Mean volumes [%]	$V_{\text{anhydrite}}$		39.0	64.3	62.8	16.9	58.0	58.5
	V_{dolomite}		55.6	29.0	30.7	76.0	33.0	32.4
	$V_{\text{kaolinite}}$		3.1	2.1	2.1	4.7	4.7	4.7
	ϕ		0.5	2.8	2.7	0.7	2.7	2.7
Mean sample values	λ	4.99	4.84	4.77	4.77	5.04	4.98	4.99
	v_p	5864	5869	5875	5869	5802	5853	5843
	ρ_b	2826	2875	2835	2836	2846	2827	2827
Estimated mineral values	$\lambda_{\text{anhydrite}}$					6.20 ± 0.22	6.03 ± 0.17	6.12 ± 0.20
	$\lambda_{\text{dolomite}}$					5.97 ± 0.20	5.31 ± 0.14	5.38 ± 0.20
	$\lambda_{\text{kaolinite}}$					0.29 ± 0.20	1.21 ± 0.28	1.23 ± 0.28

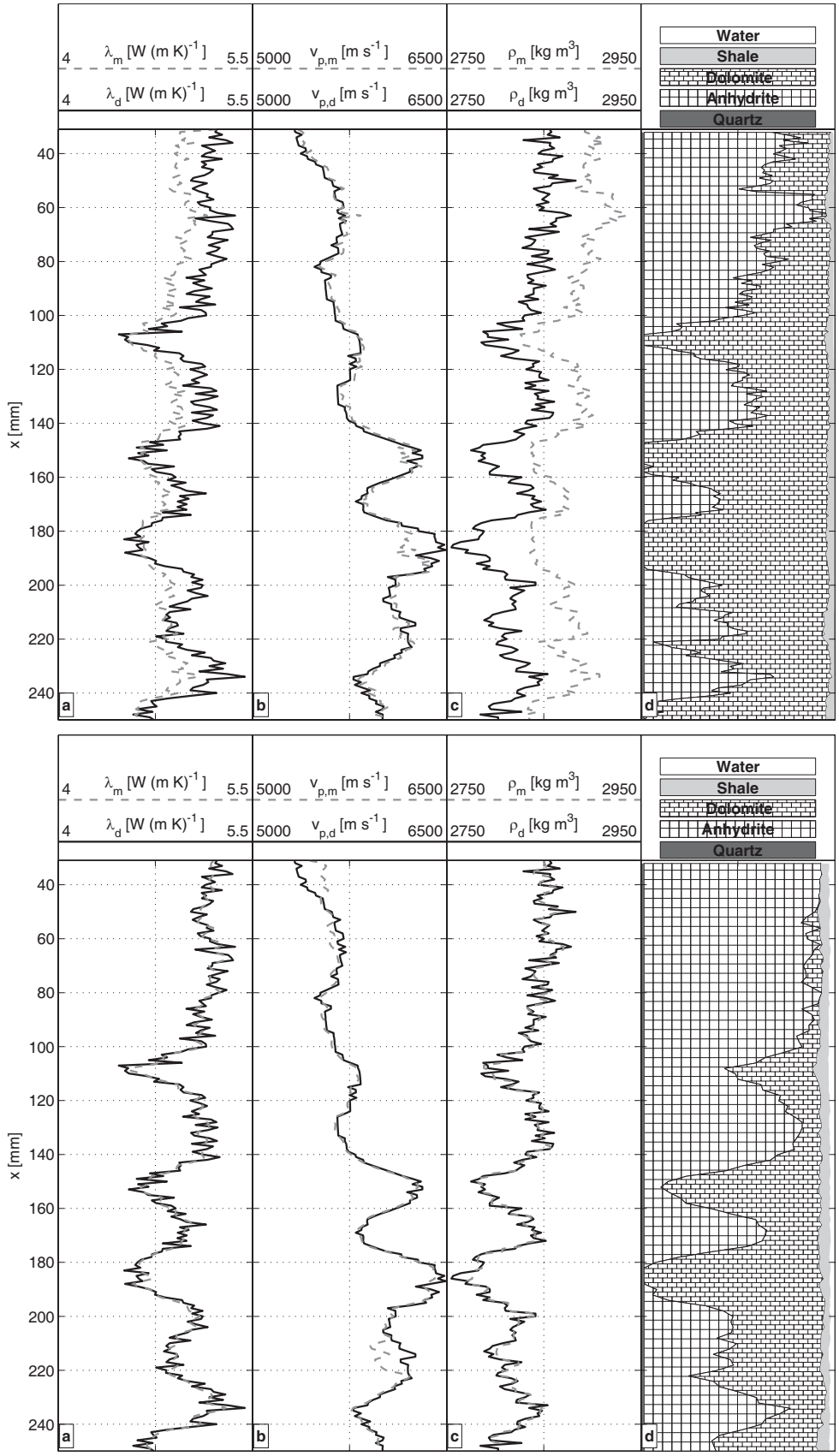

Figure 4.18: Results of the inversion of high resolution measurements for the anhydrite/dolomite sample. *Top:* Results for model 1. *Bottom:* Results for model 6. *a) – c)* Measured data (subscript d) and modelled values (subscript m) for thermal conductivity λ, sonic velocity v_p, and bulk density ρ_b. *d)* Modelled mineral composition of the sample.

original values. This is a strong indicator for the invalidity of the standard mixing laws when such well lithified chemical sediments are considered. The models show slightly different values for t if separate values are used for v_p and λ but they are almost equal when considering the error bounds. Compare this also to the aspect ratios derived in chapter 3 for sandstones with values of $\alpha \approx 0.01$, corresponding to values of $t \approx -0.6$ (see figure 3.3) for the thermal conductivity. The difference between the two t-values indicates large petrophysical differences between the sandstones studied in chapter 3 and the chemical sediments analysed here.

The misfit is improved to lower RMS-errors of about 1.95 by models 2 and 3. But the fit is still inconsistent with the data, showing that uncertainties about the mixing law cannot explain alone the inconsistency. Therefore, the same set of models is modified in models 4 to 6 to include mineral thermal conductivities in the inversion. Thermal conductivity values of the minerals are assigned a-priori standard deviations of 0.1 W(m K)$^{-1}$. To reduce the ambiguity of the inversion only anhydrite, dolomite, and kaolinite are included as mineral components.

The inversion results using these models are shown in table 4.7. Use of the geometric and Wyllie average (model 4) yields an improved but still high RMS-value of 1.62. In addition, the thermal conductivity value for kaolinite is unrealistically low. The situation is improved when the general mixing law is used. Figure 4.18 shows the results for model 6. The RMS-error is below one, indicating a slight overfitting of the data. The values for t are more strongly separated than for model 3 with $t = 0.6$ for thermal conductivity and $t = 0.9$ for sonic velocity. Note that the value of 0.6 is close to 0.5 which corresponds to the square root average (equation 3.11). It can also be noted that an inverse correlation exists between the value of t and the matrix thermal conductivities for models 4 to 6 [14]. The mineral thermal conductivities are rather high for anhydrite and dolomite, but still plausible considering that the values given in table 3.5 are mostly based on natural rock samples [*Clauser*, 2006; *Diment and Pratt*, 1988; *Robertson*, 1988]. Impurities and a small but significant porosity of these samples result in a range of values often larger than 10 % [*Diment and Pratt*, 1988]. In addition, values measured on rock samples can be systematically lower than those for single crystals [*Robertson*, 1988]. Since porosity is taken into account explicitly in the inversion approach presented here, it is to be expected that the derived mineral values should be higher than values based on measurements on rock samples. This is confirmed by *Brigaud and Vasseur* [1989], who report similarly high values based on an inversion method (Dolomite: 5.0 W(m K)$^{-1}$ to 5.3 W(m K)$^{-1}$; Anhydrite: 6.0 W(m K)$^{-1}$ to 6.3 W(m K)$^{-1}$). The clay mineral value is quite low. It is most strongly affected by the choice of model and, due to its low content, the least trustworthy.

The question if the same mixing law is applicable for both thermal conductivity and sonic velocity cannot be answered conclusively. Both, thermal conductivity and sonic velocity apparently react in the same manner, i.e. an increase in t for the change from granular, high-porosity to chemical, low-porosity sediments. The increase in t seems to be stronger for sonic velocity (-1 to 0.9) than for thermal conductivity (0 to 0.6). However, because t decreases when mineral properties are inverted for, it cannot be ruled out that the high t-value for v_p in model 6 derives from underestimated v_p-values of the minerals rather than the structure of the sample. The number of independent measurements was unfortunately not large enough to include the sonic properties in

[14] Recall that the geometric mixing law (model 4) corresponds to $t = 0$.

the inversion as well.

4.5 Conclusions

This chapter describes the development and application of the modular inversion algorithm "LogInv" for well log and petrophysical analysis. It features a general, common interface for wireline logging and petrophysical problems. The program allows modification of the forward model without changing the inverse code. The petrophysical models and the temperature model were tested using benchmark models. There is good agreement confirming correctness of the models and inversion procedure applied. The remaining differences can be explained in terms of slightly different parametrisation of the problem in the codes compared.

In contrast to conventional inversion techniques for wireline data which are mostly based on a level by level basis, the proposed algorithm can deal with more complex models including shoulder effects and global inversion parameters. In the Gauß-Newton iteration scheme this yields a large Jacobian matrix, resulting in issues of memory requirements and CPU performance. The implementation of automatic differentiation (AD) and matrix compression are two options that were considered to solve these problems. Although AD is promising, in the applications studied here it yielded no advantage over finite differences (FD). It is most effective when derivatives of strongly nonlinear functions are needed. In such a case finite differences are either inaccurate, leading to a larger number of iterations, or are computed adaptively, leading to a larger number of forward computations per FD evaluation. For the problems studied here, AD did not reduce computational expense compared to finite differences. Automated matrix compression by colouring yields mixed results. It is very effective when models with only local non-zero derivatives are considered. However, when temperature is considered, the Jacobian matrix becomes densely populated as temperature does not only depend on the current depth level but also on every level above the current depth.

The original motivation for this development — that is inclusion of temperature in the petrophysical inversion and use of petrophysical data in the transient temperature inversion — was addressed in a case study and by theoretical error analysis. It appears that the value of temperature in petrophysical inversion is comparable to that of conventional logging data. The distinguishing feature of temperature data is its non-locality. However, the assumption could not be verified that incorporation of temperature data improves results where local errors in the petrophysical data are present.

The example inversion for GSTH using the Molasse data set is consistent with what would be expected for this region and a well of restricted depth. But the results leave considerable ambiguity as to the real paleoclimatic change in surface temperature. The inversion runs for the case study with fixed GST history suggest that a transient temperature model has only minor influence on the estimated petrophysical properties. If one is interested purely in a petrophysical inversion, it seems unnecessary to include a transient model. However, this is not only caused by the fact that the transient signal is inherently weak. A larger depth coverage increases the influence of the transient signal on the petrophysical part. Another aspect is the model complexity. Part of the transient signal can be accommodated by minor variations of petrophysical properties. In

particular this is true for a zoned model such as the one considered. Here, the most influential property is the shale thermal conductivity. It is the property that varies most between inversion runs. For the different models it is adjusted by the inversion procedure to fit the temperature signal without modifying the volumetric composition significantly. This is of course not desirable, but it is a natural consequence of the poor prior information about this parameter and cannot be avoided. In conjunction with the regularisation of the GSTH amplitudes this will always yield a dampened version.

This seemingly negative quality turns out to be quite useful for studying the actual information content of a set of data. It would of course be very desirable to obtain an accurate estimate of the GST history, but the truth is that this information can only be inferred with a large error margin. A more simple model that does not use all information sources available might yield a wrong impression of the actual data quality and the possible inferences. This is also demonstrated in the second, purely petrophysical example. The different models with varying parameters and complexity constrain the range of plausible models and also highlight weaknesses in the data set. In general, these are the mineral properties of the petrophysical model. Such values are tabulated but often need to be adjusted in the analysis process to obtain a result which is consistent with the input data.

Chapter 5

Summary & Outlook

The work presented here analyses several aspects of the interpretation of well logging data, with special emphasis on temperature data. Chapter 2 analyses the sensitivity of paleoclimatic inversion with respect to several parameters. Major issues are the length of the log and the regularisation of the ill-posed problem. With respect to the petrophysical properties, errors in thermal diffusivity and heat production rate are less important than those in thermal conductivity. Errors in thermal conductivity will corrupt any paleoclimate inversion. In particular continuous variations, be they due to compaction processes or the temperature dependence of thermal conductivity, are difficult to distinguish from transient signals. In contrast, lithological changes usually cause step changes in the temperature gradient that cannot be fitted by a paleoclimatic signal. Indeed, in the examples studied here, a strong compaction effect is noted in the sonic data, both from the laboratory and the borehole (see chapters 3 and 4). A solution to this problem may be provided by the joint inversion of temperature data and a continuous record of petrophysical properties. If this is to be implemented, the feasibility of computing thermal properties from wireline data needs to be assessed.

This predictability of thermal properties, in particular thermal conductivity, based on petrophysical and wireline measurements is reviewed on a case example from the Southern German Molasse Basin in chapter 3. This serves not only as a guide to the optimal method for thermal property prediction but also as a study of the feasibility of the approach even with a less than complete data set. The mixing law method, as implemented in a commercial program, was found to be the optimum method. In addition it is the most flexible one with respect to the number and type of available input logs. Empirical relationships yield a statistical accuracy of about 0.2 $\mathrm{W(m\,K)^{-1}}$ based on laboratory data and 0.3 $\mathrm{W(m\,K)^{-1}}$ for wireline data. However, the inversion algorithm used can not deal with temperature data. For geothermal problems this is an important log with large sensitivity to thermal properties.

These requirements define the framework for an inversion algorithm presented in chapter 4. It is capable to account for global parameters, implements custom-tailored petrophysical models, and contains advanced inversion techniques. The implemented forward models and the inversion code are successfully tested against commercial software and a published algorithm. An analysis of the quality of the temperature log for petrophysics inversion in general shows that its value is comparable to other wireline data.

The application to a real-world example indicates that a number of ambiguities between thermal data and other properties exist that can influence the inference of reliable GST histories. The volumetric composition is the most robust parameter in the inversion and relatively insensitive to the transient signal superimposed on the temperature data. For the specific cases studied, it cannot be confirmed that a more accurate prediction of thermal conductivity is possible by using this inversion code. On the contrary, it was shown that certain unknowns regarding the thermophysical properties and the transient temperature signal have a strong interaction.

The prime objective of the petrophysical part of the algorithm is the integration of various empirical relationships for a joint evaluation. This flexibility is demonstrated on a second case example were high resolution continuous petrophysical measurements on a rock sample are analysed. Several models of varying complexity can be compared and evaluated. This proves very useful for interpreting structural parameters of the rock sample and possible similarities between structural parameters for different petrophysical properties. This type of analysis can be taken a step further if a single numerical rock model is used which can predict several properties at once from volumetric composition and structural parameters described in a statistical sense. A number of studies have been published that approach the forward problem [e.g. *Arns et al.*, 2002]. This type of forward model is a good candidate for inclusion in the inversion, in particular, if automatic differentiation ensures that exact derivatives are computed even for highly non-linear models. Another interesting extension lies in the use of other petrophysical models. For example, NMR measurements can be used to constrain porosity estimates from other methods and provide additional information about the structure of the sample.

Future development and routine application of the LogInv-code will require work on computational efficiency. The associated problems and approaches to their solution are analysed in this study. The main bottleneck is the inversion of the full matrix because it requires large memory and CPU time. A more efficient matrix compression might speed up the process considerably. But it is demonstrated that the effectiveness also depends on the particular petrophysical model and the way it is set up. In consequence, efficiency cannot be guaranteed and heavily depends on the user's expertise in preparing the forward model. The most promising route forward is the consequent use of automatic differentiation. With the currently available version, no significant performance increase was achieved. In the forward mode of AD, it requires a number of function evaluations on the same order of the number of model parameters. Thus, it is most efficient when the number of parameters is small, which is not the case here. Using the reverse mode, the gradient vector can be computed instead of the full Jacobian matrix. This should be possible with roughly one function evaluation. Together with a modified inversion algorithm that requires only this information, such as conjugate gradient algorithms, this may result in a major performance increase.

Bibliography

Allen, P. A., and J. R. Allen, *Basin Analysis. Principles and Applications*, Blackwell Scientific, Oxford, 1990.

Anonymous, *Log Interpretation Principles/Application*, 7th ed., Schlumberger Wireline & Testing, Sugar Land, Texas, 1989.

Anonymous, *ELANPlus Theory*, Schlumberger, Austin, Texas, 1999.

Archie, G. E., The electrical resistivity log as an aid in determining some reservoir characteristics, *Transactions of the American Institute of Mining, Metallurgical, and Petroleum Engineers*, *146*, 54–62, 1942.

Arns, C. H., M. A. Knackstedt, W. V. Pinczewski, and E. J. Garboczi, Computation of linear elastic properties from microtomographic images: Methodology and agreement between theory and experiment, *Geophysics*, *67*, 1396–1405, 2002.

Aster, R., B. Borchers, and C. Thurber, *Parameter estimation and inverse problems*, Academic Press, San Diego, 2004.

Athy, L. F., Density, porosity, and compaction of sedimentary rocks, *AAPG Bulletin*, *14*, 1–24, 1930.

Aydin, I., H. I. Karat, and A. Kocak, Curie-point depth map of Turkey, *Geophysical Journal International*, *162*, 633–640, 2005.

Bartetzko, A., P. Pezard, D. Goldberg, Y. F. Sun, and K. Becker, Volcanic stratigraphy of DSDP/ODP Hole 396A; An interpretation using well-logging data, *Marine Geophysical Researches*, *22*, 111-127, 2001.

Bartetzko, A., R. Pechnig, and J. Wohlenberg, Interpretation of well-logging data to study lateral variations in young oceanic crust: DSDP/ODP holes 504B and 896A, Costa Rica Rift, in *Geological applications of well logs: AAPG Methods in Exploration*, edited by M. Lovell and P. N., vol. 13, pp. 213-228, American Association of Petroleum Geologists, 2002.

Beardsmore, G. R., and J. P. Cull, *Crustal Heat Flow*, Cambridge University Press, 2001.

Beck, A. E., The use of thermal resistivity logs in stratigraphic correlation, *Geophysics*, *41*, 300–309, 1976.

Beck, A. E., P. Y. Shen, H. Beltrami, J.-C. Mareschal, J. Safanda, M. N. Sebagenzi, G. Vasseur, and K. Wang, A comparison of five different analyses in the interpretation of five borehole temperature data sets, in *Climatic Change Inferred from Underground Temperatures, Paleogeography, Paleoclimatology, Paleoecology (Global and Planetary Change Section)*, edited by T. J. Lewis, vol. 98, pp. 101–112, Elsevier, Amsterdam, 1992.

Bellotti, P., V. Di Lorenzo, and D. Giacca, Overburden gradient from sonic log, *SPWLA Transactions*, 1979.

Beltrami, H., and E. Bourlon, Ground warming patterns in the Northern Hemisphere during the last five centuries, *Global and Planetary Change*, *227*, 169–177, 2004.

Beltrami, H., and J.-C. Mareschal, Resolution of ground temperature histories inverted from borehole temperature data, *Global and Planetary Change*, *11*, 57–70, 1995.

Beltrami, H., and A. E. Taylor, Records of climatic change in the canadian arctic: Towards calibrating oxygen isotope data with geothermal data, *Global and Planetary Change*, *11*, 127–138, 1995.

Beltrami, H., D. S. Chapman, S. Archambault, and Y. Bergeron, Reconstruction of high resolution ground temperature histories combining dendrochronological and geothermal data, *Earth and Planetary Science Letters*, *136*, 437–445, 1995.

Beltrami, H., L. Cheng, and J. C. Mareschal, Simultaneous inversion of borehole temperature data for determination of ground surface temperature history, *Geophysical Journal International*, *129*, 311–318, 1997.

Benaouda, D., G. Wadge, R. B. Whitmarsh, R. G. Rothwell, and C. MacLeod, Inferring the lithology of borehole rocks by applying neural network classifiers to downhole logs: An example from the Ocean Drilling Program, *Geophysical Journal International*, *136*, 477-491, 1999.

Berglund, A.-C., Nonlinear regularization — with applications to geophysics, Ph.D. thesis, Department of Informatics and Mathematical Modeling, Technical University of Denmark, 2002.

Bhatt, A., and H. B. Helle, Committee neural networks for porosity and permeability prediction, *Geophysical Prospecting*, *50*, 645–660, 2002.

Bischof, C., B. Lang, and A. Vehreschild, Automatic differentiation for MATLAB programs, *Proceedings in Applied Mathematics and Mechanics*, *2*, 50–53, 2003.

Bischof, C. H., H. M. Bücker, B. Lang, A. Rasch, and A. Vehreschild, Combining source transformation and operator overloading techniques to compute derivatives for MATLAB programs, in *Proceedings of the Second IEEE International Workshop on Source Code Analysis and Manipulation (SCAM 2002)*, pp. 65–72, IEEE Computer Society, Los Alamitos, CA, USA, 2002.

Blackwell, D. D., and J. L. Steele, Thermal conductivity of sedimentary rocks: Measurement and significance, in *Thermal History of Sedimentary Basins, Methods and case Histories*, edited by N. D. Naeser and T. H. McCulloh, chap. 2, pp. 13–35, Springer, New York, 1989.

Blobel, V., and E. Lohrmann, *Statistische und numerische Methoden der Datenanalyse*, B. G. Teubner, Leipzig, 1998.

Bredehoeft, J. D., and I. S. Papadopulos, Rates of vertical groundwater movement estimated from the Earth's thermal profile, *Water Resources Research*, *1*, 325–328, 1965.

Brigaud, F., and G. Vasseur, Mineralogy, porosity and fluid control on thermal conductivity of sedimentary rocks, *Geophysical Journal International*, *98*, 525–542, 1989.

Brigaud, F., D. S. Chapman, and S. Le Douran, Estimating thermal conductivity in sedimentary basins using lithologic data and geophysical well logs, *American Association of Petroleum Geologists Bulletin*, *74*, 1459–1477, 1990.

Bücker, C., and L. Rybach, A simple method to determine heat production from gamma-ray logs, *Marine and Petroleum Geology*, *13*, 373–375, 1996.

Budiansky, B., Thermal and thermoelastic properties of isotropic composites, *Journal of Composite Materials*, *4*, 286–295, 1970.

Bullard, E. C., Heat flow in South Africa, *Proceedings of the Royal Society London, Series A*, *173*, 474–502, 1939.

Buntebarth, G., Thermal properties of KTB-Oberpfalz VB core samples at elevated temperature and pressure, *Scientific Drilling*, *2*, 73–80, 1991.

Buntebarth, G., and J. R. Schopper, Experimental and theoretical investigations on the influence of fluids, solids and interactions between them on thermal properties of porous rocks, *Physics and Chemistry of the Earth*, *23*, 1141–1146, 1998.

Burke, J. A., A. W. Schmidt, and J. Campbell, Raymond L., The litho-porosity cross plot; a method of determining rock characteristics for computation of log data, *The Log Analyst*, *10*, 25–43, 1969.

Carslaw, H. S., and J. C. Jaeger, *Conduction of heat in solids*, 2nd ed., Clarendon Press, Oxford, 1959.

Čermák, V., and L. Rybach, Thermal conductivity and specific heat of minerals and rocks, in *Landolt Börnstein: Physical Properties of Rocks, Group V, Geophysics, Volume 1a*, edited by G. Angenheister, pp. 305–343, Springer, Berlin, 1982.

Chapman, D. S., and K. P. Furlong, Thermal state of the continental lower crust, in *Continental lower Crust*, edited by D. M. Fountain, R. Arculus, and R. W. Kay, vol. 23 of *Developments in Geotectonics*, pp. 179–199, Elsevier, Amsterdam, 1992.

Cheng, C. H., and M. N. Toksöz, Inversion of seismic velocities for the pore aspect ratio distribution of a rock, *Journal of Geophysical Research*, *84*, 7533–7543, 1979.

Clauser, C., *Thermal signatures of heat transfer processes in the Earth's crust*, Springer, Berlin–Heidelberg, 1999.

Clauser, C., Geothermal energy, in *Landolt-Börnstein, Group VIII: Advanced Materials and Technologies, Vol. 3: Energy Technologies, Subvol. C: Renewable Energies*, edited by K. Heinloth, pp. 493–604, Springer Verlag, Heidelberg-Berlin, 2006.

Clauser, C., and E. Huenges, Thermal conductivity of rocks and minerals, in *Rock Physics and Phase Relations – a Handbook of Physical Constants, AGU Reference Shelf*, edited by T. J. Ahrens, vol. 3, pp. 105–126, American Geophysical Union, Washington, 1995.

Clauser, C., and J. C. Mareschal, Ground temperature history in central Europe from borehole temperature data, *Geophysical Journal International*, *121*, 805–817, 1995.

Clauser, C., and H. Villinger, Analysis of conductive and convective heat transfer in a sedimentary basin, demonstrated for the Rheingraben, *Geophysical Journal International*, *100*, 393–414, 1990.

Clauser, C., P. Giese, E. Huenges, T. Kohl, H. Lehmann, L. Rybach, J. Šafanda, H. Wilhelm, K. Windloff, and G. Zoth, The thermal regime of the crystalline continental crust: Implications from the KTB, *Journal of Geophysical Research*, *102*, 18417–18441, 1997.

Clauser, C., F. Höhne, A. Hartmann, V. R. Deetjen, H., W. Rühaak, R. Schellschmidt, and A. Zschocke, Erkennen und Quantifizieren von Strömung: Eine geothermische Rasteranalyse zur Klassifizierung des Untergrundes in Deutschland hinsichtlich seiner Eignung zur Endlagerung radioaktiver Stoffe, *Endbericht*, Applied Geophysics, RWTH Aachen University, 2002.

Clavier, C., and D. H. Rust, MID plot: A new lithology technique, *The Log Analyst*, *17*, 16–24, 1976.

Coleman, T. F., and Y. Li, An interior, trust region approach for nonlinear minimization subject to bounds, *SIAM Journal on Optimization*, *6*, 418–445, 1996.

Constable, S. C., R. L. Parker, and C. G. Constable, Occam's inversion: A practical algorithm for generating smooth models from electromagnetic sounding data, *Geophysics*, *52*, 289–300, 1987.

Crain, E. R., *The Log Analysis Handbook, Volume 1*, PennWell, Tulsa, 1986.

Curtis, A. R., M. J. D. Powell, and J. K. Reid, On the estimation of sparse Jacobian matrices, *Journal of the Institute of Mathematics and its Applications*, *13*, 117–119, 1974.

Demongodin, L., B. Pinoteau, G. Vasseur, and R. Gable, Thermal conductivity and well logs: A case study from the Paris basin, *Geophysical Journal International*, *105*, 675–691, 1991.

Diment, W. H., and H. H. Pratt, Thermal conductivity of some rock-forming minerals: A tabulation, *Open-File Report 88-690*, United States Geological Survey, Denver, 1988.

Doveton, J. H., and H. W. Cable, Fast matrix methods for the lithological interpretation of geophysical logs, *Computers & Geology*, *3*, 101-116, 1979.

Doveton, J. H., A. Förster, and D. F. Merriam, Predicting thermal conductivity from petrophysical logs: A midcontinent paleozoic case study, in *Proceedings of IAMG'97*, edited by V. Pawlowsky-Glahn, pp. 212–217, Centro Internacional de Métodos Numéricos en Ingeniería, Barcelona, 1997.

Ellis, D. V., *Well logging for earth scientists*, Elsevier, Amsterdam, 1987.

Esper, J., E. R. Cook, and F. H. Schweingruber, Low-frequency signals in long tree-ring chronologies for reconstructing past temperature variability, *Science*, *295*, 2250–2253, 2002.

Evans, T. R., Thermal properties of North Sea rocks, *Log Analyst*, *18*, 3–12, 1977.

Farquharson, C. G., and D. W. Oldenburg, A comparison of automatic techniques for estimating the regularization parameter in non-linear inverse problems, *Geophysical Journal International*, *156*, 411–425, 2004.

Fox Maule, C., M. E. Purucker, N. Olsen, and K. Mosegaard, Heat flux anomalies in Antarctica revealed by satellite magnetic data, *Science*, *309*, 464–467, doi:10.1126/science.1106888, 2005.

Geyer, O. F., and M. P. Gwinner, *Geologie von Baden-Württemberg*, 4th ed., E. Schweizerbart'sche Verlagsbuchhandlung, Stuttgart, Germany, 1991.

Gilbert, J. R., C. Moler, and R. Schreiber, Sparse matrices in MATLAB: Design and implementation, *SIAM Journal on Matrix Analysis and Applications*, *13*, 333–356, 1992.

González-Rouco, F., H. von Storch, and E. Zorita, Deep soil temperature as proxy for surface air-temperature in a coupled model simulation of the last thousand years, *Geophysical Research Letters*, *30*, 2116, doi:10.1029/2003GL018264, 2003.

Goss, R., J. Combs, and A. Timur, Prediction of thermal conductivity in rocks from other physical parameters and from standard geophysical well logs, in *Transactions of the SPWLA Annual Logging Symposium*, vol. 16, Paper MM, Society of Professional Well Log Analysts, New Orleans, 1975.

Goutorbe, B., F. Lucazeau, and A. Bonneville, Using neural networks to predict thermal conductivity from geophysical well logs, *Geophysical Journal International*, *166*, 115–125, 2006.

Gretener, P. E., On the thermal instability of large diameter wells — an observational report, *Geophysics*, *32*, 727–738, 1967.

Griewank, A., *Evaluating Derivatives: Principles and Techniques of Algorithmic Differentiation*, no. 19 in Frontiers in Appl. Math., SIAM, Philadelphia, PA, 2000.

Haber, E., and D. Oldenburg, A GCV based method for nonlinear ill-posed problems, *Computational Geosciences*, *4*, 41–63, 2000.

Haenel, R., L. Rybach, and L. Stegena (Eds.), *Handbook of terrestrial Heat-Flow Density Determination*, Solid Earth Science Library, Kluwer Academic Publishers, 1988.

Han, D. H., A. Nur, and D. Morgan, Effects of porosity and clay content on wave velocities in sandstones, *Geophysics*, *51*, 2093–2107, 1986.

Hanke, M., *Conjugate Gradient Type Methods for Ill-posed Problems*, Pitman Research Notes in Mathematics, Longman Scientific and Technical, Harlow, UK, 1995.

Hansen, P. C., *Rank Deficient and Discrete Ill-posed Problems. Numerical Aspects of Linear Inversion*, SIAM, Philadelphia, 1998.

Hartmann, A., V. Rath, and C. Clauser, Identifying paleoclimatic signals in borehole temperature logs as a step towards isolating advective effects, 5th International Meeting on Heat Flow and Structure of the Lithosphere, Kostelec nad Cernými Lesy, Czech Republic, 2001, www.geophysik.rwth-aachen.de/Downloads/pdf/AH_Kostelec2001_slides.pdf.

Hashin, Z., and S. Shtrikman, A variational approach to the theory of the effective magnetic permeability of multiphase materials, *Journal of Applied Physics*, *33*, 3125–3131, 1962.

Hearst, J. R., P. H. Nelson, and F. L. Paillet, *Well logging for physical properties*, Wiley, New York, 2000.

Hill, R., A self-consistent mechanics of composite materials, *Journal of the Mechanics and Physics of Solids*, *13*, 213–222, 1965.

Holt, R. M., C. Lehr, C. J. Kentner, and P. Spits, In-situ porosity from cores: Poroelastic correction for stress relief during coring, *Petrophysics*, *44*, 253–261, 2003.

Hoppie, B. W., High-resolution lithologic characterization of sequences on the New Jersey margin slope through inversion of leg 150 logging data for lithologies, in *Proceedings of the Ocean Drilling Program, Scientific Results*, edited by G. S. Mountain, K. G. Miller, P. Blum, C. W. Poag, and D. C. Twitchell, vol. 150, pp. 385–409, Texas A&M University, College Station, Texas, 1996.

Horai, K.-I., Thermal conductivity of rock-forming minerals, *Journal of Geophysical Research*, *76*, 1278–1308, 1971.

Horai, K.-I., Thermal conductivity of Hawaian basalt: A new interpretation of Robertson and Peck's data, *Journal of Geophysical Research*, *96*, 4125–4132, 1991.

Hotchkiss, W. O., and L. R. Ingersoll, Postglacial time calculations from recent geothermal measurements in the Calumet copper mines, *Journal of Geology*, *42(2)*, 113–122, 1934.

Huang, S., H. N. Pollack, and P.-Y. Shen, Temperature trends over the past five centuries reconstructed from borehole temperatures, *Nature*, *403*, 756–758, 2000.

Huffel, S. V., and J. Vandewalle, *The Total Least Squares Problem: Computational Aspects and Analysis*, vol. 9 of *Frontiers in Applied Mathematics*, SIAM, Philadelphia, 1991.

Jones, M. Q. W., P. D. Tyson, and G. R. J. Cooper, Modelling climatic change in South Africa from perturbed borehole temperature profiles, *Quarternary International*, *57/58*, 185–192, 1999.

Jun, Y., Reservoir parameters estimation from well log and core data: A case study from the North Sea, *Petroleum Geoscience*, *8*, 63–69, 2002.

Kobolev, V. P., R. I. Kutas, and Y. A. Popov, Method and results of research of thermal properties of Ural region rocks with laser scanning, *Geophysical Journal, Kiev*, *12*, 29–37, 1990.

Kohl, T., Palaeoclimatic temperature signals — can they be washed out?, *Tectonophysics*, *291*, 225–234, 1998.

Kohl, T., Transient thermal effects below complex topographies, *Tectonophysics*, *306*, 311-324, 1999.

Korvin, G., The hierarchy of velocity formulae: Gerneralized mean value theorems, *Acta Geodaetica, Geophysica et Montanista, Hungarian Academy of Science*, *13*, 211–222, 1978.

Korvin, G., Axiomatic characterization of the general mixture rule, *Geoexploration*, *19*, 267–276, 1982.

Lanczos, C., *Linear Differential Operators*, Van Nostrand, London, 1961.

Lane, A. C., Geotherms of Lake Superior copper country, *Geological Society of America Bulletin*, *34*, 703–720, 1923.

Lemcke, K., and W. Tunn, Tiefenwasser in der süddeutschen Molasse und ihrer verkarsteten Malmunterlage, *Bulletin der Vereinigung Schweizerischer Petroleum-Geologen und -Ingenieure*, *23*, 35–56, 1956.

Lucazeau, F., F. Brigaud, and J. L. Bouroullec, High-resolution heat flow density in the lower Congo basin, *Geochemistry Geophysics Geosystems*, *5*, 2004.

Magnus, G., Beschreibung eines Maximumthermometers und einiger damit angestellten Versuche in einem Bohrloche zu Rüdersdorf, *Annalen der Physik und Chemie*, *22*, 136–150, 1831.

Mann, M. E., and P. D. Jones, Global surface temperatures over the past two millennia, *Geophysical Research Letters*, *30*, 1820, doi:10.1029/2003GL017814, 2003.

Mann, M. E., and G. A. Schmidt, Ground vs. surface air temperature trends: Implications for borehole surface temperature reconstructions, *Geophysical Research Letters*, *30*, 1607, doi:10.1029/2003GL017170, 2003.

Mareschal, J.-C., and H. Beltrami, Evidence for recent warming from perturbed geothermal gradients: Examples from Eastern Canada, *Climate Dynamics*, *6*, 135–143, 1992.

Mavko, G., T. Mukerji, and J. Dvorkin, *The Rock Physics Handbook*, Cambridge University Press, Cambridge, U.K., 1998.

Mayr, S., Der Einfluß der Mikrostruktur auf die Ultraschalleigenschaften von Sandsteinen bei hydrostatischen Druckbedingungen, Dissertation, Technische Universität Berlin, 2002.

Menke, W., *Geophysical Data Analysis: Discrete Inverse Theory*, International Geophysics Series, no. 45, Academic Press, 1989.

Mügler, C., M. Filippi, P. Montarnal, J.-M. Martinez, and Y. Wileveau, Determination of the thermal conductivity of opalinus clay via simulations of experiments performed at the Mont Terri underground laboratory, *Journal of Applied Geophysics*, *58*, 112–129, 2006.

Nielsen, S. B., and N. Balling, Transient heat flow in a stratified medium, *Tectonophysics*, *121*, 1–10, 1985.

Nieto, J. A., D. P. Yale, and R. J. Evans, Improved methods for correcting core porosity to reservoir conditions, *The Log Analyst*, *35*, 21–30, 1994.

Nitoiu, D., and H. Beltrami, Subsurface thermal effects of land-use changes, *Journal of Geophysical Research*, *110*, F01005, doi:10.1029/2004JF000151, 2005.

Popov, Y. A., Optical scanning technology for nondestructive contactless measurements of thermal conductivity and diffusivity of solid matter, in *Experimental Heat Transfer, Fluid Mechanics and Thermodynamics, Proc of the 4th World Congress on Experimental Heat Transfer, Fluid Mechanics and Thermodynamics*, edited by M. Giot, F. Mayinger , and G. P. Celata, vol. 1, pp. 109–116, Brussels, Belgium, 1997.

Popov, Y. A., A. V. Sukhorada, R. A. Romushkevich, and V. G. Semenov, Thermal conductivity of Ukrainian shield rocks, *Geology and Prospecting*, *3*, 71–78, 1990.

Popov, Y. A., D. F. C. Pribnow, J. H. Sass, C. F. Williams, and H. Burkhardt, Characterization of rock thermal conductivity by high-resolution optical scanning, *Geothermics*, *28*, 253-276, 1999.

Popov, Y. A., J. Pohl, R. Romushkevich, V. Tertychnyi, and H. Soffel, Geothermal characteristics of the Ries impact structure, *Geophysical Journal International*, *154*, 355–378, 2003a.

Popov, Y. A., V. Tertychnyi, R. Romushkevich, D. Korobkov, and J. Pohl, Interrelations between thermal conductivity and other physical properties of rocks: Experimental data, *Pure and Applied Geophysics*, *160*, 1137-1161, 2003b.

Portniaguine, O., and M. S. Zhdanov, Focusing geophysical inversion images, *Geophysics*, *64*, 874–887, 1999.

Rall, L. B., and G. F. Corliss, An introduction to automatic differentiation, in *Computational Differentiation: Techniques, Applications, and Tools*, edited by M. Berz, C. H. Bischof, G. F. Corliss, and A. Griewank, pp. 1–17, SIAM, Philadelphia, PA, 1996.

Rath, V., and C. Clauser, Erkennen und Quantifizieren von Strömung: Eine geothermische Rasteranalyse zur Klassifizierung des tiefen Untergrundes in Deutschland hinsichtlich seiner Eignung zur Endlagerung radioaktiver Stoffe — Fortsetzung, *Endbericht*, Geophysica Beratungsgesellschaft mbH, Angewandte Geophysik RWTH Aachen, Hochleistungsrechnen RWTH Aachen und GGA-Institut Hannover, 2005.

Rath, V., and D. Mottaghy, Smooth inversion for ground surface temperature histories: Estimating the optimum regularization parameter by generalized cross-validation, *Geophysical Journal International*, *171*, 1440–1448, doi:10.1111/j.1365-246X.2007.03587.x, 2007.

Raymer, L. L., E. R. Hunt, and J. S. Gardner, An improved sonic transit time-to-porosity transform, in *Transactions of the SPWLA Annual Logging Symposium*, vol. 21, Paper P, Society of Professional Well Log Analysts, 1980.

Reiter, M., Possible ambiguities in subsurface temperature logs: Consideration of ground-water flow and ground surface temperature change, *Pure and Applied Geophysics*, *162*, 343–355, 2005.

Reiter, M., A. J. Mansure, and B. K. Peterson, Precision continuous temperature logging and comparison with other types of logs, *Geophysics*, *45*, 1857-1868, 1980.

Rellstab, W., Der Einfluß des Paläoklimas auf das Temperaturfeld in der Schweiz, *Tech. rep.*, Institut für Geophysik, ETH, Zürich, 1981.

Rényi, A., Some fundamental questions of information theory, in *Selected Papers of Alfred Rényi*, vol. 2, pp. 526–552, Akademia Kiado, Budapest, 1976.

Robertson, E. C., Thermal properties of rocks, *Open-File Report 88-441*, United States Geological Survey, Reston, 1988.

Robertson, E. C., and D. L. Peck, Thermal conductivity of vesicular basalt from Hawaii, *Journal of Geophysical Research*, *79*, 4875–4888, 1974.

Roy, R. F., A. E. Beck, and Y. S. Touloukian, Thermophysical properties of rocks, in *Physical Properties of Rocks and Minerals*, edited by Y. S. Touloukian, W. R. Judd, and R. F. Roy, pp. 409–502, McGraw-Hill, New York, 1981.

Rybach, L., Determination of heat production rate, in *Handbook of Terrestrial Heat-Flow Density Determination*, edited by R. Haenel, L. Rybach, and L. Stegena, pp. 125–142, Kluwer, 1988.

Sass, J. H., A. H. Lachenbruch, and R. J. Munroe, Thermal conductivity of rocks from measurements on fragments and its application to heat-flow determination, *Journal of Geophysical Research*, *76*, 3391–3401, 1971.

Sass, J. H., A. H. Lachenbruch, T. H. J. Moses, and P. Morgan, Heat flow from a scientific research well at Cajon Pass, California, *Journal of Geophysical Research*, *97*, 5017-5030, 1992.

Schulz, B., Thermal conductivity of porous and highly porous materials, *High Temperatures High Pressures*, *13*, 649–660, 1981.

Seipold, U., The variation of thermal transport properties in the Earth's crust, *Journal of Geodynamics*, *20*, 145–154, 1995.

Şerban, D. Z., and B. H. Jacobsen, The use of broad-band prior covariance for inverse paleoclimate estimation, *Geophysical Journal International*, *147*, 29–40, 2001.

Serra, O., *Fundamentals of Well-Log Interpretation*, Elsevier, New York, 1984.

Shao, J., and D. Tu, *The Jacknife and the Bootstrap*, Springer, New York, 1995.

Shapiro, N. M., and M. H. Ritzwoller, Inferring surface heat flux distributions guided by a global seismic model: particular application to Antarctica, *Earth and Planetary Science Letters*, *223*, 213–224, 2004.

Shen, P. Y., and A. E. Beck, Least squares inversion of borehole temperature measurements in functional space, *Journal of Geophysical Research*, *96*, 19965–19979, 1991.

Shen, P. Y., and A. E. Beck, Paleoclimate change and heat flow density inferred from temperature data in the Superior Province of the Canadian Shield, in *Climatic Change Inferred from Underground Temperatures, Paleogeography, Paleoclimatology, Paleoecology (Global and Planetary Change Section)*, edited by T. J. Lewis, vol. 98, pp. 143–165, Elsevier, Amsterdam, 1992.

Shen, P. Y., H. N. Pollack, S. Huang, and K. Wang, Effects of subsurface heterogeneity on the inference of climate change from borehole temperature data: Model studies and field examples from Canada, *Journal of Geophysical Research*, *100*, 6383–6396, 1995.

Signorelli, S., and T. Kohl, Regional ground surface temperature mapping from meteorological data, *Global and Planetary Change*, *40*, 267–284, 2004.

Stallmann, R. W., Computation of ground-water velocity from temperature data, in *Methods of collecting and interpreting ground-water data*, edited by R. Bentall, Geological Survey Water-Supply Paper 1544-H, pp. 36-46, United States Geological Survey, Washington, 1963.

Surma, F., and Y. Geraud, Porosity and thermal conductivity of the Soultz-sous-Forets granite, *Pure and Applied Geophysics*, *160*, 1125–1136, 2003.

Taniguchi, M., J. Shimada, T. Tanaka, I. Kayane, Y. Sakura, Y. Shimano, S. Dapaah-Siakwan, and S. Kawashima, Disturbances of temperature-depth profiles due to surface climate change and subsurface water flow: 1. An effect of linear increase in surface temperature caused by global warming and urbanization in the Tokyo metropolitan area, Japan, *Water Resources Research*, *35*, 1507–1517, 1999.

Tarantola, A., *Inverse Problem Theory and Methods for Model Parameter Estimation*, SIAM, Philadelphia, 2005.

Tarantola, A., and B. Valette, Generalized nonlinear inverse problems solved using the least squares criterion, *Reviews of Geophysics and Space Physics*, *20*, 219–232, 1982.

Vacquier, V., Y. Mathieu, E. Legendre, and E. Blondin, Experiment on estimating thermal conductivity from oil well logging, *American Association of Petroleum Geologists Bulletin*, *72*, 758–764, 1988.

van der Kamp, G., and S. Bachu, Use of dimensional analysis in the study of thermal effects of various hydrogeological regimes, in *Hydrogeological regimes and their subsurface thermal effects*, edited by A. E. Beck, G. Garven, and L. Stegena, vol. 47 of *Geophysical Monograph*, pp. 23–28, American Geophysical Union, Washington, 1989.

Vasseur, G., L. Demongodin, and A. Bonneville, Thermal modelling of fluid flow effects in thin-dipping aquifers, *Geophysical Journal International*, *112*, 276–289, 1993.

Vosteen, H.-D., and R. Schellschmidt, Influence of temperature on thermal conductivity, thermal capacity and thermal diffusivity for different types of rock, *Physics and Chemistry of the Earth*, *28*, 499-509, 2003.

Wagner, W., and A. Pruß, The IAPWS formulation 1995 for the thermodyamic properties of ordinary water substance for general and scientific use, *Journal of Physical and Chemical Reference Data*, *31*, 387–535, 2002.

Waples, D. W., and H. Tirsgaard, Changes in matrix thermal conductivity of clays and claystones as a function of compaction, *Petroleum Geoscience*, *8*, 365–370, 2002.

Weber, M. E., F. Niessen, G. Kuhn, and M. Wiedicke, Calibration and application of marine sedimentary physical properties using a multi-sensor core-logger, *Marine Geology*, *136*, 151–172, 1997.

Williams, C. F., and R. Anderson, Thermophysical properties of the earth's crust: In situ measurements from continental and ocean drilling, *Journal of Geophysical Research*, *95*, 9209–9236, 1990.

Winkler, H. G. F., *Petrogenesis of Metamorphic Rocks*, Springer, New York, 1979.

Wyllie, M. R. J., A. R. Gregory, and G. H. F. Gardner, Elastic wave velocities in heterogenous and porous media, *Geophysics*, *21*, 41–70, 1956.

Zhdanov, M. S., and E. Tolsataya, Minimum support nonlinear parametrization in the solution of a 3D magnetotelluric inverse problem, *Inverse Problems*, *20*, 937–952, doi:10.1088/02665611/20/3/017, 2004.

Ziagos, J. P., and D. D. Blackwell, A model for the effect of horizontal fluid flow in a thin aquifer on temperature-depth profiles, *Geothermal Research Council, Transactions*, *5*, 221–223, 1981.

Zimmerman, R. W., The effect of pore structure on the pore and bulk compressibilities of consolidated sandstones, Ph.D. thesis, University of California, Berkeley, Ca., 1984.

Zimmerman, R. W., Thermal conductivity of fluid saturated rocks, *Journal of Petroleum Science and Engineering*, *3*, 219–227, 1989.

Zimmerman, R. W., W. H. Somerton, and M. S. King, Compressibility of porous rocks, *Geophysics*, *91*, 12765–12777, 1986.

Zschocke, A., V. Rath, and C. Clauser, Estimating darcy flow velocities from correlated anomalies in temperature logs, *Journal of Geophysics and Engineering*, *2*, 332–342, 2005.

Appendix

A Mathematical derivations

A.1 Generalised t-th order mean

The generalised t-th order mean λ_t

$$\lambda_t(\phi, \lambda_p, \lambda_m, t) = \left[\phi\lambda_p^t + (1-\phi)\lambda_m^t\right]^{1/t} \tag{A.1}$$

reduces to the harmonic mean, geometric mean, and arithmetic mean for values of $t = -1, 0, 1$, respectively. For $t = -1$ and 1 this can be seen easily by inserting the values into equation A.1. To obtain the geometric mixing law, however, the limit for $t \to 0$ has to be computed,

$$\lambda_{t=0} = \lim_{t\to 0} \lambda_t = \lim_{t\to 0} [\phi\lambda_p^t + (1-\phi)\lambda_m^t]^{1/t}. \tag{A.2}$$

This equation is transformed by taking the natural logarithm of both sides and using the fact that $\ln(\lim_{x\to 0} f(x)) = \lim_{x\to 0} \ln(f(x))$

$$\ln \lambda_{t=0} = \lim_{t\to 0} \ln \lambda_t = \lim_{t\to 0} \frac{\ln[\phi\lambda_p^t + (1-\phi)\lambda_m^t]}{t}. \tag{A.3}$$

Using the rule of de l'Hospital yields:

$$\begin{aligned} \ln \lambda_{t=0} &= \lim_{t\to 0} \frac{\phi\lambda_p^t \ln \lambda_p + (1-\phi)\lambda_m^t \ln \lambda_m}{\phi\lambda_p^t + (1-\phi)\lambda_m^t}, & \text{(A.4)} \\ &= \phi \ln \lambda_p + (1-\phi) \ln \lambda_m. & \text{(A.5)} \end{aligned}$$

Exponentiating both sides of this expression gives the familiar geometric mixing law.

A.2 Gamma-ray tool

Inserting the impulse response of the tool (equation 4.5) into the integral equation 4.7 gives

$$GR(z_d) = \sum_l \frac{GR_l}{2\alpha} \int_{z_{l-1}}^{z_l} \mathrm{e}^{-|z'-z_d|/\alpha} dz'. \tag{A.6}$$

The integral in this equation has to be solved separately for the three cases where $(z_d \leq z_{l-1})$, $(z_d \geq z_l)$, and $(z_{l-1} < z_d < z_l)$. For case 1 we obtain

$$z_d \leq z_{l-1}: \quad \frac{GR_l}{2\alpha} \int_{z_{l-1}}^{z_l} \exp\left(-\frac{z' - z_d}{\alpha}\right) dz' \tag{A.7}$$

$$= \frac{GR_l}{2\alpha} \left[-\alpha \exp\left(-\frac{z' - z_d}{\alpha}\right)\right]_{z_{l-1}}^{z_l} \tag{A.8}$$

$$= -\frac{GR_l}{2} \left[\exp\left(-\frac{z_l - z_d}{\alpha}\right) - \exp\left(-\frac{z_{l-1} - z_d}{\alpha}\right)\right] \tag{A.9}$$

$$= \frac{GR_l}{2} \left|\exp\left(-\frac{|z_l - z_d|}{\alpha}\right) - \exp\left(-\frac{|z_{l-1} - z_d|}{\alpha}\right)\right|. \tag{A.10}$$

Case 2:

$$z_d \geq z_l: \quad \frac{GR_l}{2\alpha} \int_{z_{l-1}}^{z_l} \exp\left(\frac{z' - z_d}{\alpha}\right) dz' \tag{A.11}$$

$$= \frac{GR_l}{2\alpha} \left[\alpha \exp\left(\frac{z' - z_d}{\alpha}\right)\right]_{z_{l-1}}^{z_l} \tag{A.12}$$

$$= \frac{GR_l}{2} \left[\exp\left(\frac{z_l - z_d}{\alpha}\right) - \exp\left(\frac{z_{l-1} - z_d}{\alpha}\right)\right] \tag{A.13}$$

$$= \frac{GR_l}{2} \left|\exp\left(-\frac{|z_l - z_d|}{\alpha}\right) - \exp\left(-\frac{|z_{l-1} - z_d|}{\alpha}\right)\right|. \tag{A.14}$$

This is the same result as for case 1. Case 3 gives rise to the following equations:

$$\frac{GR_l}{2\alpha} \int_{z_{l-1}}^{z_l} \exp\left(\frac{z' - z_d}{\alpha}\right) dz' \tag{A.15}$$

$$= \frac{GR_l}{2\alpha} \int_{z_{l-1}}^{z_d} \exp\left(-\frac{z' - z_d}{\alpha}\right) + \frac{GR_l}{2\alpha} \int_{z_d}^{z_l} \exp\left(\frac{z' - z_d}{\alpha}\right). \tag{A.16}$$

With the solutions of case 1 and 2 this equations becomes

$$\frac{GR_l}{2} \left|1 - \exp\left(-\frac{|z_{l-1} - z_d|}{\alpha}\right)\right| + \frac{GR_l}{2} \left|\exp\left(-\frac{|z_l - z_d|}{\alpha}\right) - 1\right| \tag{A.17}$$

$$= GR_l \left[1 - \frac{1}{2}\exp\left(-\frac{|z_{l-1} - z_d|}{\alpha}\right) - \frac{1}{2}\exp\left(-\frac{|z_l - z_d|}{\alpha}\right)\right]. \tag{A.18}$$

When the layer k is defined by $z_{k-1} < z_d < z_k$ the combined solution is given by

$$GR(z_d) = \sum_{l, l \neq k} \frac{GR_l}{2} \left|\exp\left(-\frac{|z_l - z_d|}{\alpha}\right) - \exp\left(-\frac{|z_{l-1} - z_d|}{\alpha}\right)\right|$$

$$+ GR_k \left[1 - \frac{1}{2}\exp\left(-\frac{|z_{k-1} - z_d|}{\alpha}\right) - \frac{1}{2}\exp\left(-\frac{|z_k - z_d|}{\alpha}\right)\right]. \tag{A.19}$$

The correction factor $c(z_d)$ corrects for the finite depth extent of the sum of integrals given in equation 4.7. It can be found by integrating the impulse response over the full infinite depth range and the actually used finite range and taking the ratio of both:

$$c(z_d) = \frac{\int_{-\infty}^{+\infty} I(z', z_d)dz'}{\int_{z_t}^{z_b} I(z', z_d)dz'}. \tag{A.20}$$

Here, z_t and z_b denote the top and bottom of the finite depth interval. Because the unit impulse response is normalised, integrating the numerator of equation A.20 yields a value of 1. Integrating the denominator of equation A.20 leads to

$$\begin{aligned}
\int_{z_b}^{z_t} I(z', z_d)dz' &= \frac{1}{2\alpha} \int_{z_t}^{z_b} \exp\left(-\frac{|z' - z_d|}{\alpha}\right) dz' && \text{(A.21)} \\
&= \frac{1}{2\alpha} \left[\int_{z_t}^{z_d} \exp\left(-\frac{z_d - z'}{\alpha}\right) dz' + \int_{z_d}^{z_b} \exp\left(-\frac{z' - z_d}{\alpha}\right) dz' \right] && \text{(A.22)} \\
&= \frac{1}{2} \exp\left(-\frac{z_d - z'}{\alpha}\right)\Big|_{z_t}^{z_d} - \frac{1}{2} \exp\left(-\frac{z' - z_d}{\alpha}\right)\Big|_{z_d}^{z_b} && \text{(A.23)} \\
&= \frac{1}{2}\left[1 - \exp\left(-\frac{z_d - z_t}{\alpha}\right)\right] + \frac{1}{2}\left[1 - \exp\left(-\frac{z_b - z_d}{\alpha}\right)\right] && \text{(A.24)} \\
&= \frac{1}{2}\left(2 - \exp\left(-\frac{z_d - z_t}{\alpha}\right) - \exp\left(-\frac{z_b - z_d}{\alpha}\right)\right). && \text{(A.25)}
\end{aligned}$$

Thus, the correction factor $c(z_d)$ is given by

$$c(z_d) = 2\left[2 - \exp\left(-\frac{z_d - z_t}{\alpha}\right) - \exp\left(-\frac{z_b - z_d}{\alpha}\right)\right]^{-1}. \tag{A.26}$$

B Petrophysical measurements

Table B.1: Thermal conductivity [$W(m\,K)^{-1}$] as a function of temperature measured using the divided bar method. All samples are from the Molasse Basin. For a detailed sample description see *Clauser et al.* [2002].

Sample	T [°C]	5	15	25	35	50	70	90	110	130	150
Bt1.3		2.40	2.39	2.35	2.32	2.28	2.23	2.18	2.08	2.01	1.95
Bt2.1		2.58	2.53	2.50	2.45	2.41	2.35	2.28	2.21	2.11	2.01
Bt3.3		1.86	1.86	1.85	1.83	1.82	1.79	1.76	1.70	1.64	1.59
Bw603		2.05	2.02	2.00	1.97	1.94	1.89	1.85	1.78	1.72	1.69
DST1b		2.38	2.35	2.31	2.28	2.22	2.16	2.10	2.04	1.99	1.96
DST2b		2.52	2.49	2.42	2.37	2.31	2.23	2.16	2.10	2.04	2.00
DST3b		2.30	2.28	2.24	2.20	2.15	2.08	2.02	1.95	1.91	1.88
DST4b		2.65	2.62	2.55	2.51	2.43	2.35	2.28	2.21	2.14	2.10
E1a		3.02	2.99	2.94	2.90	2.84	2.79	2.71	2.65	2.59	2.54
E2a		2.88	2.85	2.83	2.80	2.74	2.69	2.60	2.54	2.46	2.40
E3a		2.21	2.16	2.11	2.05	1.98	1.89	1.80	1.73	1.65	1.59
E4a		2.94	2.86	2.79	2.72	2.62	2.49	2.40	2.32	2.25	2.19
E5a		2.16	2.14	2.10	2.07	2.04	1.98	1.95	1.90	1.87	1.83
E6a		2.37	2.34	2.29	2.26	2.21	2.16	2.11	2.08	2.03	1.99
S2b		2.52	2.50	2.46	2.40	2.34	2.27	2.19	2.14	2.07	2.01
S3c		1.77	1.77	1.76	1.74	1.72	1.72	1.70	1.68	1.64	1.62
Sa1b		2.53	2.50	2.45	2.40	2.35	2.27	2.21	2.15	2.09	2.04
Sa2b		2.00	1.98	1.95	1.92	1.88	1.84	1.79	1.74	1.70	1.66
Sa3a		2.45	2.43	2.36	2.32	2.26	2.19	2.11	2.07	2.00	1.95
Sa5b		2.96	2.92	2.85	2.79	2.72	2.61	2.55	2.48	2.43	2.39
Sa6b		3.28	3.22	3.14	3.06	2.93	2.82	2.70	2.60	2.51	2.44
Sa7b		3.17	3.10	3.01	2.95	2.82	2.71	2.59	2.49	2.41	2.33

Table B.2: Values for sonic velocity v_p for varying confining pressure P. z values give converted depths for pressure gradients of 20, 23, and 25 MPa km^{-1}.

P [MPa]	v_p [m s^{-1}]	z_{23} [m]	z_{20} [m]	z_{25} [m]
0.00	1592	0	0	0
0.76	1777	34	38	30
1.14	1855	50	57	45
1.51	1925	67	76	61
1.89	2001	84	95	76
2.27	2134	101	114	91
2.65	2132	117	132	106
3.03	2208	134	151	121
3.41	2254	151	170	136
4.16	2345	185	208	167
4.92	2395	218	246	197
5.68	2466	252	284	227
6.43	2507	285	322	257
7.57	2572	335	378	303
9.46	2657	419	473	378

C Well locations

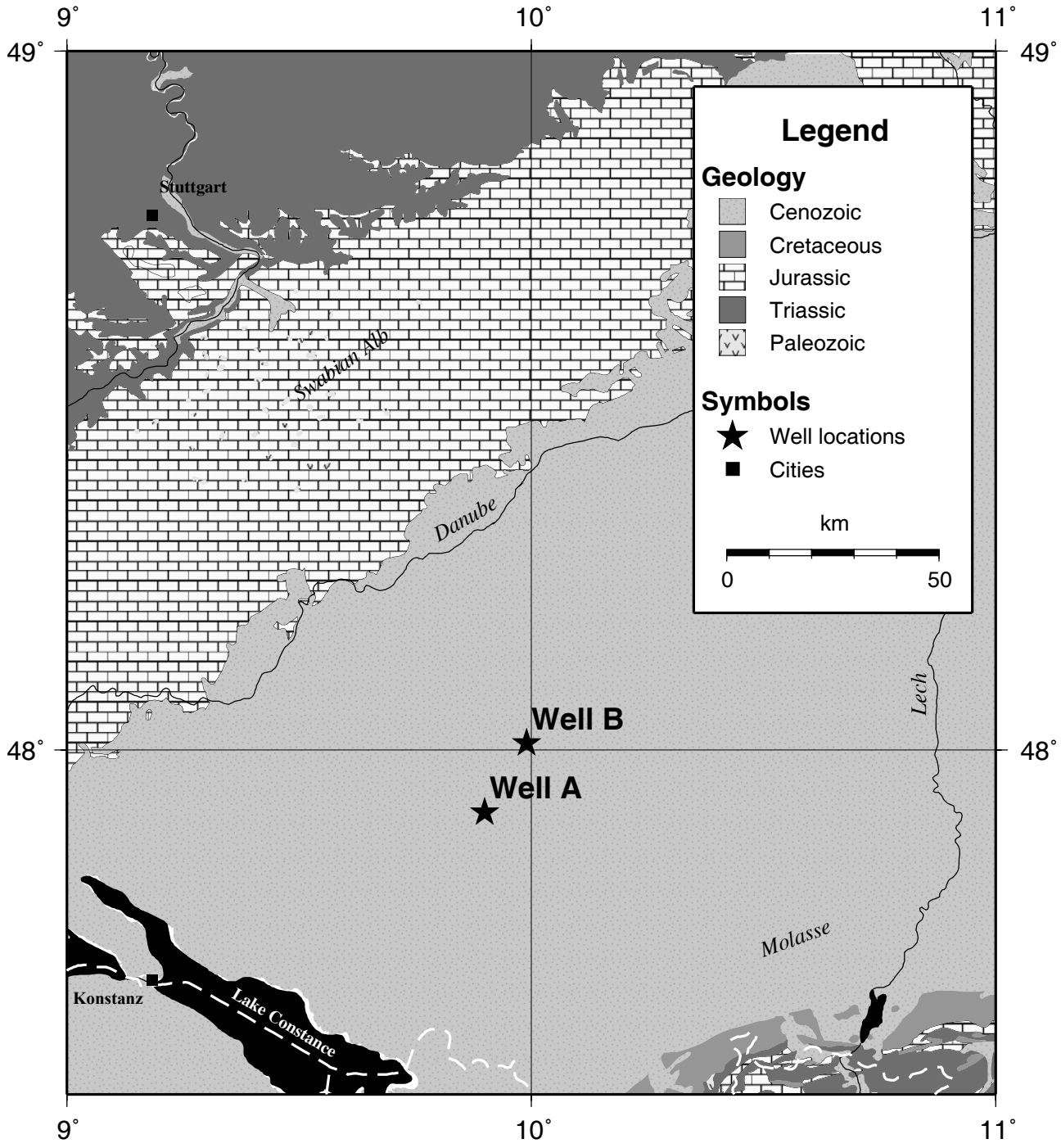

Figure C.1: Overview map of well locations in the Southern German Molasse. Well A is studied in chapter 3. Well B is discussed in section 4.4.1.

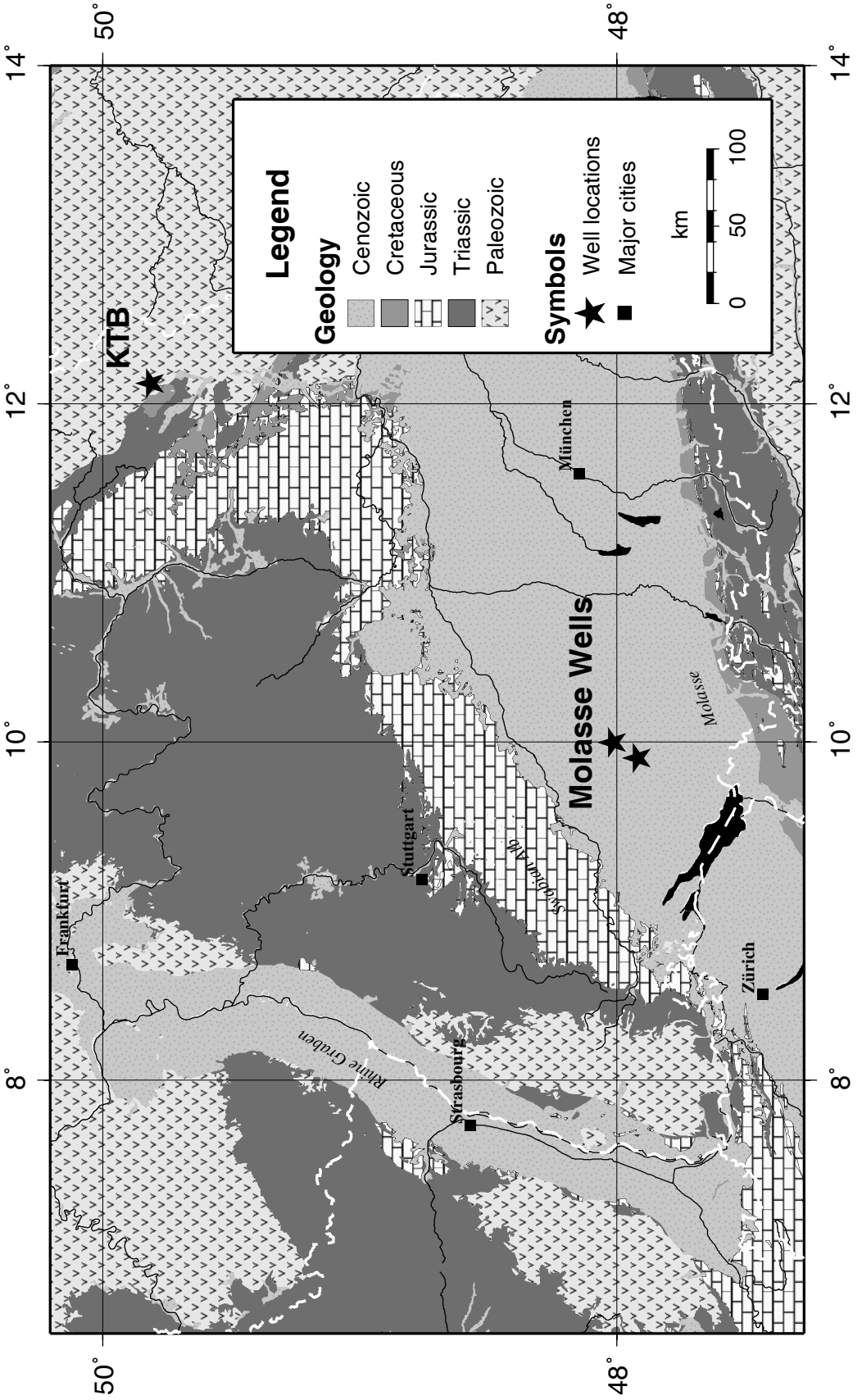

Figure C.2: Geologic overview map of Southern Germany showing the locations of the wells (stars) studied in this thesis. KTB is studied in chapter 2, wells in the Western Molasse are shown in more detail in figure C.1.

Acknowledgements

A lot of people helped me to prepare this thesis. Without them the work would have been more difficult and certainly much less fun.

First of all I would like to thank Prof. Clauser for the opportunity to prepare this thesis under his supervision. I am also indebted to Dr. Lucazeau for refereeing the manuscript.

Many thanks go to all the people at the RWTH Aachen Geophysics group. In particular Volker Rath always provided helpful advice and good ideas. I would like to thank Norbert Klitzsch for discussions and the work outs and Ute Kreutz for her administrative support. I also want to mention the people who generated the laboratory data that I am using throughout this work. Lothar Ahrensmeier, Dirk Breuer, and Frank Höhne at the RWTH Aachen and Hilke Deetjen at the GGA Hannover performed most of the measurements and were of great help. Especially Dirk Breuer conscientiously kept the laboratory equipment up and running and always looked for ways to improve the quality of the measurements. Sonic velocity under confining pressure was measured by Sibylle Mayr at the TU Berlin.

Cores, well-logging data, and archive data were kindly provided by the Geological Survey of Baden-Württemberg (LGRB), the Geological Survey of Lower Saxony (NLfB), and by the Wintershall AG. Part of this work was funded under grants 9X0009-8390-0, 9WS-0009-8497-2, and FKZ0329985 from the Federal Environment Ministry of Germany.

Finally, I am grateful to my wife and my kids for their support and the joy they brought me.

Abstract

This thesis analyses the inversion of petrophysical and temperature measurements for the study of geothermal problems. The inversion of temperature data and the inversion of petrophysical measurements are first considered separately, then jointly by introducing a new algorithm for the combined inversion.

Heat conduction is studied with emphasis on the transient effect of a variable ground surface temperature caused by past climate changes. Here, the focus is on uncertainties and sensitivity of the results when using insufficient data. Inversions are subdivided into two types based on the length of the computed time-series: (1) Analyses of the last ice-age (10^5 years length) and (2) studies of the last 1000 years. For the first type of inversion the length of the temperature log is the primary restriction, with a depth of 3000 m necessary to obtain a correct result. The second type is most affected by demands on low noise data. A very good knowledge of thermal conductivity is required for both types of inversion. This implies that an inversion of ground surface temperature histories can greatly benefit from a continuous profile of thermal properties. Thermal diffusivity has a secondary effect on the inversion results but thermal conductivity directly influences the inference of ground surface temperatures. This is particularly true for boreholes in sedimentary basins where petrophysical properties can vary continuously with depth.

The combined inversion requires to study the feasibility of calculating thermal conductivity from other petrophysical properties. Core data from the Southern German Molasse Basin are used for this purpose. A regression analysis of thermal conductivity, sonic velocity, bulk density, and porosity yields an accuracy of ± 0.2 W(m K)$^{-1}$ for the prediction of thermal conductivity. This type of direct correlation is suitable for predicting thermal conductivity from a single petrophysical property. For the study of wireline data, a mixing law approach is used. Existing mixing laws are reviewed to choose the most appropriate one. Relationships based on a two phase mixture and one using an additional rock structure parameter are analysed. For the water-saturated rocks studied here, the geometric mixing law is appropriate. For dry samples, the structure of the rock cannot be neglected.

The computation of thermal conductivity from wireline data is performed for a borehole from the Southern German Molasse Basin. Two inverse algorithms of varying complexity are used and the results are tested against core data from the same borehole. The accuracy of the prediction is ± 0.3 W(m K)$^{-1}$. The uncertainty is larger than for the computation of thermal conductivity from core measurements under controlled laboratory conditions. This is due to problems of core-log matching, different spatial resolution of measurements, and changes in sample properties during the coring process. However, the large number of data points compensates this disadvantage.

The analysis shows the feasibility of the inversion of wireline measurements for the computation of thermophysical data. An extension of the method to include borehole temperature data seems sensible.

To this end an algorithm is proposed to achieve the joint inversion. Requirements are different from conventional algorithms for the petrophysical problem because the differential equation for transient heat conduction needs to be solved, resulting in a more complex forward problem. The inverse problem is solved by a Quasi-Newton iterative scheme with a Bayesian type regularisation. To make the implementation most efficient the techniques of automatic differentiation and matrix compression are considered. In this particular application automatic differentiation does not improve efficiency. Matrix compression can drastically improve the computational speed of the algorithm for certain classes of inverse problems. Those involving transient heat conduction cannot be compressed efficiently whereas purely petrophysical problems have a much higher compression ratio.

A comparison of results of the new algorithm with the programs used before for the paleoclimate and petrophysical inversion shows that these problems can be treated as special cases of the new algorithm. A borehole in Southern Germany serves as a case study for the algorithm. An inversion is performed using wireline and temperature data. The algorithm is able to match both wireline and temperature data with good accuracy and in a consistent manner. The ground surface temperature history cannot be reconstructed without ambiguity because of two reasons: (1) The log terminates at 2000 m depth, too shallow for a full reconstruction of the temperatures of the last glacial; (2) In the inversion results, the transient temperature perturbation is not entirely independent of the petrophysical properties. In particular this is the case for the shale petrophysical properties that are not well constrained.

The petrophysical inversion is demonstrated in a second case study on a core sample that is extensively analysed using continuous core scanning methods. The sample consists of low-porosity chemical sediments. Several petrophysical models are tested to provide the optimum match to the measured data. Wyllie's travel time average and the geometric mixing law fail to explain the measured values of sonic velocity and thermal conductivity. Therefore, a mixing law using an additional structural parameter is introduced in the inversion and the mineral thermal conductivities are considered as inversion parameters. This allows a detailed analysis yielding a value of the structural parameter and values for mineral thermal conductivities suitable for this type of sediment.

Zusammenfassung

Die vorliegende Arbeit behandelt die Inversion von petrophysikalischen Messungen und Temperaturmessungen in der Anwendung auf geothermische Fragestellungen. Die Inversion von Temperaturdaten und die Inversion petrophysikalischer Messungen werden zunächst getrennt betrachtet. Danach wird ein neuer Algorithmus für eine kombinierte Inversion eingeführt, der eine gemeinsame Analyse ermöglicht.

Die Wärmeleitung wird unter Berücksichtigung transienter Effekte durch eine variable Erdbodentemperatur analysiert, die wiederum durch vergangene Klimaänderungen hervorgerufen wurden. Der Schwerpunkt liegt hier auf Unsicherheiten und Sensitivitäten der Ergebnisse bei nicht ausreichenden Daten. Zwei Typen von Inversionen werden, basierend auf der Länge der berechneten Zeitreihe, unterschieden: (1) Analysen der letzten Eiszeit (10^5 Jahre Länge) und (2) Untersuchungen der letzten 1000 Jahre. Für den ersten Inversionstyp ist die Tiefe des Temperaturlogs die wichtigste Randbedingung. Eine Tiefe von 3000 m ist notwendig, um ein korrektes Ergebnis zu erzielen. Der zweite Typ ist am stärksten von Datenrauschen beeinflusst. Eine sehr gute Kenntnis der Wärmeleitfähigkeit des Untergrundes ist für beide Analysetypen notwendig. Dies bedeutet, dass ein kontinuierliches Tiefenprofil der Wärmeleitfähigkeit die Inversion der zeitlichen Entwicklung der Erdbodentemperatur sehr verbessern kann. Die Temperaturleitfähigkeit hat einen sekundären Einfluss auf die Inversionsergebnisse, während die Wärmeleitfähigkeit einen direkten Einfluss auf die Ableitung der Erdbodentemperatur hat. Dies ist insbesondere in Sedimentbecken wichtig, in denen petrophysikalische Eigenschaften kontinuierlich mit der Tiefe variieren können.

Eine Voraussetzung für die kombinierte Inversion ist die Analyse der Machbarkeit der Berechnung der Wärmeleitfähigkeit aus anderen petrophysikalischen Eigenschaften. Diese Analyse wird anhand von Kerndaten aus dem süddeutschen Molassebecken durchgeführt. Eine Regressionsanalyse von Wärmeleitfähigkeit, akustischer Wellengeschwindigkeit, Rohdichte und Porosität ergibt eine Genauigkeit von ± 0.2 W(m K)$^{-1}$ für die Vorhersage der Wärmeleitfähigkeit. Diese Methode der direkten Korrelation ist geeignet für die Berechnung der Wärmeleitfähigkeit auf der Basis einer einzigen petrophysikalischen Eigenschaft. Ein Mischungsgesetz-Ansatz wird für die Analyse von bohrlochgeophysikalischen Messungen benutzt. Bekannte Mischungsgesetze werden bewertet, um einen geeigneten Zusammenhang zu finden. Neben Beziehungen, die auf einem Zweiphasengemisch beruhen, wird ein Gesetz mit einem zusätzlichen Parameter für die Gesteinsstruktur analysiert. Für die hier untersuchten wassergesättigten Proben ist das geometrische Mischungsgesetz adäquat. Für trockene Proben kann die Struktur des Gesteins nicht vernachlässigt werden.

Anhand einer Bohrung aus dem süddeutschen Molassebecken wird die Berechnung der Wärmeleitfähigkeit aus bohrlochgeophysikalischen Messungen durchgeführt. Zwei inverse Algorithmen mit unterschiedlicher Komplexität werden benutzt und ihre Ergebnisse mit Kernmessungen verglichen. Die Genauigkeit der Berechnung liegt bei ± 0.3 W(m K)$^{-1}$. Die Unsicherheit ist größer als jene der Berechnung der Wärmeleitfähigkeit aus Kernmessungen unter kontrollierten Laborbedingungen. Dies ist auf Probleme bei der Zuordnung von Kern- zu Bohrlochdaten, unterschiedliche räumliche Auflösungen der Messungen und Änderungen der Gesteinseigenschaften während des Kernens zurückzuführen. Dieser Nachteil wird jedoch durch die große Anzahl an Messpunkten ausgeglichen. Die Analyse zeigt, dass die Inversion von Bohrlochmessungen zur Berechnung von thermophysikalischen Eigenschaften durchführbar ist und Temperaturmessungen im Bohrloch einbeziehen sollte.

Zu diesem Zweck wird ein Algorithmus für eine gemeinsame Inversion entwickelt. Da die partielle Differentialgleichung für die transiente Wärmeleitung gelöst werden muss, unterscheiden sich die Anforderungen von denen für eine petrophysikalische Inversion und führen zu einem komplexeren Vorwärtsproblem. Das inverse Problem wird mit einer iterativen Quasi-Newton Methode mit bayesscher Regularisierung gelöst. Um die Implementierung möglichst effizient zu gestalten, werden die Verfahren der automatischen Differentiation und der Matrixkomprimierung untersucht. Für die vorliegende Anwendung kann keine Verbesserung der Effizienz durch automatische Differentiation erzielt werden. Matrixkomprimierung verkürzt die Rechendauer für bestimmte Klassen von inversen Problemen drastisch. Transiente Wärmeleitungsprobleme können nicht effektiv komprimiert werden, wohingegen rein petrophysikalische Probleme eine wesentlich höhere Kompressionsrate erzielen.

Der neue Algorithmus wird mit denen verglichen, die vorher für die getrennten Inversionen zur Paläoklimabestimmung und zur Wärmeleitfähigkeitsberechnung benutzt wurden. Diese können als Spezialfall des neuen Algorithmus betrachtet werden. Bohrlochgeophysikalische Daten und Temperaturmessungen in einem Bohrloch in der süddeutschen Molasse liefern die Daten für eine Fallstudie. Der Algorithmus kann sowohl die bohrlochgeophysikalischen als auch die Temperaturdaten konsistent und mit guter Genauigkeit anpassen. Die Rekonstruktion der Zeitreihe der Erdbodentemperatur bleibt aus zwei Gründen mehrdeutig: (1) Die Temperaturmessung reicht bis in eine Tiefe von 2000 m, zu flach um die Erdbodentemperatur des letzten Glazials komplett aufzulösen; (2) In den Inversionsergebnissen ist die transiente Temperaturstörung nicht vollkommen unabhängig von den petrophysikalischen Eigenschaften. Insbesondere die Eigenschaften des „Shale“-Anteils sind nur schlecht bestimmt.

Eine zweite Fallstudie demonstriert die petrophysikalische Inversion mithilfe einer Gesteinsprobe, an der umfangreiche Untersuchungen mit kontinuierlichen Kernabtastmethoden durchgeführt wurden. Die Kernprobe besteht aus chemischen Sedimenten geringer Porosität. Verschiedene petrophysikalische Modelle werden getestet, um eine optimale Anpassung an die Messdaten zu erhalten. Es stellt sich heraus, dass Wyllie's Laufzeitmittelwert und das geometrische Mischungsgesetz nicht die Messwerte der akustischen Geschwindigkeit und der Wärmeleitfähigkeit erklären können. Daher werden ein Mischungsmodell mit einem zusätzlichen Strukturparameter und die Mineralwärmeleitfähigkeiten als Inversionsparameter benutzt. Die detaillierte Analyse liefert geeignet Werte für die Eigenschaften dieses Sedimenttyps.

Curriculum Vitae

Persönliche Daten

Name:	Andreas Hartmann
Geburtsdatum:	10. Februar 1970
Geburtsort:	Sassenberg
Familienstand:	verheiratet

Lebenslauf

1976 – 1980	Besuch der Grundschule Sassenberg
1980 – 1986	Besuch des Gymnasium Laurentianum Warendorf
1986 – 1989	Berufsausbildung zum Fernmeldehandwerker bei der Deutschen Bundespost, Oberpostdirektion Münster
1989 – 1990	Fachoberschule Warendorf
1990 – 1992	Studium der Physik an der Universität Gesamthochschule Paderborn, Vordiplom Physik
1993	Studium der Physik an der Western Michigan University, Kalamazoo, USA
1993 – 1997	Studium der Geophysik an der Universität Bremen
1997	Diplom Geophysik, Thema: Ein neues Inversionsverfahren zur Auswertung mariner Wärmestromdichtemessungen
1998 – 2000	Field processing geophysicist, Western Geophysical, London
2000 – 2006	Wissenschaftlicher Angestellter, Institut für Angewandte Geophysik, RWTH Aachen
seit 2006	Geophysiker, Baker Hughes INTEQ, Celle